6-29-2018

Radiation Effects in Apatite and High Entropy Alloy under Energetic Ions and Electrons

Jianren Zhou
Louisiana State University and Agricultural and Mechanical College

RADIATION EFFECTS IN APATITE AND HIGH ENTROPY ALLOY UNDER ENERGETIC IONS AND ELECTRONS

A Dissertation

Submitted to the Graduate Faculty of the
Louisiana State University and
Agricultural and Mechanical College
in partial fulfillment of the
requirements for the degree of
Doctor of Philosophy

in

The Department of Mechanical & Industrial Engineering

by
Jianren Zhou
B.S., Chongqing University of Technology, 2011
M.S., South China University of Technology, 2014
August 2018

ACKNOWLEDGEMENTS

First and foremost, I would like to express my sincere appreciation to my major advisor Prof. Fengyuan Lu of Louisiana State University for his expert advice and continuous assistance throughout the projects, for his excellent guidance throughout my Ph.D. study, and for his generous support in this research study. It is a great opportunity for me to join his group and work with him. Through my Ph.D. study, I am benefited much from his knowledge, encouragement, and patience. I also would like to sincerely thank Prof. Wenjin Meng, Prof. Ying Wang, Prof. Jianwei Wang, and Prof. Rui Zhang for serving on my doctoral committee.

I would like to thank the Louisiana Board of Regents LINK award and Ziegler Energy Scholarship for the financial support. Without these funding, this dissertation would not have been possible.

I wish to address special thanks to Dr. Mark Kirk, Pete Baldo, and Ed Ryan of the Intermediate Voltage Electron Microscopy (IVEM)-Tandem Facility at the Nuclear Engineering Division of Argonne National Lab for assistance with the ion irradiation experiments. Special thanks to Dr. Dongmei Cao at the Shared Instrument Facility of Louisiana State University for the help of material's characterization (TEM, SEM, and FIB) and electron irradiation experiments. Special thanks to Dr. Ying Xiao for the preparation of microtome-cutting TEM samples.

I wish to address special thanks to Dr. Tiankai Yao, Prof. Jie Lian at the Department of Mechanical, Aerospace, and Nuclear Engineering at Rensselaer Polytechnic Institute for providing the spark plasma sintering hydroxyapatite samples. Special thanks to Dr. Yiqiang Shen and Dr. Zhili Dong at the School of Materials Science and Engineering at Nanyang Technological University in Singapore for providing the Ce-doped silicate apatite samples. Special thanks to Dr. Shengmin Guo at the Department of Mechanical & Industrial Engineering at Louisiana State University for providing the high entropy alloys samples.

I wish to address many thanks to the Nuclear Energy Materials Group (NEMG) members: Mr. Md I Islam and Mr. Todd Sherman, and all the peers and friends at Louisiana State University for their help and support during my Ph.D. study.

Last but not least, I am greatly indebted to my parents and family. My parents, Mr. Yinhe Zhou and Ms. Shuhua Wan, who always encourage me and give me the motivation to study. My brother, Mr. Jianyi Zhou, who loves and supports me at all time. My wife, Dr. Caroline Yu, who gives me the strength and ambition, and who always wants to create a bright future together with me.

TABLE OF CONTENTS

LIST OF FIGURES

LIST OF ABBREVIATION

BCC	Body centered cubic
BF	Bright field
DF	Dark field
DPA	Displacement per atom
EDS	Energy dispersive spectrometry
FCC	Face centered cubic
FIB	Focus ion beam
FFT	Fast fourier transformation
HAP	Hydroxyapatite
HCP	Hexagonal close-packed
HEA	High entropy alloy
HEBM	High energy ball milling
HLW	High level waste
HRTEM	High-resolution transmission electron microscopy
ILW	Intermediate level waste
IVEM	Intermediate voltage electron microscopy
IFFT	Inverse fast fourier transformation
LLW	Low level waste
PKA	Primary knock-on atom
PIPS	Precision Ion Polishing System
PPM	Parts per million
RT	Room temperature

SAED	Select area electron diffraction
SEM	Scanning electron microscopy
SRIM	Stopping and Ranges of Ions in Matter
SPS	Spark plasma sintering
TEM	Transmission electron microscopy
VLM	Vacuum levitation melting
XRD	X-ray diffraction

ABSTRACT

Radiation effects in apatite and high entropy alloy under energetic ions and electrons are studied in this doctoral dissertation to develop advanced crystalline ceramic waste forms and nuclear structural materials. Apatite is proposed as a ceramic waste form for the immobilization of radionuclides, but its performance is strongly affected by the irradiation of the incorporated radionuclides. It is thus important to understand the radiation effects in apatite structure and the underlying physics. Effects of chemical composition, grain size, interfacial structure, as well as radiation conditions on the microstructural evolution, phase transformation and damage mechanisms of apatite under alpha-decay and beta-decay events, simulated by 1 MeV Kr ions and 200 keV electrons respectively, are investigated. Composition effect on silicate apatite shows the better radiation tolerance under higher cerium content. Size effect on hydroxyapatite exhibits the reduction of radiation stability with the decrease of grain size due to excess surface energy in nanoparticles. A further study addresses densified nanocrystalline hydroxyapatite exhibits higher radiation tolerance than the same sized hydroxyapatite nanoparticle as a result of lower interface energy. Effect of radiation conditions on the recrystallization behaviors of pre-amorphized hydroxyapatite is also studied. *In-situ* TEM observation reveals a rapid recrystallization process and a notable size effect, which smaller sized sample nucleates and fully recrystallizes under lower electron fluence. Recrystallization mechanism is attributed to ionization process as a result of breaking and reforming of dangling bonds. The radiation effect study is further extended to include high entropy alloys intended as structural materials in advanced nuclear reactors. Two types of high entropy alloys are selected as model alloys to investigate the irradiation-induced behaviors under 1 MeV Kr ions. Study on nanocrystalline $Al_xCoCrFeNi$ alloys shows a notable ion-irradiation-induced grain growth, whose mechanisms are attributed to a disorder-driven

mechanism for the initial fast increase of grain size and defect-stimulated mechanism for the later slow grain size increase, elucidated by the thermal spike model. Study on HfNbTaTiVZr alloy reveals a crystal-to-amorphous phase transformation with critical amorphization dose of 2 displacements per atom (dpa) at 298 K, while the amorphization is suppressed when the temperature increases to 423 K.

CHAPTER 1 INTRODUCTION

1.1 Nuclear waste

Energy consumption and energy supply have become one of the most important issues facing our current society. Advanced nuclear energy offers greater energy security and reliable supply with extremely low carbon emission as compared to other energy sources. However, with the continued expansion of the nuclear industry, the disposal of nuclear wastes has become a major concern. Nuclear wastes are generated in the nuclear fuel cycle, decommissioning nuclear power plants or nuclear weapon production, with radioactivity exceeding the threshold defined by legislation[1]. Based on its activity and heat generating capacity, nuclear waste can be classified into Low Level Waste (LLW), Intermediate Level Waste (ILW, term used in Europe), High Level Waste (HLW), and transuranic waste (TRU) [2]. The intensely radioactive HLW and TRU are mainly from spent nuclear fuel and weapons development and contains α, β, γ activities[3, 4]. To dispose them, sophisticated disposal techniques and storage including substantial shielding and durable host matrix are required[5]. In particular, the long-lived radionuclides can be incorporated into and immobilized in the lattice structure of a solid matrix that is chemically and mechanically durable, thermodynamically stable, and radiation resistant, for long-term geological disposal. It is also a great challenge to find a suitable geological repository to dispose the HLW. A typical geological repository for the immobilized nuclear waste is shown in Figure 1.1, where nuclear waste will be transported down vertically and stored in chambers hundreds of meters underground. Usually, there are several barriers for an HLW repository system: the conditioned waste form, the container, a geo-engineered barrier or backfill, seals, as well as the host rock and the overlaying geological layers.

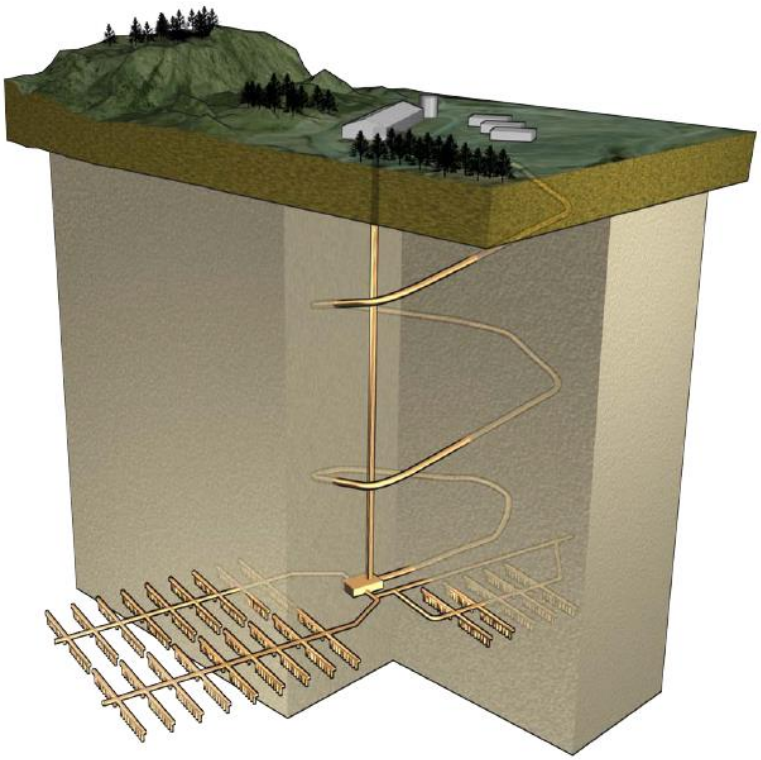

Figure 1.1 A typical geological storage of high-level nuclear waste[6]

1.2 Nuclear waste forms

Nuclear waste forms are host materials, usually amorphous or crystalline, containing different types of radioactive waste. The long-term disposal of radioactive waste has become a major nuclear waste management strategy as a consequence of the continuous increase of the nuclear power worldwide. Overall, nuclear waste forms for long-term disposal should be thermally, chemically, and physically stable, have low radionuclide release and low sensitivity to waste stream variations, and possess good impact resistance in transport, and good waste density loadings[7].

1.2.1 Glass waste forms

Glass has been used as host materials for the immobilization of HLW. Glass was initially proposed as a waste form in the early 1950s in Canada to contain radionuclides and provide

protection against radiation damage[8-10]. Glass waste forms can incorporate a large number of elements, and offer high chemical and physical durability[11], and high radiation tolerance, with reasonable costs made available by the contemporary glass manufacturing technology. Borosilicate and phosphate glasses are among the most commonly used host materials for the immobilization of HLW at present. The immobilization mechanism to incorporate HLW into glass waste forms is the vitrification process, which consists of the evaporation of excess water, calcination, glass melting, and finally pouring and cooling of the waste glass product. However, glass waste form has a limited loading for HLW such as actinides, lanthanides, and halides[3], and more importantly, the inclusion of these radionuclides results in chemical instability which in the long term will increase the leaching and devitrification and degrade the ability of glass as a waste form[12].

1.2.2 Ceramic waste forms

Many crystalline mineral-structures were proposed as an alternative waste form because they have a high chemical stability and can retain high concentrations of radionuclides but still remain thermodynamically stable for millions of years[13]. Furthermore, crystalline waste forms are inherently highly leach resistant for a much longer time, have excellent thermal and mechanical stability and a much higher loading ability for HLWs, as compared to glass. This is especially important for the long-term disposal of HLW and TRU. However, there is a possibility that the crystalline waste forms will undergo a crystalline to amorphous phase transformation under radiations, as reported in monazite[14], pyrochlore[15-17], zirconolite[18, 19], zircon[20, 21]. The transformation may be accompanied by changes in the volume and radionuclide release rate, which will degrade the performance of the ceramic waste forms. Therefore, one main goal of this study is to understand the behavior of ceramic waste forms under extreme radiation conditions for long-

term radioactive waste management.

Apatite structure-type has also been proposed as a potential crystalline ceramic waste form for HLW and TRU, particularly for actinide and fission product bearing waste streams due to its chemical durability, structure flexibility, promising thermal stability, and low leaching rate. The apatite structure (shown in Figure 1.2) has the chemical formula of $A^{I}_4A^{II}_6(BO_4)_6X_2$, in which A^{I}, A^{II} = Ca, rare earth, fission products and/or actinides; B= Si, P, V or Cr and X= OH, F, Cl, I or O. Apatite exhibits an open frame structure, in which six equivalent BO_4 tetrahedra are corner-connected to AO_6 metaprism columns to form a channel parallel to the c-axis to accommodate X-site anions. This structure shows a potential to incorporate radionuclides like actinides and fission products into its lattice structure to form a new solid solution. In particular, the apatite structures are very promising waste forms to incorporate actinides in the A-site, and the highly volatile and extremely long-lived fission product I-129 in the X site. The size of the channel structure in apatite can be tuned by adjusting the chemical composition, which makes it possible to incorporate the large iodine anions in lead vanadate apatite $Pb_{10}(VO_4)_6I_2$[22, 23]. Similar to other crystalline ceramics, radiation can cause atomic-scale changes that affect their physical properties. When actinides and fission products are incorporated in the apatite structures, they produce ionizing and displacive radiations which may cause damage to the apatite waste form, degrade its chemical stability, and reduce the actinide immobilization performance. On the other hand, the radiation tolerance of the apatite structures may be affected by their chemical compositions, microstructures, and the radiation conditions. Therefore, it is crucial to understand the radiation effects in apatite structures and the underlying physics for the design of advanced nuclear waste forms.

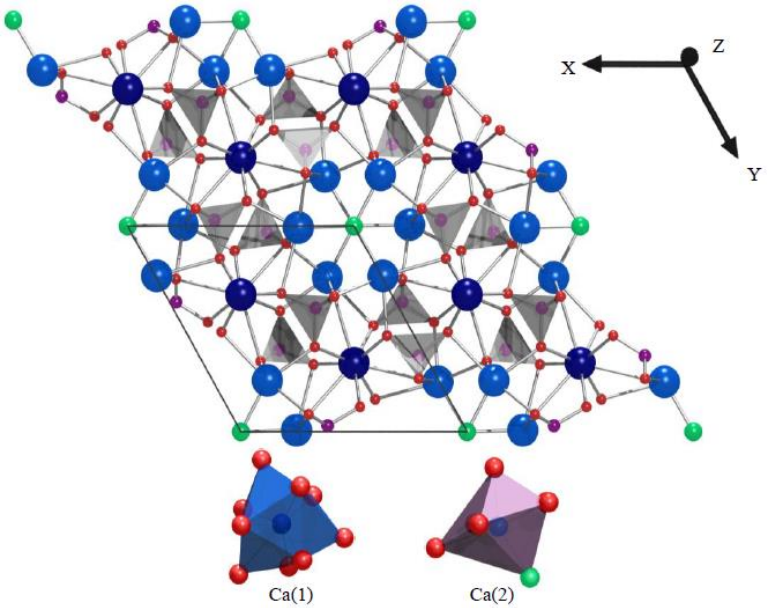

Figure 1.2 Apatite structure, with the two calcium sites as dark and light blue, Ca(I) and Ca(II) respectively. Phosphorus ions are purple, oxygen is red and the PO_4 tetrahedron is grey[6]

In this dissertation, silicate apatite and hydroxyapatite (HAp) were chosen as model materials to study the effects of chemical composition, radiation condition, grain size and interface on the radiation tolerance of the apatite waste form. Silicate apatite doped with a different concentration of cerium was selected to study the chemical composition effect on radiation tolerance, in which cerium is used as a surrogate for the actinide Pu. HAp is the main constituent of animal bone with a stoichiometric composition of $Ca_{10}(PO_4)_6(OH)_2$ and has a poorly crystalline non-stoichiometric nano-sized structure[24]. It is widely believed that nanomaterials have improved exchange and uptake capacities when compared to their micron-sized analogues due to their increased surface area, a significant fraction of defective sites, and higher ability to mitigate radiation-induced damage due to the high density of interfaces that behave as defect sinks[25]. In addition, pure HAp is thermally stable without phase transformations up to 1573 K[26], and its composition, grain size, and interfaces can be easily manipulated. Therefore, HAp is a good model material to study the roles of the aforementioned factors in the radiation response of apatite structure.

1.3 Nuclear structural materials

In the fuel assemblies of nuclear reactors, structural materials are used to encapsulate and hold the fuel rods and other components of the reactor core. In-service core structure materials have to maintain their performance to support the reactor core and prevent the leaking of radioactive materials. Structural materials hold key roles not only in the containment of nuclear fuel and fission products but also in the reliable and thermodynamically efficient production of electrical energy from nuclear reactors. The working conditions for the structural materials are usually very harsh. For example, for a pressurized water reactor, structure materials need to withstand high temperature up to 400°C, high radiation dose up to 20 dpa as well as high pressure up to 155 bar[27]. However, with the development of the new generation of nuclear reactors, harsher conditions are required for structure materials, such as higher irradiation dose as high as 100 dpa and higher temperatures up to 1000°C. The displacement damage and operating temperature regimes for structural materials in current nuclear energy system were shown in Figure 1.3. Therefore, advanced structural materials are required and essential to provide increased strength, thermal creep and radiation damage resistance, and superior corrosion for improved reactor performances[27].

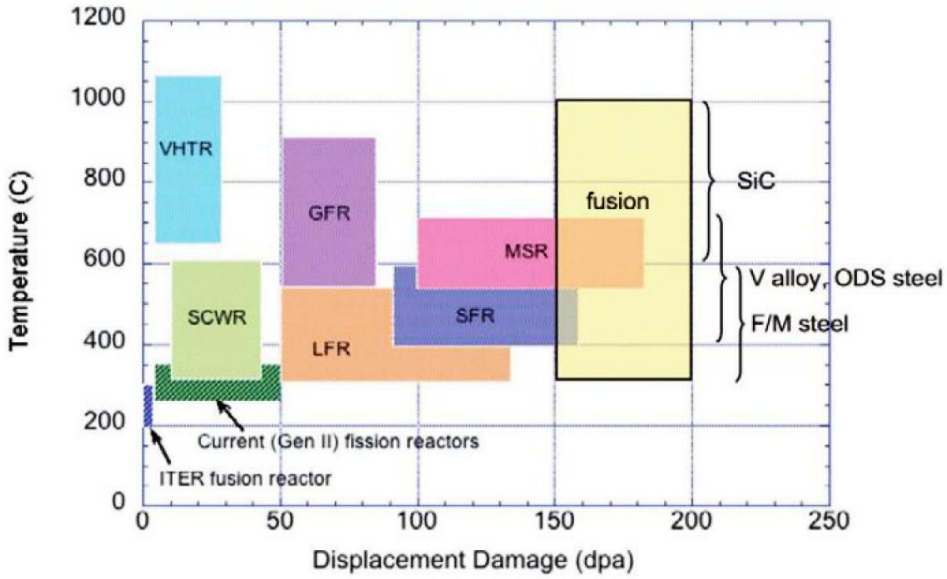

Figure 1.3 The displacement damage and operating temperature regimes for structural materials in current nuclear energy system[27]

1.3.1 Conventional structural alloys

Many conventional structural materials have been widely studied and used for the safe and reliable nuclear energy supply. Ni-based alloys[28], Fe-based systems[29-31], zirconium alloys[32, 33], austenitic steels[34-36], and ferritic/martensitic steels[37] are the commonly used structural alloys in fission reactors. Zirconium alloys are used as fuel cladding for most commercial reactors because they show a good thermal conductivity and are compatible with nuclear fuel and water. Ferritic steels and Ni-based alloys are used as heat exchanger materials for the reliable conversion of thermal energy. Ferritic/martensitic steel[38, 39], oxide dispersion strengthened steel[40, 41], and refractory alloys[42, 43] are commonly used structural materials in fusion reactors.

However, materials degradations under extreme radiation environments have not been fully overcome in spite of the rapid development of these structural alloys for nuclear applications, such as the severe swelling of austenitic steels[34, 35], mechanical property degradation as well as reduced thermal conductivity[44, 45]. A key strategy to design highly radiation resistant materials

is based on the high-temperature strength, phase stability as well as dimensional stability under irradiation conditions because the accumulation of radiation-induced point defects leads to material failure. With the assistance of modern materials science tools, some high-performance materials have been developed. For instance, in a nanocluster-strengthened ferritic steel[46], the formation of highly stable nanoscale clusters enriched in Y, Ti, and O from initial Y_2O_3 and Fe-Ti master alloy powder can be synthesized by ball milling and powder metallurgy techniques. And this nanocluster-strengthened ferritic steel exhibited good fracture toughness at low temperature and high strength as well as respectable radiation resistance. Nevertheless, these traditional alloys may not meet all the requirements of the harsher working condition for the next generation of nuclear reactors, and the development of new alloys as nuclear structure materials becomes indispensable.

1.3.2 High entropy alloys

One new type of alloys, high entropy alloys (HEAs), have attracted great attention recently. HEA contains several principal components, usually no less than 5 elements, with equal or close molar concentrations to form a simple solid solution structure like face-centered cubic (FCC) or body-centered cubic (BCC)[47, 48]. Many studies reported these alloys exhibit excellent chemical and mechanical properties such as high elevated-temperature strength[49, 50], low-temperature toughness[51], excellent wear[52, 53], corrosion[54, 55], as well as oxidation resistance[56], which make them promising candidates for structural materials in nuclear reactors. Their unique properties are closely associated with the local structures within these alloys, particularly local lattice distortions [57-59]. The schematic of the interactions of the severely distorted lattice structure of HEAs with dislocations, electrons, phonons, and x-ray beam was shown in Figure 1.4[60].

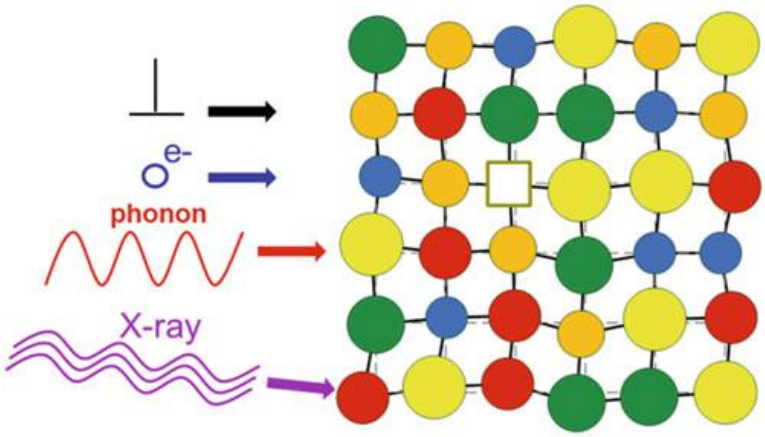

Figure 1.4 Schematic of the interactions of the severely distorted lattice of HEAs with dislocations, electrons, phonons, and x-ray beam[60]

Motivated by HEA's applications in nuclear energy, some researchers have recently started investigating the radiation behavior of HEA, which led to a very limited number of reports showing good radiation resistance and the ability of HEA as a potential structural material candidate under extreme radiation conditions [61-64], suitable for next-generation nuclear system applications. Study on Zr-Hf-Nb[62], a model equiatomic ternary alloy, showed irradiation resistance up to a dose of 10 dpa. Study on CoCrCuFeNi HEA[63] also exhibited this alloy can tolerant irradiation resistance up to 40 dpa. In addition, voids were not observed for FeNiMnCr HEA[65] although the irradiation dose reached up to 10 dpa, and a lower volume swelling of $Al_xCoCrFeNi$ HEAs[66] was also revealed compared to conventional structural materials under similar irradiation conditions. These encouraging results make HEAs very attractive in the applications as nuclear structural materials. However, the issues of radiation-induced hardening and embrittlement, radiation creep, phase instability as a result of precipitation, volumetric swelling in HEA are still there. And structural alloys in real nuclear reactor environment requires further investigations. Therefore, the other major focus of this doctoral dissertation is the phase stability and microstructural evolution of HEA under intense radiations.

1.4 Radiation effects in nuclear materials

In the nuclear fuel cycles, nuclear materials can be affected by a number of different types of irradiations (e.g. alpha, beta, gamma, and neutron). In the current dissertation, the types of radiations relevant to the apatite-based nuclear waste forms and HEA-based structural materials are beta-decay of the fission products and alpha-decay of the actinide elements, which cause significant physical and chemical changes in the waste forms [67-69], as well as neutron irradiation encountered by the structural materials in the reactor core. Ion irradiations provide a cost effective way to simulate the long-term radiation damage induced by alpha-decay events and neutrons in the waste repository and reactor environments. The high dose rate and hence defect production rate of ion accelerators, such as the intermediate voltage electron microscopy (IVEM)-tandem facility at Argonne National Lab, make it possible to reach high radiation damage levels within hours comparable to those in structural materials irradiated in reactors for several years, and those in nuclear waste forms to be irradiated by the incorporated radionuclides for up to millions of years. Similarly, the beta-irradiation effect can be simulated by using the electron beam in a transmission electron microscopy (TEM) [67, 70-72]. When energetic particles such as ions interact with solids, they dissipate their energy through elastic (ballistic) and inelastic collisions. If the ions carry sufficient kinetic energy, such that the energy transferred to the lattice atoms in the elastic collisions exceeds the threshold displacement energy (E_d), the atoms can be directly displaced from their lattice sites by the impinging ions. The displaced atoms, known as the primary knock-on atom (PKA), could continue to interact with other lattice atoms, causing more displacements, leading to displacement cascades and extended damage zones in the irradiated material. To measure the damage level caused by displacive irradiations, the unit displacements per atom (dpa), which is the average number of times each atom is displaced from its original lattice site, is used

to directly compare the damage levels caused by different particles with various energies. Typically, fusion reactors are expected to endure 50-200 dpa during an operational lifetime while pressurized water reactor pressure vessel can experience 1 dpa [27]. On the other hand, the ions also interact with solids through the inelastic ionization processes that excite the electron clouds, followed by electron-phonon coupling that causes a temperature increase. Like ions, energetic electrons can also cause atomic displacement and ionization in the irradiated materials. However, the displacive damage caused by electrons are usually limited due to isolated point defects, rather than extended damage zones in the case of ion irradiations. Both atomic displacement and ionization strongly affect the phase stability and microstructures of the materials, which will be elucidated in the apatite and HEA material systems in the following chapters.

1.5 Motivations

The stability of apatite structure under radiation conditions is key to its application as a ceramic nuclear waste form for the immobilization of long-lived radionuclides. The radiation tolerance of ceramic waste forms strongly depends on their chemical compositions[15, 73], grain sizes[14], surfaces[74-77], interfaces[78-83] and grain boundaries (GBs)[84-89], etc. It has been reported that the chemical composition significantly affects the radiation tolerance of many ceramic waste froms, including phosphate fluorapatite[90], mono-silicate fluorapatite[91], synthetic britholite[92], silicate apatite[93, 94], monazite[14], and pyrochlore[95]. For instance, study of nano-sized tantalate pyrochlore[95] with different compositions showed a higher K^+ content at A site, which increased the average r_A/r_B value and resulted in more structure deviation, reduced the radiation tolerance. The stability of materials under radiations is also found to depend on the grain size, and it has been widely believed that nanostructured materials exhibit higher radiation tolerance compared to their micron-grain-sized counterparts, due to the high density of surfaces

and grain boundaries that behave as sinks for the elimination of radiation-induced defects. This assumption has been supported by many studies. Examples include that nanocrystalline $MgGa_2O_4$ can withstand displacive radiations with a dose up to 96 dpa, while its bulk counterpart can be amorphized by a dose of only 12 dpa[96]; and nanocrystalline TiN had a higher radiation tolerance against amorphization and damage accumulation than its counterpart with coarse grains[97].

However, nanomaterials are not intrinsically radiation resistant, as some recent studies[77, 98] showed extremely reduced grain size could be less radiation tolerant. For example, nanostructured monazite[14] was found to exhibit reduced tolerance under displacive ion irradiations when the grain size was reduced from 40 nm to 20 nm. Such a special size effect was greatly related to the crucial role of interfaces (e.g. grain boundary and surface) under radiation, which has not been fully understood yet. Therefore, the development of apatite-based nuclear waste forms cannot be achieved without understanding the various factors on the radiation stability of the apatite structure. One main objective of the current dissertation is to acquire the fundamental understanding of the radiation response of apatite structure for the design of radiation tolerant apatite-based ceramic waste form for the disposal of HLW in the advanced nuclear energy systems. The main focus is the roles of chemical composition, grain size, interface, and radiation condition on the radiation tolerance of apatite structure.

In Chapter 3, Ce-doped $Mg_2Y_8(SiO_4)_6O_2$ silicate apatite with different Ce content (Ce=0.5 and 0.05) is used to study the composition effect, and the grain size effect is investigated by HAp with different crystallite sizes. Section 3.1 shows radiation tolerance was enhanced by increasing the Ce content at A^I site, meaning radiation tolerance can be controlled by changing the chemical composition. Section 3.2 shows a notable grain size effect on the radiation tolerance, in which a negative effect of grain size reduction on the radiation tolerance of HAp is found. The excess

surface energy of smaller sized HAp may lower the energy gap between the amorphous state and crystalline phase, which can degrade the radiation tolerance. Section 3.3 addresses an important question of how different interfaces, more specifically surface and grain boundary, affect the radiation resistance of the ceramic waste form. Radiation tolerance of HAp nanoparticles and densified nanocrystalline HAp of the same grain size is compared, in which densified nanocrystalline HAp shows a better radiation tolerance because of lower interface energy. Chapter 4 focuses on the different radiation conditions, in particular, displacive and ionizing radiations, on the behavior of the apatite structure. Electron-beam-induced recrystallization of amorphous HAp under different fluxes is reported, and the curve of recrystallization as a function of electron fluence shows a characteristic sigmoidal shape. The recrystallization mechanism is attributed to ionization process as a result of breaking and reforming of dangling bonds along the amorphous-crystalline interface.

To be used as structural materials in advanced nuclear energy systems, HEA must withstand extreme radiation conditions of high doses and temperatures. Chapter 5 focuses on the irradiation performances of two new HEAs: $Al_xCoCrFeNi$ and HfNbTaTiVZr alloys. A notable grain growth is observed for the nanocrystalline $Al_xCoCrFeNi$ alloys. The grain growth process is attributed to the disorder-driven mechanism for the initial fast development and defect-stimulated mechanism for the decelerated later stage. HfNbTaTiVZr on the other hand shows a crystal-to-amorphous phase transformation under displacive radiations, which is greatly suppressed at elevated temperatures due to significant dynamic annealing of the defects. The last chapter of the dissertation (Chapter 6) summarizes the main conclusions and future research of iodine incorporated apatite structure and future researches on HfNbTaTiVZr high entropy alloy.

CHAPTER 2 EXPERIMENTAL TECHNIQUES AND MATERIALS PREPARATION

A systemic study was conducted to understand the radiation effects in apatite and HEA structures, especially the radiation-induced phase transformation and microstructural evolution under intensive ion and electron irradiation bombardments. Comprehensive observation of radiation damage was carried out using IVEM-Tandem facility at Argonne National Lab and *in situ* TEM at Louisiana State University. The details of experimental techniques and materials preparation were discussed in this chapter.

2.1 Materials synthesis

Apatite was chosen as a model material system due to its considerable compositional and structural flexibility to study the radiation damage under extreme conditions. Silicate apatite doped with different concentrations of cerium was used to study the compositional effect upon actinide loading on radiation tolerance of apatite. The Ce doped $Mg_2Y_8(SiO_4)_6O_2$ silicate apatite powders were synthesized by solid state reaction. HAp was used to study the effects of grain size and interface on the radiation tolerance of apatite. The preparation process of HAp powders and pellets was discussed in section 2.1.1. Two HEAs, $Al_xCoCrFeNi$ and HfNbTaTiVZr, were irradiated by ion beams to investigate irradiation-induced phase transformation, microstructural evolution, grain growth, as well as phase segregation. The synthesis process of $Al_xCoCrFeNi$ and HfNbTaTiVZr alloys were discussed in section 2.1.2 and 2.1.3, respectively.

2.1.1 Hydroxyapatite

HAp nanoparticles with different particle sizes were synthesized for the grain size effect investigation. The HAp nanoparticle samples were prepared by calcination in a muffle furnace. Bovine bones were boiled in water to remove the organic content, before being calcined in a muffle

furnace at various temperatures of 600°C, 650°C and 1000°C. The temperature increasing rate was 8°C/min and the calcination was maintained for 60 minutes at 600°C, 45 and 60 minutes at 650°C and 60 minutes at 1000°C. After calcination, the sample was furnace cooled to room temperature and ground into fine powders using a mortar and pestle. The powder samples were named as HAp-600C-60min, HAp-650C-45min, HAp-650C-60min, and HAp-1000C-60min.

Densified nanocrystalline HAp samples were fabricated by Spark Plasma Sintering (SPS) method. The HAp nanoparticle powders were loaded into a DR. SINTER LAB Jr. SPS-211Lx furnace and sintered at 700°C for 3 mins under pressure of 60 MPa. SPS processing was conducted in argon atmosphere where oxygen concentration was no higher than 5 parts per million (ppm). The temperature of powder samples was monitored by a K-type thermocouple 2 mm away in the graphite die wall. The heating rate was kept at 200°C/min until sintering temperature was reached. After sintering, a slow cooling rate of 50°C/min was kept until room temperature was reached to prevent pellet cracking.

2.1.2 HfNbTaTiVZr alloy

The HfNbTaTiVZr alloy was synthesized using a vacuum arc melting furnace under a controlled atmosphere of argon in a water-cooled copper hearth. Firstly, the elemental metal powders (purity higher than 99.5 wt. %) were mixed uniformly in a polystyrene ball mixing jar for 15 minutes; then compressed green-body disk was made by pressing the mixed powders in a uniaxial die at 350 MPa. After this, the disk was melted using the arc melter under the controlled condition of argon gas for protection. The sample was flipped over and re-melted 3 to 4 times in order to get the homogeneous composition. The solidified ingots were embedded into an epoxy resin after the system was cooled down, and the sample was cut by a low speed saw to expose a flat surface of the cross-section for future characterization.

2.1.3 $Al_xCoCrFeNi$ alloy

Samples with nominal compositions of $Al_xCoCrFeNi$ (x=0, 1 and 2) HEAs were synthesized by high energy ball milling method in an argon gas environment inside a glove box to protect the powders from oxidation. The pure elements have a purity higher than 99.5% with a size smaller than 40 μm. The elements were put into stainless steel mill pot together with stainless steel balls (8 mm and 12 mm in diameter and 1:4 in weight percentage respectively). The weight ratio of the powders to the grinding ball is 1:5, so the large HEA powders were obtained after ball milling for 10 hours. Then, 5 hours of wet ball milling was used to reduce the size of the large HEA powders. The samples with different Al concentration of x=0, 1, 2 were denominated to be Al-0, Al-1, and Al-2 alloy.

2.2 TEM sample preparation

All of the TEM samples in this dissertation were prepared at the Shared Instrument Facility of Louisiana State University, via different methods: solution-drop for powder samples, microtome-cutting and focus ion beam (FIB) milling for bulk samples. The TEM samples of HAp nanoparticle powders and nanocrystalline $Al_xCoCrFeNi$ powders were prepared by the solution-drop method. A small amount of calcined bone apatite and $Al_xCoCrFeNi$ powders were ground into fine powders using a mortar and pestle, and dispersed in ethanol in an ultrasonic cleaner for 5-10 minutes. Then deposited onto a carbon-coated TEM grid from the top clear liquid in drops, dried in air. TEM samples of densified nanocrystalline HAp were prepared by microtome-cutting method[99]. The sample was washed thoroughly with ethanol to remove the adsorbed oils or water in case of hindering the bonding of the resin to the sample and embedded with the LR white materials in a polyethylene capsule. The sample blocks were then removed from the mold and the resin was removed from the block face until the specimen was exposed using fine SiC paper. The remaining

SiC particles on the sample surface was removed using ethanol before the sample was transferred to the Leica EM UC7 microtome for trimming using a razor blade. The sample was fixed into the microtome arm and initially sectioned using a worn diamond knife until a smooth surface was obtained. Final sectioning was conducted at the set thickness of 50 nm using a new diamond knife.

The TEM samples of HfNbTaTiVZr alloy were prepared via FIB milling method using the Quanta™ 3D Dual Beam™ FEG FIB-SEM and the Gatan Precision Ion Polishing System (PIPS) II (model 695) facilities. For the TEM sample preparation procedures by FIB/SEM, there are seven steps: Pt deposition, Bulk-out, G-cut, Lift-out, Mounting, Thinning and Cleaning. Pt was deposited on the surface of the sample for the protection of damage caused by ion milling in the FIB steps. Bulk-out was conducted by choosing the "regular cross section" and "cleaning cross section" at a tilt angle of 52° of the sample in the chamber to cut a feature around 20 μm (X) × 1.5 μm (Y) × 6 μm (Z). For the "regular cross section" mode, we used 30 kV and 30 nA parameters. And for the "cleaning cross section", the same voltage was used but with a smaller current of 7 nA. For the G-cut, the sample was tilted for 7°, and the cut mode was changed to "rectangles" with 30 kV voltage and a current of 15 nA. The sample was back to the original position, that is to say, there is no tilt for the Lift-out. Insert Omni probe at park, drive to eucentric height, lower the sample and insert Pt GIS needle. Deposit Pt to attach the needle on the surface of the sample and cut the other side using ion beam. Then retract the needle and lift out the sample. The mounting was also conducted at zero tilt and the sample was mounted onto a TEM copper grid. For the thinning, the sample was tilted 50° to 54° and used "cleaning cross section" mode to thin the sample under a very low ion current. A further cleaning step may also be needed. Load the sample into the TEM for observation. If the sample is still too thick, we can use the Gatan PIPS II for a further thinning until the sample is ready for TEM characterization. The PIPS was operated with two Ar+ ion guns ranging from 1

to 5 keV. The samples were milled with 4-5 keV to form a hole. After forming a hole, the sample was finely polished with 1.5 keV for 2 minutes to remove surface damage induced by the ion milling.

2.3 Irradiation experiments

To simulate the irradiation effect of neutrons, alpha-decay and beta-decay events, high energy ion beam and electron beam were used to irradiate the samples. The IVEM-tandem facility at Argonne National Lab and a JEM-2010 transmission electron microscope were used to conduct the irradiation experiments.

2.3.1 IVEM-tandem facility

The IVEM-tandem facility located at Argonne National Lab is a powerful tool to study radiation damage in materials. It consists of a 2 MeV tandem accelerator and ion implanter interfaced to a Hitachi H-9000NAR TEM, allowing *in situ* TEM observation of the radiation effects. The structure of the IVEM and its schematic illustration of the specimen area inside the microscope are shown in Figure 2.1. Figure 2.1 (a) shows the Hitachi H-9000NAR and its associated ion beam line, which linked to a 2-MeV tandem ion accelerator located on the second floor of the building. Figure 2.1 (b) shows the schematic of the sample area of the IVEM, which has a side-entry stage with a slightly expanded objective pole piece that provides room for the ion beam line[100]. The ion dose can be recorded by the ion Faraday cup assembly as shown in Fig. 2.1 (b). The ion beam is oriented to the microscope axis at an angle of 30°, which allows continuous observation of the samples as the beam hits it. The ion species and energy can be selected, which enables the deliberate control of the radiation conditions. A thermocouple attached to the specimen cup is used to measure the sample temperature. And a heating stage allows this facility to conduct the irradiation experiments at a wide range of temperatures.

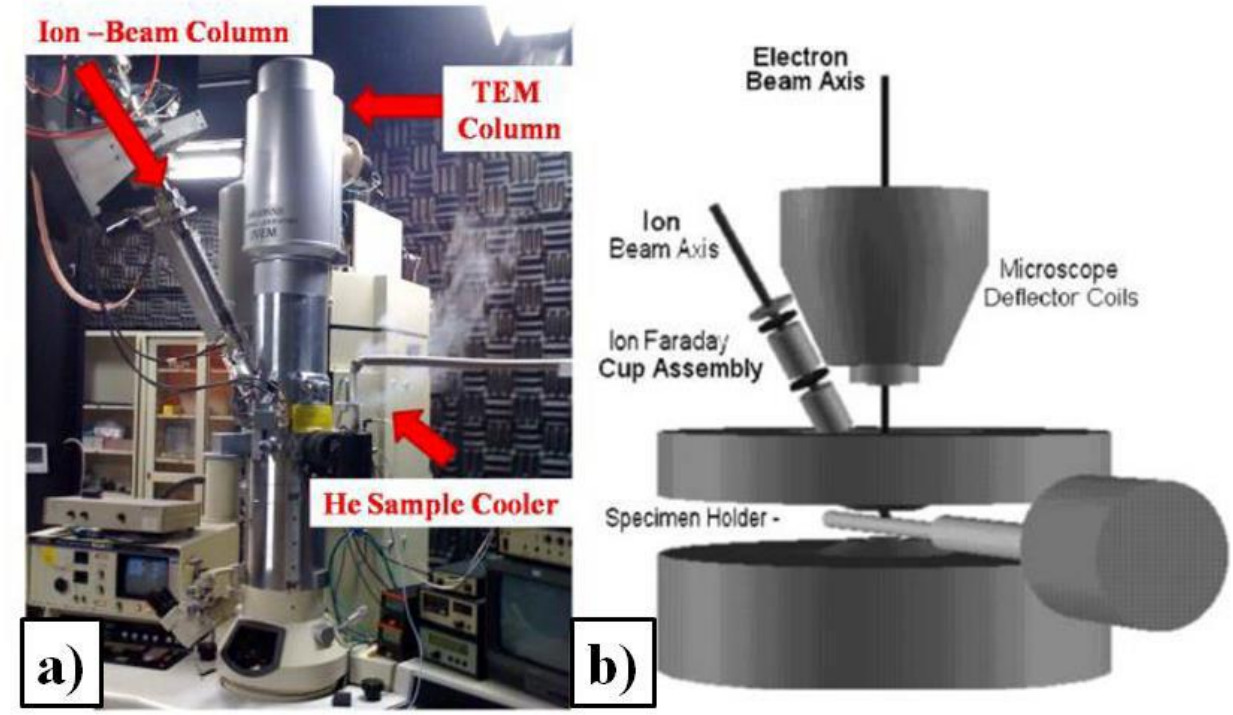

Figure 2.1(a) Intermediate Voltage Electron Microscopy (IVEM)-Tandem facility located at Argonne National Laboratory, (b) schematic of the sample area of the IVEM[100]

2.3.2 Characterization of radiation damage under ion irradiation

Irradiation-induced amorphization, microstructural evolution as well as phase transformation of apatites and high entropy alloys under 1 MeV Kr^{2+} ions irradiation were observed via *in situ* TEM at Argonne National Lab. In order to irradiate the sample simultaneously, the specimen was tilted between 5° and 20° from the electron beam. TEM bright field (BF) images and selected area electron diffraction (SAED) patterns were captured by using imaging plates for the *in situ* observation of the radiation damage under intensive ion bombardment while dark field (DF) images were obtained by inserting an objective aperture to cover the low index diffraction rings of the SAED. Besides, the sample temperature was controlled by a Gatan TEM sample holder so that the irradiation behaviors at different temperatures can be monitored. A Gatan liquid helium (LHe) cooling stage and a Gatan heating stage were used for temperatures between 50 and 250 K, and

between room temperature and high temperature, respectively. The electron beam was turn off to avoid electron beam irradiation damage under ion irradiation and electron diffraction patterns were taken from different areas of the specimen.

2.3.3 Characterization of radiation damage under electron irradiation

The electron-beam irradiation was conducted under an acceleration voltage of 200 kV in a JEOL JEM-2010 TEM at the Shared Instrument Facility of Louisiana State University. Current density was recorded as that on the fluorescent screen, showing the density of electronic charge through the interesting region, and current density was chosen to be J=30 pA/cm^2, 100 pA/cm^2, 120 pA/cm^2, 400 pA/cm^2, respectively. Different radiation conditions were controlled by changing the current density, and the current density was controlled by the diameter of the beam as well as the size of the condenser aperture of the TEM. Microstructural evolution and phase transformation of different sized amorphous HAp specimens (20 nm, 60 nm, and 280 nm) before and after electron beam irradiation were characterized by *in situ* high-resolution TEM and SAED patterns. TEM was also used for the *ex situ* characterization of the apatite and HEA samples before and after irradiation. JEOL TEM 2011 LaB6 equipped with a bottom-mounted Gatan SC1000 CCD camera and an EDAX EDS system was used for the BF image, DF image, high-resolution TEM image and SAED pattern.

2.3.4 Dose calculation and simulation using SRIM software

The doses in the unit of dpa were calculated using the Stopping and Ranges of Ions in Matter (SRIM) software to quantify the radiation damage in apatite and high entropy alloys. SRIM is a Monte Carlo calculation which calculates the interactions of an incident ion with the solid comprising of stationary target atoms. Some parameters needed to be input before the simulation, such as the atomic and mass number for incident and target atoms, initial energy for the incident

ion, displacement energy for the target atom, and the thickness of the target material. Displacement damage of the 1 MeV Kr ions is calculated with the SRIM-2008 program. Based on the SRIM-2008 calculation, ion range (~300 nm) of 1 MeV Kr is greater than the thickness of the samples, meaning all the ions will pass through the sample examined. The SRIM results show the number of displacements produced per unit length per ion and the penetrated depth into the irradiated material. The SRIM code requires the definition of the displacement energy for each element in the material. Irradiation doses were calculated from irradiation fluence based on the following equation, where F_c is irradiation fluence, which can be employed from *in situ* TEM experiments.

$$dpa = \frac{F_c \times [displacements\ by\ single\ ion\ per\ nm] \times 10^3}{[atomic\ density]}$$

When complete amorphization occurs, the critical amorphization fluence was determined by the disappearance of all of the diffraction maximum in the SAED patterns. DPA was converted from the observed critical amorphous fluence using SRIM-2008 simulations using displacement threshold energies of 50 eV for Ca, P, O and H in $Ca_{10}(PO_4)_6(OH)_2$ under a sample density of 3.16 g/cm^3, 50 eV for Mg, Y, Ce, Si, and O in $Mg_2Y_xCe_{8-x}(SiO_4)_6O_2$, which was based on previous theoretical computations[73, 101], and 40 eV for each metal element[102] in high entropy alloys. The damage production for HAp and high entropy alloys under 1 MeV Kr ions by using SRIM software were listed in Appendix A.

2.4 Other Characterization techniques

Other materials characterization techniques like X-ray diffraction (XRD), Scanning Electron Microscopy (SEM) and Energy-Dispersive X-Ray Spectroscopy (EDS) were used for the microstructure and crystal analysis. XRD technique was employed to characterize the apatite and HEA samples before ion irradiation to identify the phase and lattice constant. For the HAp

nanoparticle and $Al_xCoCrFeNi$ alloys, a fine powdered crystalline sample was used for the X-ray powder diffraction experiments. Monochromatic X-rays are diffracted at the small uniformly distributed crystallites in the powder, and a number of crystallites orientated in the right position will meet the Bragg's law for a specific family plane of the crystal structure. For the densified nanocrystalline HAp and HfNbTaTiVZr alloy, a bulk pelleted crystalline sample was used for the diffraction experiments. The crystal structure was characterized by an X-ray diffractometer with the 2θ scan varying from 20°-100° with a scan step of 0.05° at an accelerating voltage of 45 KV and current of 40 mA. SEM technique is a powerful method to study the morphology of the sample. The microstructural evolution and compositional characterization for the HAp and high entropy alloys were investigated using the Quanta™ 3D Dual Beam™ FIB-SEM facility equipped with field emission gun (FEG). The composition of the bulk HfNbTaTIVZr alloy was analyzed by the SEM-EDS and the compositions of the nanoparticle $Al_xCoCrFeNi$ alloys, TEM sample of HfNbTaTIVZr alloy, and HAp were analyzed by the TEM-EDS.

CHAPTER 3 RADIATION-INDUCED AMORPHIZATION OF APATITE UNDER 1 MEV KR^{2+} IONS

This chapter addressed the fundamental understanding of radiation-induced amorphization of apatite structure for the design of radiation tolerant apatite-based ceramic waste form for the disposal of HLW in the advanced nuclear energy systems. The roles of chemical composition, grain size, and interfacial structure on the radiation tolerance of apatite structure were studied. In section 3.1, Ce-doped $Mg_2Y_8(SiO_4)_6O_2$ silicate apatite with different Ce content (Ce=0.5 and 0.05) was used to study the composition effect while the grain size effect was investigated using HAp as a model system by varying the crystallite size ranging from 20 nm to 280 nm, as discussed in section 3.2. A notable size effect was demonstrated in which the radiation tolerance reduced with the decrease of crystallite size due to the excess surface energy. Therefore, a more important question of how different interfaces, more specifically surface and grain boundary, affect the radiation resistance of the apatite waste form was addressed in section 3.3.

3.1 Composition effect on radiation tolerance of silicate apatite

3.1.1 Introduction

The apatite structure has the form of $A^I_4A^{II}_6(BO_4)_6X_2$, where A^I and A^{II} are the two different cationic sites with difference in their local symmetries and atomic scale environments because each A^I cation has nine O atoms as nearest neighbors and each A^{II} cation is surrounded by one anion and six O atoms of three different types. In addition, the A^{II} cations and anions are located in the flexible tunnels[73]. Silicate apatite $Mg_2Y_8(SiO_4)_6O_2$ is an extremely durable material that has important applications in ionic conductors[103, 104] and host phases for actinide immobilization and fission products[105]. As a host phase for actinides, silicate apatite must endure high radiation doses associated with alpha decay of the actinides and beta decay of the

fission products. Natural apatite minerals are greatly resistant to alpha-decay and neutron irradiation[106]. Studying the radiation effects on silicate apatite is of great importance since radiation induced amorphization of silicate apatite results in volumetric swelling and increases the aqueous dissolution rates[107]. The ion beam irradiation-induced amorphization in many different complex oxide structures [108-110] and compositions [16, 111] has been investigated, and numerous models have been developed to explain various aspects of the amorphization process. Radiation stability of materials is very important for their application in nuclear waste forms because the host material's stability and long-term durability can be negatively affected by the radioactive decay of the incorporated radionuclides in nuclear waste which generates displacive and ionizing radiations. Radiation stability may be related with factors like chemical composition[112], different energy loss mechanism[73, 92], structural disorder[96], and grain size[14, 113]. Therefore, the radiation effects in different apatite compositions are very interesting and efforts have been made to study the radiation stability of different apatite composition as nuclear waste forms, like fully phosphate fluorapatite[90], mono-silicate fluorapatite[91], synthetic britholite[92] and fully silicate apatite[93, 94]. Rare-earth silicates with the apatite structure have been observed as actinide host phases in a devitrified borosilicate HLW glass[114], a multiphase ceramic waste form[115], a glass-ceramic waste form[116], and a cement waste form[117]. Radiation effects on $Ca_2RE_8(SiO_4)_6O_2$ have been studied in detail by Cm-doping [118] and ion beam-irradiation experiments [119, 120].

When silicate apatite is used as a nuclear waste host, its chemical composition is changed by the incorporation of radionuclides, which can alter many of the properties of the apatite structure. For instance, the high ionic conductivity of apatite can be achieved by the trivalent cations at the A-sites which resulted in nonstoichiometric composition and disordered anions in the channels at

interstitial sites [121-123]. When smaller atoms were replaced by large atoms at the A-site or B-site, the apatite unit cell usually expanded due to the large unit cell parameters of the large atoms. More importantly, change in the chemical composition may also offer an effective way to improve the material's radiation stability. To understand how the radiation stability of silicate apatite is affected by the incorporation of actinides such as Pu, we performed the ion beam irradiation experiments on two silicate apatite compositions, $Mg_2Y_{7.5}Ce_{0.5}(SiO_4)_6O_2$ (named as Ce-0.5) and $Mg_2Y_{7.95}Ce_{0.05}(SiO_4)_6O_2$ (named as Ce-0.05), in which Cerium is used as a surrogate for Pu [124]. The resulting change in the A^I and A^{II} site composition significantly affects the radiation damage and defect annealing processes in the silicate apatite structure. The bright field images of the two silicate apatite were shown in Figure 3.1.

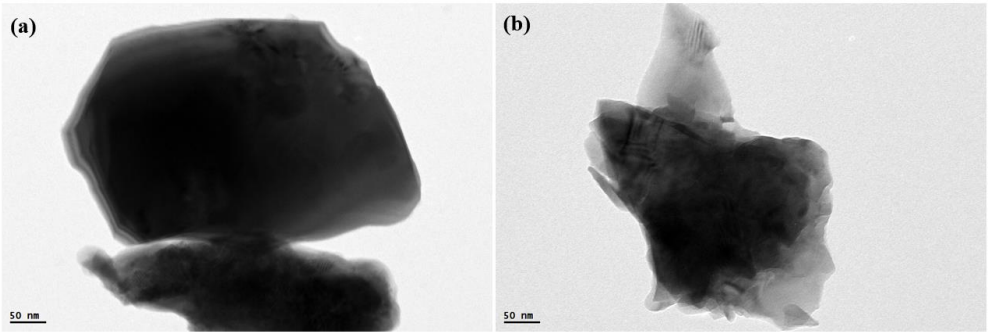

Figure 3.1 Transmission electron microscopy images of (a) $Mg_2Y_{7.5}Ce_{0.5}(SiO_4)_6O_2$ and (b) $Mg_2Y_{7.95}Ce_{0.05}(SiO_4)_6O_2$ silicate apatite

3.1.2 Amorphization process of Ce-doped $Mg_2Y_8(SiO_4)_6O_2$ at room temperature

Ce-doped $Mg_2Y_8(SiO_4)_6O_2$ silicate apatite with different Ce content were irradiated by 1 MeV Kr^{2+} at room temperature. As observed with *in situ* TEM, they all underwent a crystalline/amorphous (c/a) phase transformation under 1 MeV Kr^{2+} irradiation as a result of the ballistic interaction and the subsequent atomic displacements. However, with the varying of the chemical composition, that is the different content of Ce, the critical dose of amorphization changed, which indicates that the radiation ability depends on the composition of the A^I and A^{II}

sites. Figure 3.2 showed a series of TEM dark field images and SAED patterns taken at different ion doses for Ce-0.5 silicate apatite. Figure 3.2 (a) clearly showed the spotted crystalline diffraction pattern and high-contrast TEM dark field image, which indicated the crystalline structure of the pristine Ce-0.5. Small amorphous domains began to appear at a low dose of 0.032 dpa (Figure 3.2 (b)), indicating that the direct ion beam irradiation process may be responsible for amorphization. At a dose of 0.064 dpa, extended radiation damage was observed from TEM dark field image and SAED pattern, in which a significant diffuse halo ring appeared in SAED pattern and accompanied by the weakening of the diffraction pattern (Figure 3.2 (c)). Finally, the TEM dark field image showed a fully amorphous matrix with SAED diffusion halos completely replacing the diffraction spot pattern when the dose reaches 0.096 dpa, which is the critical amorphization dose (D_c) for Ce-0.5 silicate apatite at room temperature. The room temperature ion irradiation of Ce-0.05 showed a similar amorphization process to that of the Ce-0.5 at room temperature, with a lower critical dose of 0.064 dpa. The irradiation-induced amorphization process for Ce-0.05 was shown in Figure 3.3.

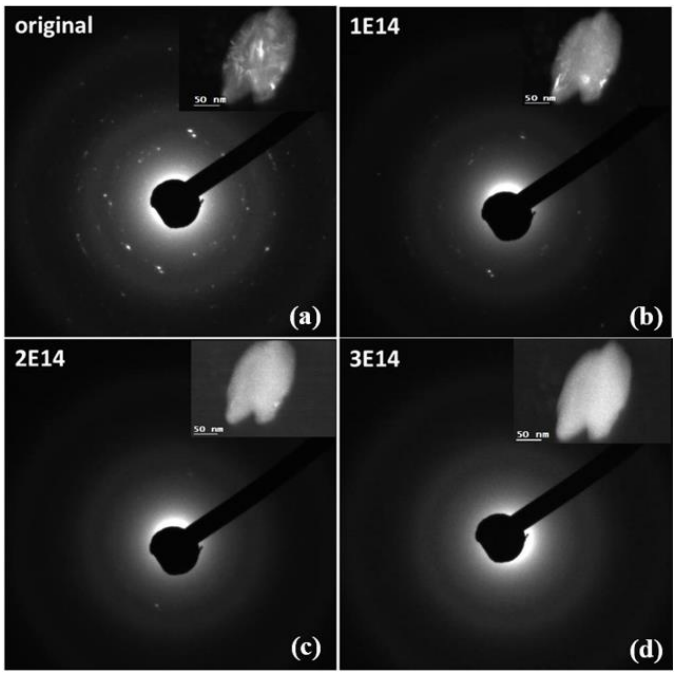

Figure 3.2 Room temperature TEM dark field images and SAED patterns show the 1 MeV Kr^{2+} ion beam irradiation-induced amorphization process of the $Mg_2Y_{7.5}Ce_{0.5}(SiO_4)_6O_2$ silicate apatite. (a) unirradiated, (b) 0.032 dpa (1×10^{14} ions/cm^2), (c) 0.064 dpa (2×10^{14} ions/cm^2), (d) 0.096 dpa (3×10^{14} ions/cm^2)

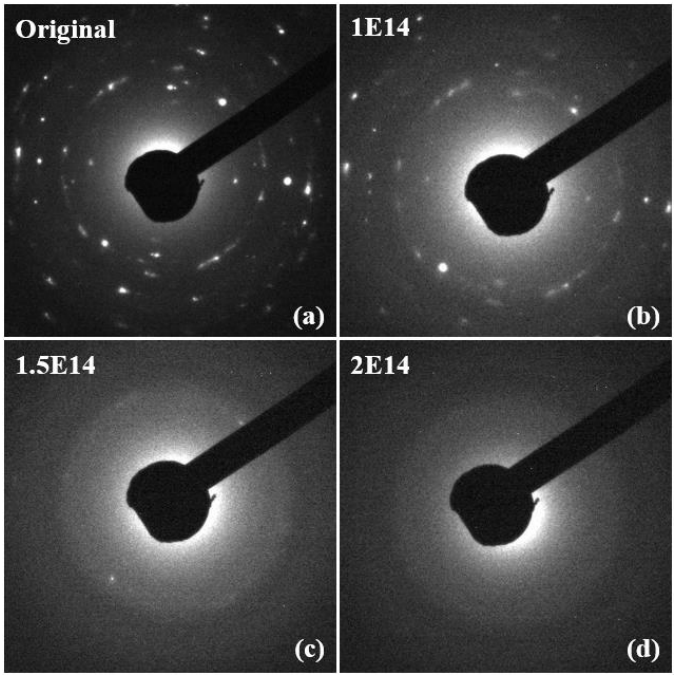

Figure 3.3 Room temperature SAED patterns show the 1 MeV Kr^{2+} ion beam irradiation-induced amorphization process of the $Mg_2Y_{7.95}Ce_{0.05}(SiO_4)_6O_2$ silicate apatite. (a) unirradiated, (b) 0.032 dpa (1×10^{14} ions/cm^2), (c) 0.048 dpa (1.5×10^{14} ions/cm^2), (d) 0.064 dpa (2×10^{14} ions/cm^2)

3.1.3 Temperature dependence on radiation tolerance of silicate apatite

Temperature plays a critical role in the radiation tolerance since it affects the defect dynamics and the radiation damage process. In general, a higher Frenkel pair recombination rate and defect interaction with the material's structure result from the increased mobility of radiation-induced defects at elevated temperature. This process leads to the suppression of radiation damage due to a dynamic annealing effect. When the temperature exceeds a critical value, which the radiation defect production is smaller than the annealing rate, materials that are subject to radiation induced amorphization at room temperature will become highly radiation resistant, *i.e.* the materials can't be amorphized even at extremely high doses. Therefore, the critical temperature (T_c) is an indicator of materials' radiation tolerance, and the lower the T_c is, the higher the radiation tolerance. In order to understand the temperature dependence of the Ce-doped $Mg_2Y_8(SiO_4)_6O_2$ silicate apatite, the two Ce-doped silicate apatite samples, Ce-0.5 and Ce-0.05, were studied using 1 MeV Kr^{2+} ion beam irradiation. The enhanced radiation tolerance at elevated temperature was confirmed by the *in situ* TEM observation for these two silicate apatites. For example, at 798 K, Ce-0.05 remained highly crystalline until the dose reached 0.16 dpa and 0.192 dpa, which is almost 3 times as the critical dose of 0.064 dpa at room temperature, as shown in Figure 3.4.

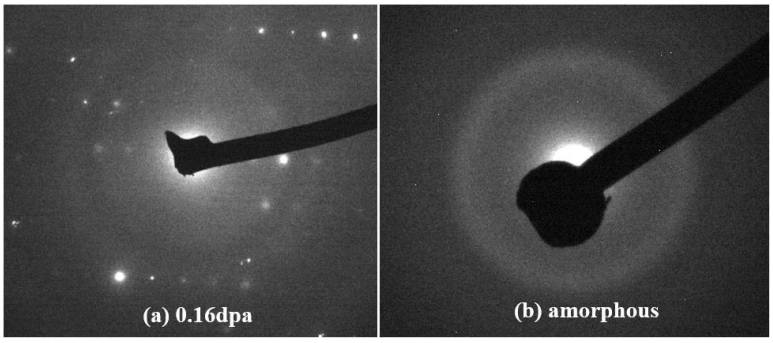

Figure 3.4 SAED patterns of $Mg_2Y_{7.95}Ce_{0.05}(SiO_4)_6O_2$ silicate apatite showing (a) crystallinity at 0.16 dpa (5×10^{14} ions/cm^2) at an elevated temperature of 798 K and (b) amorphization at 0.064 dpa (3×10^{14} ions/cm^2) at room temperature

In addition, *in situ* TEM also showed the significantly different temperature dependence of the irradiation-induced amorphization processes for the two silicate apatites with different Ce content at the A^{I} and A^{II} sites. The Ce-0.5 becomes highly resistant to amorphization above ~ 667 K, whereas the Ce-0.05 can still be amorphized at almost 848 K. The D_c values of these two silicate apatites at different temperature can be seen from Figure 3.5. The temperature dependence curve was fit by an empirical exponential function [20, 125] in the form of

$$D_c = \frac{D_0}{1 - \exp[(E_a/K)(1/T_c - 1/T)]}$$

where D_0 is the critical amorphization dose extrapolated at T = 0 K, E_a is the activation energy for defect annealing, and T_c is the critical amorphization temperature. From the fitting curve, the T_c for Ce-0.5 is 667.5±33 K while T_c for Ce-0.05 is 963.6±64 K. The T_c decreases with the increasing of Ce content (shown in Figure 3.6), which indicates enhanced radiation tolerance with a higher Ce content.

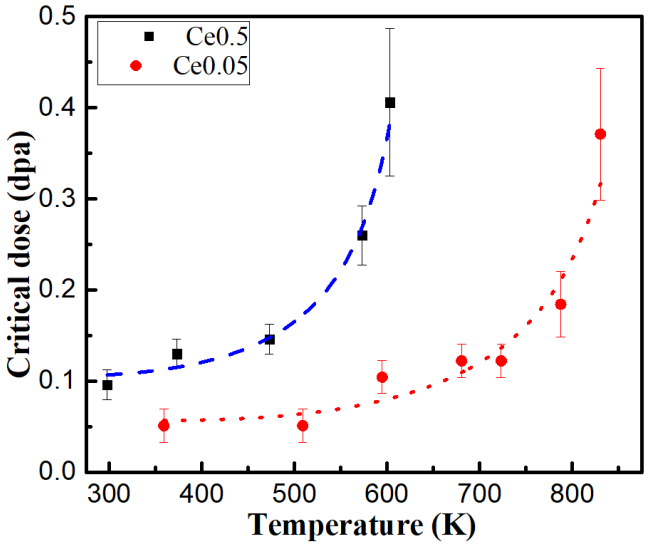

Figure 3.5 Temperature dependence of D_c for Ce-doped $Mg_2Y_8(SiO_4)_6O_2$ silicate apatite

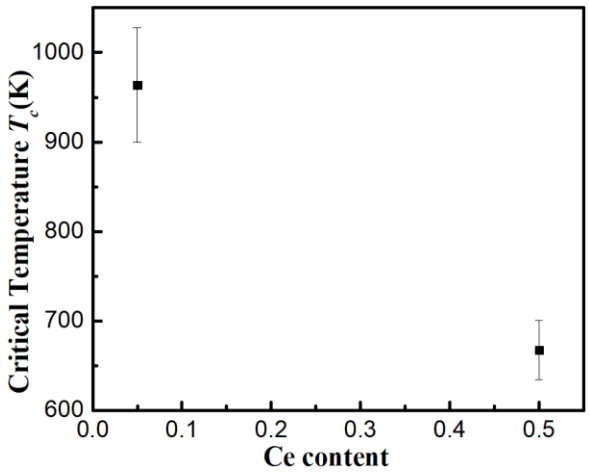

Figure 3.6 T_c dependence on Ce content in Ce-doped $Mg_2Y_8(SiO_4)_6O_2$ silicate apatite

The critical dose varies with the increase of temperature, which is associated with increased defect mobility and recrystallization at the c/a interface of amorphous cascade structures[93]. The process is the result of simultaneous radiation-induced defect production and dynamic recovery process with an activation energy, E_a, which are related to defect migration/recombination in the crystal structure or recrystallization at the c/a interface. It is also noted that the critical dose of Ce-0.5 and Ce-0.05 are close at room temperature but become significantly different at elevated temperature. The critical dose of Ce-0.05 increases to 0.144 dpa while the critical dose of Ce-0.5 largely increases to 0.26 dpa at 573 K, indicating different dynamics of the defect annealing.

3.1.4 Composition dependence on radiation tolerance of silicate apatite

The greater radiation susceptibility to radiation-induced amorphization for $Mg_2Y_{7.95}Ce_{0.05}(SiO_4)_6O_2$ as compared with $Mg_2Y_{7.5}Ce_{0.5}(SiO_4)_6O_2$ may be attributed to the variation of the Ce^{3+} concentration, which results in the change of unit cell volume. The Ce^{3+} ions are completely dissolved in the $Mg_2Y_8(SiO_4)_6O_2$ host lattice without inducing significant changes in the hexagonal crystal structure. However, a higher Ce^{3+} doping concentration leads to an

increase in the apatite lattice parameters, because of the larger ion radius of Ce^{3+} with respect to Y^{3+}. According to Li *et al* [126], the most prominent crystal structure of $Mg_2Y_8(SiO_4)_6O_2$ is the two Y^{3+} ions in 4f (C_3) sites and six Y^{3+} ions in 6h (C_s) sites, while Mg^{2+} ions only occupy the 4f (C_3) site. In addition, a previous study[127] about the crystal structure of $Sr_2Y_8(SiO_4)_6O_2$ indicates that Y^{3+} occupies two different types of cationic sites A^I and A^{II}. According to Blasse's theory[128], the cationic site with free-oxygen nearby prefers to accommodate cations with high charge or small radius in order to compensate the under-bonded valence[129]. Because the ionic radii of Ce^{3+} and Y^{3+} at A^I sites and A^{II} sites are 1.196 and 1.075, 1.07 and 0.96, respectively, the larger Ce^{3+} cations are more likely to occupy A^I sites rather than A^{II} sites. Li *et al* [126] suggested that the unit cell parameters for $Mg_2Y_8(SiO_4)_6O_2$ is a=b=9.280 Å, c= 6.626 Å, and V= 494.13 $Å^3$. The a, c and volume values gradually increase with the increase of Ce^{3+} doping content because of the larger ion radius of Ce^{3+} than Y^{3+}. As a result of the unit cell expansion due to the increase in Ce substitution at A^I site, the radiation tolerance of silicate apatite is enhanced, such that Ce-0.5, having higher Ce^{3+} occupancy at A^I site, are less sensitive to radiation-induced amorphization with relatively lower critical amorphization temperature, as compared to Ce-0.05 with a lower Ce^{3+} occupancy at A^I site. In general, Ce^{3+} content at the A^I site of silicate apatite leads to change of unit cell volume, which may contribute to the enhancement of their radiation stability.

3.1.5 Summary

The radiation response of Ce-doped $Mg_2Y_8(SiO_4)_6O_2$ silicate apatite (Ce=0.05 and 0.5) was investigated by using 1 MeV Kr^{2+} ion beam irradiations at different temperatures, and the cation composition dependence of the radiation tolerance of silicate apatite was studied. The radiation tolerance of silicate apatite $A^I_4A^{II}_6(SiO_4)_6O_2$ can be tailored by controlling the cationic species at the apatite A-site. Increasing Ce^{3+} content at the A^I site of silicate apatite results in the change of

unit cell volume and lattice parameters, which enhances the radiation tolerance of the material. The critical temperature changed from 667.5±33 K of $Mg_2Y_{7.5}Ce_{0.5}(SiO_4)_6O_2$ to 963.6±64 K of $Mg_2Y_{7.95}Ce_{0.05}(SiO_4)_6O_2$. This result highlights that the radiation resistance of apatite can be manipulated through chemical composition control for the design of highly durable nuclear waste forms.

3.2 Size dependence on radiation tolerance of hydroxyapatite nanoparticle

3.2.1 Introduction

Apatite-type structure materials have long been regarded as a candidate host phase for the incorporation of actinides [73, 92-94, 117, 130-133], due to its chemical durability and structural flexibility to incorporate a wide range of radionuclides through cation and anion substitutions. Therefore, the radiation stability of actinide-bearing materials is of great importance considering the potential radiation-induced aperiodic state transformation and α-decay of the actinides. Nano-sized materials have attracted much attention due to the possibility of enhanced radiation tolerance of the materials by mitigating radiation-induced defect accumulation through nanoscale features, such as free-standing open surfaces[75, 134], grain boundaries (GBs)[15, 86, 88, 135], and interfaces[78, 83], which are expected to act as effective sinks for radiation-induced defects, significantly hindering the accumulation of point defects and consequently reduce the overall point defect density. Nanocrystalline spine $MgGa_2O_4$ with grain sizes ranging from 4-12 nm can tolerate doses up to 96 dpa, while its bulk counterpart with an average grain size of 10 μm was amorphized by a dose of just 12 dpa at 100 K[96]. Nanocrystalline TiN had a higher radiation tolerance against amorphization and damage accumulation than its counterpart with coarse grains[97] and a similar observation was also made in nanocrystalline $Gd_2(Ti_{0.65}Zr_{0.35})_2O_7$[17]. Many studies showed the enhanced radiation tolerance upon grain size reduction in metals[136, 137] and ceramics[14, 17,

138].

However, nano-sized materials were not intrinsically radiation resistant and their radiation tolerance was associated with thermodynamic stability of materials [21, 139, 140]. Compared with the characteristics of the corresponding bulk phase, the thermodynamics of phase transitions in nanocrystalline materials can be considerably altered and the thermodynamic properties of nanocrystalline materials are particle-size dependent. Size-related effects and thermodynamic stability have been reported[141, 142]. Experiments showed that bulk zirconia cannot be irradiated at 680 dpa while the nanocrystalline zirconia can be amorphized at a dose as low as 0.9 dpa because of the energetics of the increased surface-to-volume ratio[143]. Si nanocrystals embedded in a matrix of SiO_2 became amorphous under irradiation conditions while bulk silicon did not normally become amorphous[144]. It was also found the radiation resistance decreased with the grain refinement of nanocrystalline SiC[145]. However, HAp and its size effect on the radiation-induced amorphization has never been investigated yet. In this section, we investigated the size effect on the ion-irradiation tolerance properties of HAp with chemical composition of $Ca_{10}(PO_4)_6(OH)_2$ by calcining a series of powders for different grain sizes varying from 20 nm to 280 nm. TEM characterization showed the particles of HAp-600C-60min existed in the form of nano-sized plate and needle with sizes around 20 nm. The size increased with the increase of the calcining temperature and duration, which showed the particle size approximately 60 nm and 80 nm for HAp-650C-45min and HAP-650C-60min, respectively. For HAp-1000C-60min powders, it showed an average particle size of 280 nm with a wide size distribution ranging from 150 nm to 600 nm. The bright field TEM images of these four sized HAp were shown in Figure 3.7.

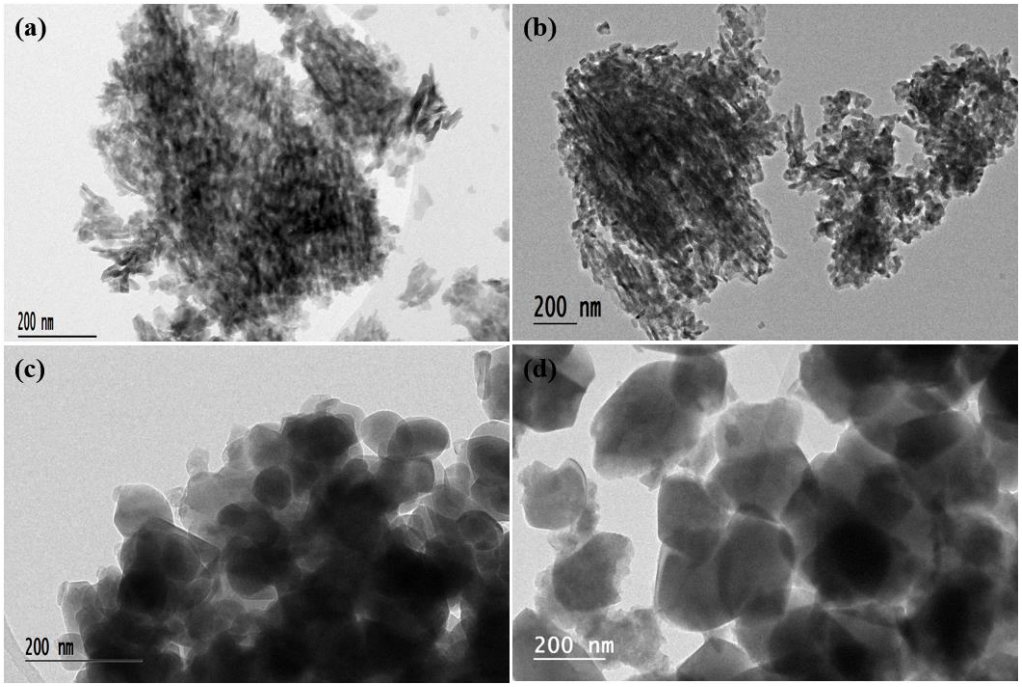

Figure 3.7 Transmission electron microscopy images of different sized hydroxyapatite: (a) 20 nm, (b) 60 nm, (c) 80 nm, (d) 280 nm

3.2.2 Radiation-induced amorphization of hydroxyapatite at room temperature

At room temperature, all the different sized HAp can be amorphized by the 1 MeV Kr^{2+} ion beam, undergoing a crystalline-to-amorphous transition due to the ballistic interaction and the subsequent atomic displacements. TEM images and SAED patterns confirmed radiation-induced amorphization of the 20 nm sized HAp at room temperature (Figure 3.8). The decreased intensity of the diffraction rings and the emerging amorphous halo ring in the SAED patterns upon ion bombardment, as well as the reduced contrast in the dark-filed images, indicated the loss of crystallinity. The structure was completely amorphized at a critical dose of 0.05 dpa (2×10^{14} ions/cm^2) when the dark-field image contrast was lost and the diffraction rings were replaced by the amorphous halos completely. A similar amorphization process was observed for the 60 nm and 80 nm sized HAp, which exhibited a higher critical amorphization dose of 0.075 dpa (3×10^{14} ions/cm^2) (Figure 3.9) and 0.1 dpa (4×10^{14} ions/cm^2) (Figure 3.10), respectively. For the 280 nm

sized HAp, it also showed a similar amorphization process but the amorphization dose was totally different and much higher than the nano-sized HAp at room temperature. The critical amorphization dose was as high as 0.625 dpa (2.5×10^{15} ions/cm^2), which was 12.5 times as the critical amorphization dose of 20 nm sized HAp, indicating that the 280 nm sized HAp showed a better radiation tolerance at room temperature. The amorphization process of 280 nm sized HAp was revealed in Figure 3.11. It is notable that the radiation tolerance decreased as a reduction of grain size at room temperature, indicating a great size effect on the radiation induced amorphization process.

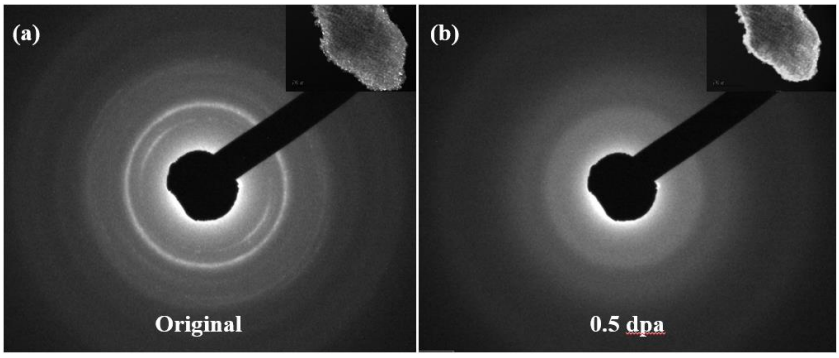

Figure 3.8 TEM dark field images and SAED patterns show 1 MeV Kr^{2+} irradiation-induced amorphization process of 20 nm sized hydroxyapatite at room temperature: (a) the unirradiated and (b) irradiated at 0.05 dpa (2×10^{14} ions/cm^2)

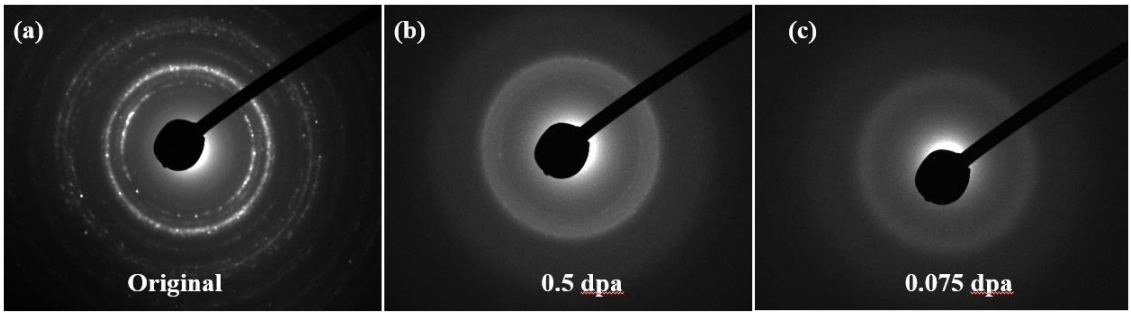

Figure 3.9 SAED patterns show 1 MeV Kr^{2+} irradiation-induced amorphization process of 60 nm sized hydroxyapatite at room temperature: (a) the unirradiated, (b) irradiated at 0.05 dpa (2×10^{14} ions/cm^2), (c) irradiated at 0.075 dpa (3×10^{14} ions/cm^2)

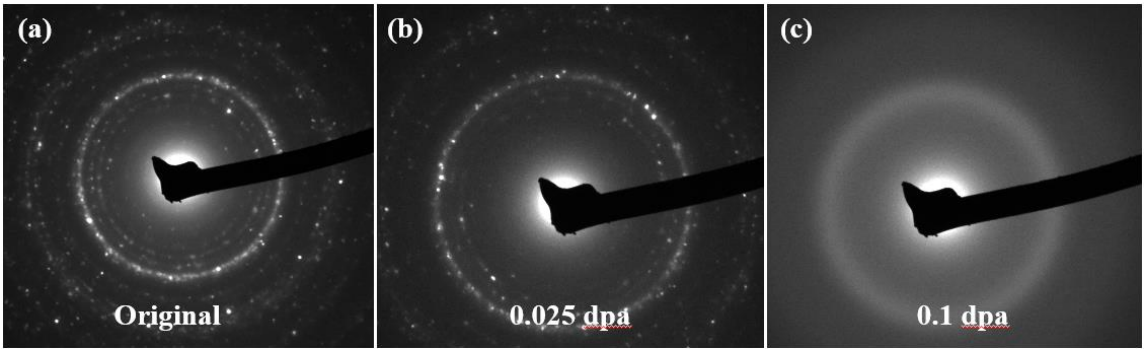

Figure 3.10 SAED patterns show 1 MeV Kr^{2+} irradiation-induced amorphization process of 80 nm sized hydroxyapatite at room temperature: (a) the unirradiated, (b) irradiated at 0.025 dpa (1×10^{14} ions/cm^2), (c) irradiated at 0.1 dpa (4×10^{14} ions/cm^2)

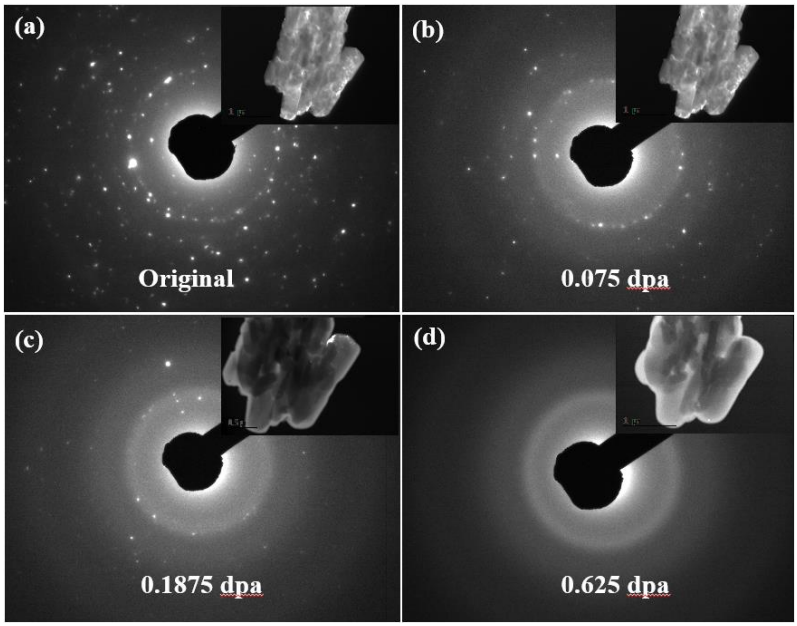

Figure 3.11 TEM dark field images and SAED patterns show 1 MeV Kr^{2+} irradiation-induced amorphization process of 280 nm sized hydroxyapatite at room temperature: (a) the unirradiated, (b) irradiated at 0.075 dpa (3×10^{14} ions/cm^2), (c) irradiated at 0.1875 dpa (7.5×10^{14} ions/cm^2), (d) irradiated at 0.625 dpa (2.5×10^{15} ions/cm^2)

3.2.3 Temperature dependence on the radiation tolerance of hydroxyapatite

The critical dose increased with the increasing temperature in all sized samples, due to the enhanced defect recovery ability at higher temperatures. Temperature is an important factor that directly affects the defect dynamics and the radiation damage process. The dynamic annealing of

radiation defects overtakes the defect production at the critical amorphization temperature (T_c) so that the radiation-induced amorphization cannot occur. Therefore, a higher T_c is associated with lower defect annealing ability and decreased amorphization tolerance. In order to understand the mechanisms controlling the amorphization processes of different sized HAp, a series of 1 MeV Kr^{2+} irradiation experiments were conducted at different temperatures from 50 K to 523 K. *In situ* TEM observation confirmed the enhanced radiation tolerance at elevated temperatures. For example, at 448 K, 60 nm sized HAp remains crystalline at a high dose of 0.1875 dpa (7.5×10^{14} ions/cm^2) (shown in Figure 3.12), which is much higher than its room temperature dose of 0.075 dpa (3×10^{14} ions/cm^2). The temperature dependence curves of the critical amorphization dose of different sized HAp crystallite were plotted in Figure 3.13, showing that the D_c increased with the increase of grain size, where the D_c of the 280 nm sized HAp had the highest dose of 0.625 dpa. It can be fit by an empirical exponential function based on a direct impact model[20, 125], in which the critical amorphization dose D_c is described in the following form:

$$D_c = \frac{D_0}{1 - \exp[(E_a/K)(1/T_c - 1/T)]}$$

Where D_0 is the critical amorphization dose extrapolated at T=0K, E_a is the defect annealing activation energy and T_c is the critical amorphization temperature. The T_c estimated from the curve fitting is 545.5 ± 12.8 K for 20 nm sized HAp, 474.6 ± 0.4 K for 60 nm sized HAp, 403 ± 5 K for 80 nm sized HAp, 316 ± 4 K for 280 nm sized HAp.

Figure 3.13 also showed that amorphous dose gap differed between different sized HAp. Point defects can be eliminated via recombination or annihilation at an interface, surface or grain boundaries. In smaller sized HAp, point defect annihilation at GBs dominates the radiation

response due to a large number of GBs. However, in larger sized HAp, as a result of few numbers of GBs, the predominant mechanism for point defect elimination is recombination. At elevated temperatures, recombination mechanisms become more efficient. Increased amorphous dose is caused by increased recombination rate while the enhanced defects mobility and interstitials eliminating rate will lead to decreased amorphous dose. Therefore, smaller sized HAp exhibits a modest increase while larger sized HAp has a rapidly increase of amorphous dose at elevated temperature. For example, for 20 nm sized HAp, the amorphous dose at 448 K is 0.075 dpa compared with 0.05 dpa at room temperature, the increasing rate is only 50%. However, for 60 nm sized HAp, the amorphous dose is 0.075 dpa at room temperature while it increases to 0.234375 dpa at 448 K, which means the dose increasing rate is 212.5%. The results agree with the rapid amorphous dose increase for a larger sized HAp, showing radiation tolerance of different sized HAp was affected by temperature.

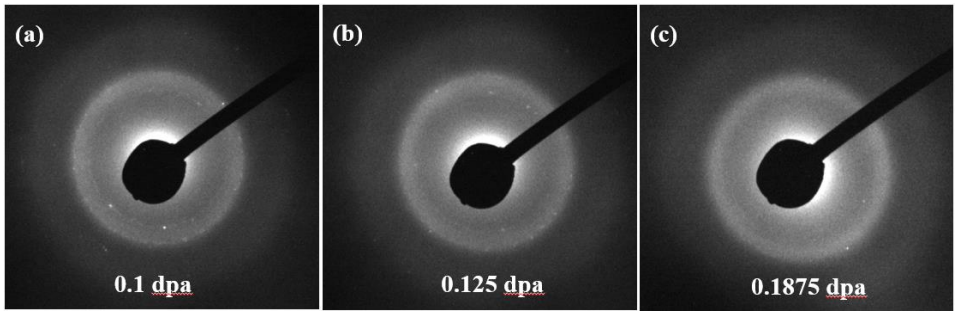

Figure 3.12 SAED patterns show 60 nm sized hydroxyapatite remained crystalline while the dose increased at (a) 0.1 dpa (4×10^{14} ions/cm^2), (b) 0.125 dpa (5×10^{14} ions/cm^2), (c)0.1875 dpa (7.5×10^{14} ions/cm^2)

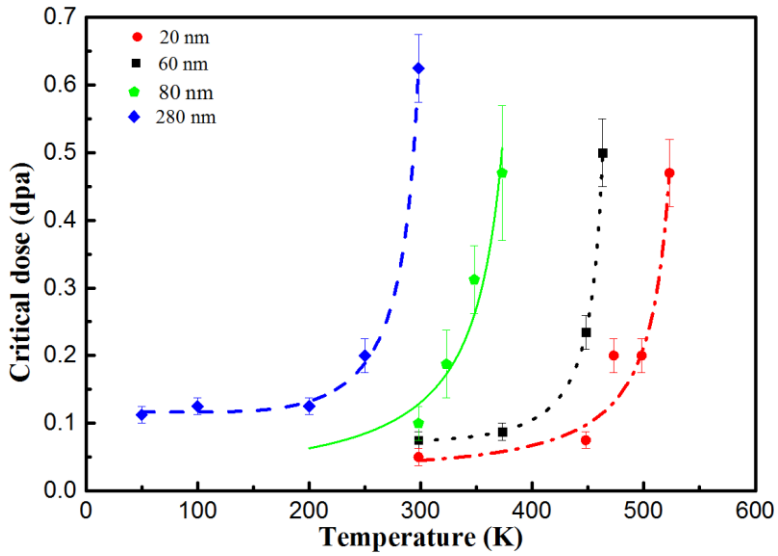

Figure 3.13 Temperature dependence of D_c for hydroxyapatite with different sizes ranging from 20 nm to 280 nm

3.2.4 Size effect on the radiation tolerance of hydroxyapatite

Previous studies showed a T_c value of apatite around 600 K~900 K, such as $Ca_2La_8(SiO_4)_6O_2$ silicate apatite (~700 K)[146], synthetic britholite (880 K~910 K)[92], Ce-doped $Mg_2Y_8(SiO_4)_6O_2$ silicate apatite (667.5 K~963.6 K) (as revealed in section 3.1), and $Ca_{10}(VO_4)_6F_2$ fluorapatites (~603 K)[73]. In contrast, the 280 nm sized HAp (~316 K) in this section showed much lower T_c and higher D_c than them, suggesting a better radiation tolerance of HAp compared with many other apatite compositions. However, T_c increased significantly from 316 K of 280 nm sized HAp to 545 K of 20 nm sized HAp, which means reduced radiation tolerance with the reduction of particle size. This phenomenon was demonstrated by the 60 nm and 80 nm sized HAp, which 60 nm sized HAp showed a higher T_c of 474 K compared to the T_c of 80 nm sized HAp (403 K). This result was interesting because it showed that a smaller sized HAp did not necessarily lead to higher radiation tolerance. As grain size decreased from 60 nm to 20 nm, T_c increased from 474.6 K to 545.5 K, indicating decreased radiation tolerance actually. Such a reduced radiation tolerance in ultrafine HAp nanoparticles indicated that nanostructured HAp materials were not intrinsically

radiation tolerant, and it is possible an optimized size regime may exist that can display the greatest radiation tolerance against displacive irradiation induced amorphization. In ceramics, amorphization process can proceed via a variety of mechanisms, including direct-impact, double-cascade overlap, direct impact/defect stimulated growth and defect accumulation[147]. Direct impact/defect stimulated (DI-DS) amorphization mechanism may favor materials with larger grain sizes, since GBs may be more easily amorphized than the bulk[145]. However, damage accumulation model favors fine-grained materials[145], which have a higher concentration of GBs sinking for point defects. Equally important is the thermodynamic aspect of the phase stability in nanostructured materials, in which the excess interface energy in ultra-fine nanostructures may significantly alter the phase-stability landscape of the materials, which interplays with the nonequilibrium radiation conditions to affect the phase transformation behavior of the materials.

The less radiation resistant ability of 20 nm sized HAp than the 280 nm sized ones may be explained by the excess surface energy as a result of the reduced particle size. Phase transitions during irradiation are usually associated with point defects, defect complexes, chemical disorder, and lattice strain, which provide the driving force for a phase transition to higher-energy crystalline or amorphous state by increasing the total free energy of a crystal[148]. Kinetically, the high fraction of interfaces (e.g. free-standing open surface and GBs) in nanostructured materials can offer more preferential sites for defects migration and annihilation, which can improve the radiation tolerance of the materials[81, 137]. However, thermodynamically, the high density of interfaces also carries a large interface energy that increases the total free energy of the materials, [21]. The radiation performance of the nanomaterials is thus largely determined by the competition between the kinetic and thermodynamic factors. In the smaller sized HAp nanoparticles, the higher surface energy and hence higher total energy can significantly lower the energy barrier between

the crystalline phase and amorphous state, tipping the balance of phase transformation under radiations in favor of amorphization, similar to previous studies of nano-sized zirconia[21, 149]. As the HAp particle size was reduced from 280 nm to 20 nm, the excess surface energy exceeded the sink effect to become the dominant factor in determining the phase stability, effectively decreased the radiation tolerance. Under displacive ion irradiation, atomic displacement cascades introduced a large number of defects that further increased the free energy of the system, eventually overcoming the energy difference between the amorphous and crystalline states, leading to the amorphization of crystalline HAp nanoparticles.

3.2.5 Summary

Different sized HAp particles ranging from 20 nm to 280 nm were prepared by calcination. Ion beam induced irradiation amorphization process was studied by 1 MeV Kr^{2+} ion irradiation. Critical dose increased with the increase of grain size at room temperature, which is 0.05 dpa, 0.075 dpa, 0.1 dpa and 0.625 dpa for 20 nm, 60 nm, 80 nm, and 280 nm sized particles respectively. Critical temperature T_c decreased with the increase of the size, e.g. 545.5±12.8 K for 20 nm and 316±4 K for 280 nm, indicating reduced radiation tolerance. The radiation tolerance dependence on grain size was discussed in the context of kinetics and thermodynamic factors. The reduced radiation tolerance in smaller sized HAp particles, which is in sharp contrast to the previously reported enhanced radiation stability in nanostructures, may be attributed to its excess surface energy which lowers the energy difference between the amorphous state and the crystalline phase and therefore facilitates the displacive radiation-induced amorphization, lending strong support to the importance of critical size in optimizing nanostructured materials design for extreme radiation conditions.

3.3 Interface effect on radiation tolerance of nanostructured hydroxyapatite

3.3.1 Introduction

Another critical but still less understood factor in the radiation behavior of nanostructured materials is the type of interface present in the materials. Interfaces such as surfaces and grain boundaries[84-89] can serve as sinks for absorbing and annihilating radiation-induced defects in materials. Studies[150, 151] showed the effect of the surface on irradiation-induced damage in bulk materials and pointed out fewer defect clusters were observed inside bulk materials compared with large numbers of defect clusters near the surface. Void denuded zones near the surface of Ni foil under irradiation were also reported[152]. However, due to the complex interplay between composition, interface and radiation condition in determining the radiation damage evolution, nanostructured materials[14, 75, 134] may not be intrinsically radiation tolerant as demonstrated in the example of HAp nanoparticles in section 3.2. Based on the foundings in section 3.2, it is thus necessary to narrow down the investigation to focus on how the interface, particularly surface and grain boundary, affects the radiation tolerance of nanostructured HAp with the same grain size. In this section 3.3, in order to understand the effect of interfacial structure on the radiation tolerance of HAp, HAp nanoparticles with large free-standing open surface areas and densified nanocrystalline HAp with densified grain boundaries, both of the same grain size, were irradiated with 1 MeV Kr^{2+} ions at temperatures ranging from 150 K to 523 K, to reveal the little understood impact of interface.

3.3.2 Specimens characterization by XRD and TEM

Crystal structures of HAp nanoparticles and densified nanocrystalline HAp were analyzed using X-ray diffractometer with Cu-κα radiation of wavelength λ=0.154 nm and operating at 45 kV and 40 mA. The θ-2θ scans in the range of 5°-70° with a step of 0.02° and scan speed of 5°/min

were performed. Measured x-ray diffraction patterns for HAp nanoparticles and densified nanocrystalline HAp were shown in Figure 3.14, which showed the HAp structure. The (hkl) Miller indices were assigned which matched the HAp X-ray PDF card number 00-009-0432. In addition, XRD peaks of densified nanocrystalline HAp became sharp after SPS compared with the ones of HAp nanoparticles, suggesting the improved crystallinity.

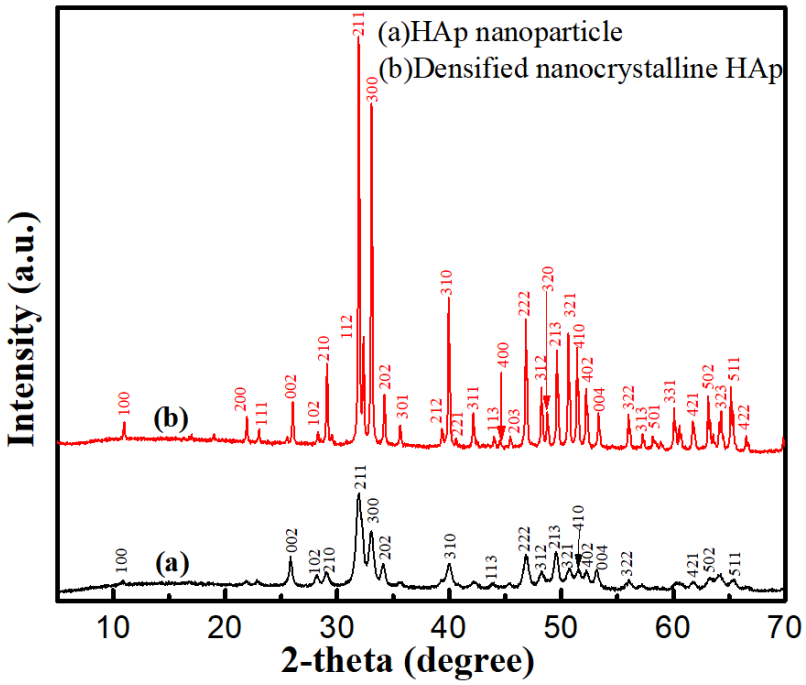

Figure 3.14 XRD pattern obtained from hydroxyapatite nanoparticle and densified nanocrystalline hydroxyapatite samples (For interpretation of the references to color in this figure legend, the reader is referred to the web version of this article)

The morphologies and structures of HAp were further studied via the TEM techniques, and the bright field TEM images and SAED patterns were shown in Figure 3.15. The grain size of HAp nanoparticles and densified nanocrystalline HAp was around 20 nm after measuring more than 50 random grains and taking an average value. Figure 3.15 (a)(b) showed the structure of HAp nanoparticles at different magnifications, in which showed a high density of free-standing open surfaces whereas a high fraction of densified grain boundaries was exhibited for densified

nanocrystalline HAp, as shown in Figure 3.15 (d)(e). The improved crystallinity of densified nanocrystalline HAp was further confirmed by comparing two diffraction patterns (Figure 3.15 (c)(f)), as more and sharp crystalline spots and rings were observed in SAED pattern of densified nanocrystalline HAp. To quantify the crystallinity percent of HAp nanoparticles and densified nanocrystalline HAp, the fraction of the crystalline phase (X_c) of HAp samples were evaluated by the following equation[153], where I_{300} is the intensity of (300) diffraction peak and $V_{112/300}$ is the intensity of hollow between (112) and (300) diffraction peaks of HAp. The crystallinity of HAp nanoparticles and densified nanocrystalline HAp was determined to be 23.5% and 66.2%.

$$X_c = 100 * \frac{I_{300} - V_{112/300}}{I_{300}}, [\%]$$

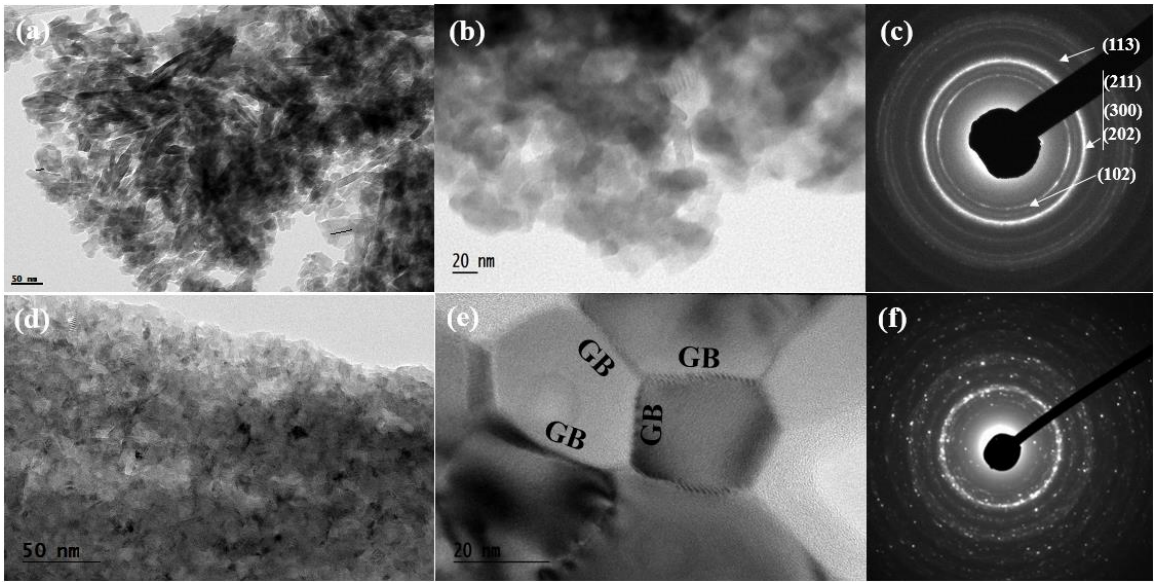

Figure 3.15 Transmission electron microscopy bright field images of (a) (b) hydroxyapatite nanoparticle and (d) (e) densified nanocrystalline hydroxyapatite; SAED patterns of (c) hydroxyapatite nanoparticle and (f) densified nanocrystalline hydroxyapatite

3.3.3 Radiation-induced amorphization at room temperature

HAp nanoparticle and densified nanocrystalline HAp were irradiated with 1 MeV Kr^{2+} at room temperature. As a result of the ballistic interaction and subsequent atomic displacements, they all

underwent a crystalline/amorphous (c/a) phase transformation via *in situ* TEM observation. However, the amorphous dose changed with the different interfacial structure of HAp. Figure 3.16 showed a series of SAED patterns taken at different ion doses for densified nanocrystalline HAp. The crystalline structure was shown clearly by the spotted diffraction pattern in Figure 3.16 (a). Small amorphous domains began to appear at a low dose of 0.025 dpa (Figure 3.16 (b)), indicating that the direct ion beam irradiation process is responsible for amorphization. Extended radiation damage was observed from the SAED pattern, in which a significant amorphous halo ring appeared and accompanied by the weakening of the diffraction pattern at a dose of 0.05 dpa (Figure 3.16 (c)). In the final, when the dose reached 0.075 dpa (Figure 3.16 (d)), which is the critical amorphization dose (D_c) at room temperature, the diffraction spot pattern was replaced completely by the SAED amorphous halo rings. Room temperature ion irradiation of HAp nanoparticle showed a similar amorphization process, while with a little lower critical dose of 0.05 dpa, suggesting the better radiation tolerance of densified nanocrystalline HAp. The irradiation-induced amorphization process for HAp nanoparticle was shown in Figure 3.17.

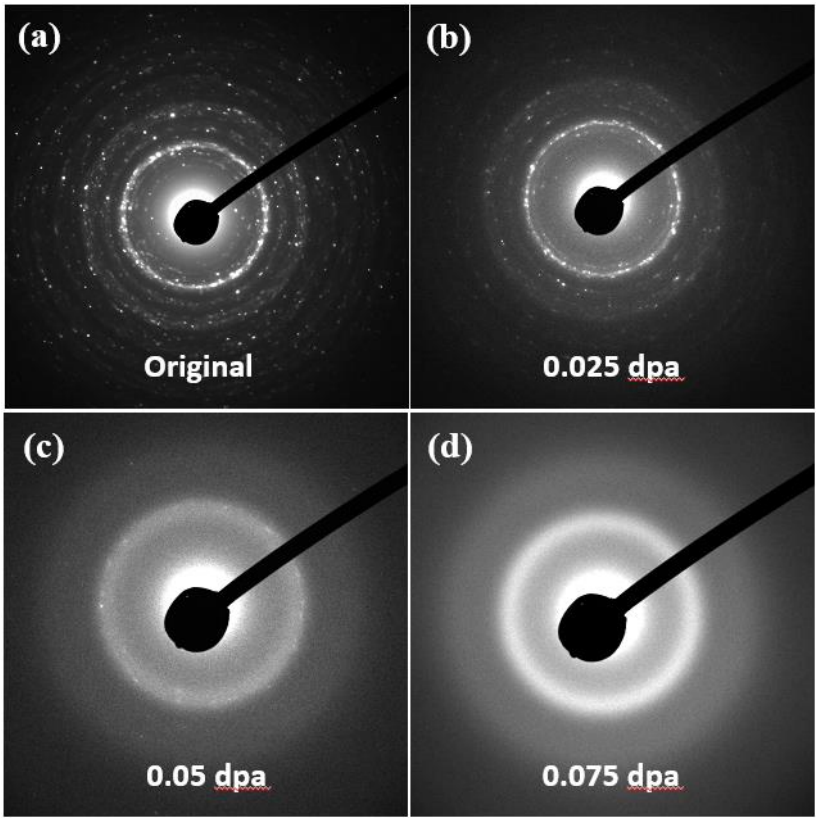

Figure 3.16 Room temperature selected area diffraction patterns show the 1 MeV Kr^{2+} ion beam irradiation induced amorphous process of densified nanocrystalline hydroxyapatite (a) unirradiated, (b) 0.025 dpa (1×10^{14} ions/cm^2), (c) 0.05 dpa (2×10^{14} ions/cm^2), (d) 0.075 dpa (3×10^{14} ions/cm^2)

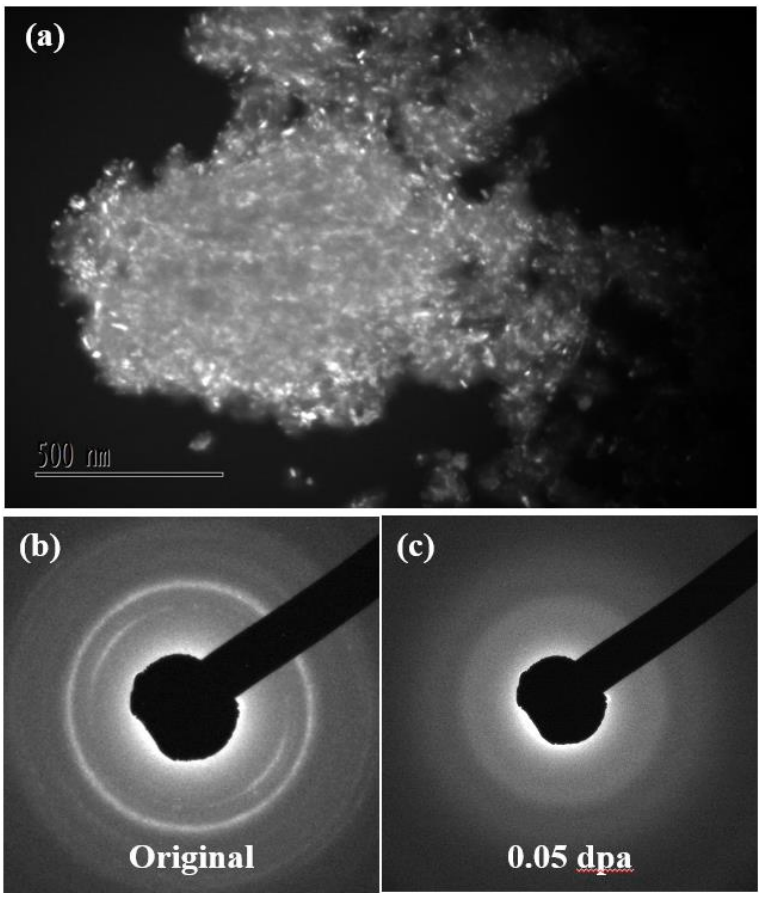

Figure 3.17 Room temperature (a) dark field image and (b) (c) selected area diffraction patterns show the 1 MeV Kr^{2+} ion beam irradiation induced amorphous process of hydroxyapatite nanoparticle: (b) the unirradiated, (c) 0.05 dpa (2×10^{14} ions/cm^2)

3.3.4 Irradiation response at elevated temperatures

Temperature plays an important and direct effect on the radiation stability of materials since it directly affects the defects dynamics and radiation damage process. The mobility of radiation-induced defects and defects recombination rate increase at elevated temperatures, resulting in the suppression of radiation damage due to defects annealing effect, which also leads to a higher amorphization dose. In order to understand temperature dependence on radiation tolerance, HAp nanoparticles and densified nanocrystalline HAp were irradiated at different temperatures ranging from 150 K to 525 K with 1 MeV Kr^{2+} ions. The temperature dependence on radiation tolerance was shown in Figure 3.18, based on a direct impact model [20, 125, 154] and the curve was fit via

an empirical exponential function listed in the following equation. In this equation, E_a means defects annealing activation energy, D_0 means critical amorphization dose extrapolated at T= 0K, and T_c means the critical amorphization temperature.

$$D_c = \frac{D_0}{1-\exp[(^{Ea}/_{K})(^{1}/_{T_c}-^{1}/_{T})]}$$

T_c was determined to be 545 K ± 12.8 K for HAp nanoparticles and 437 K ± 4 K for densified nanocrystalline HAp, respectively. T_c is a very important parameter that can directly determine the radiation tolerance of materials and usually, a lower T_c value means a higher radiation tolerance. The physical meaning of T_c is that at a temperature point at which recombination rate equals the radiation damage rate, and amorphization process is unlikely to occur over this temperature limit, as demonstrated by the crystalline point in Figure 3.18. The materials will be extremely radiation resistant when the irradiation temperature is over the T_c point. According to Figure 3.18, it was obvious that critical amorphization dose increased with the increase of temperature, suggesting the enhanced radiation tolerance at elevated temperatures, which was also confirmed via *in situ* TEM observations. For instance, densified nanocrystalline HAp at 423 K remained highly crystalline with a dose of 0.7 dpa that is almost 7 times compared to the one at room temperature.

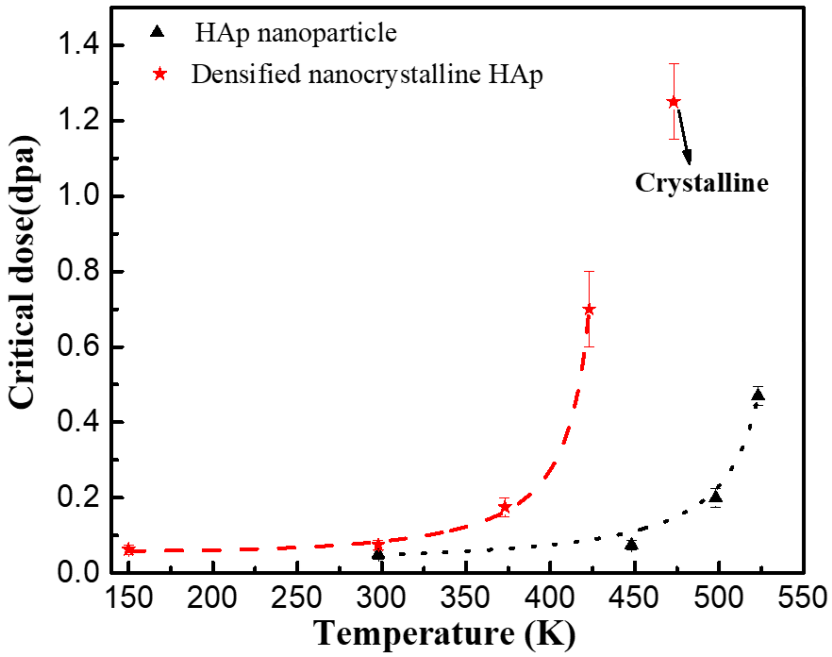

Figure 3.18 Temperature dependence of D_c for hydroxyapatite nanoparticle and densified nanocrystalline hydroxyapatite

To further understand the irradiation effects near T_c, densified nanocrystalline HAp was also irradiated at 473 K, which is over the T_c value, and compared with the irradiation behaviors at 423 K. The c/a phase transformation at 423 K was shown and revealed by the SAED patterns and associated dark field images, which SAED patterns were replaced by the amorphous halos and dark field images lost its contrast due to the loss of crystallinity at a dose of 0.7 dpa. The radiation-induced amorphization process was revealed in Figure 3.19. However, when irradiated at 473 K (above T_c), the sample remained its crystalline structure even at a high dose of 1.25 dpa, indicating the sample cannot be amorphized finally at this temperature, as shown in Figure 3.20. Defects behaviors showed a big difference between 473 K and 423 K since point defects at 473 K are more mobile and have much higher recovery rate, suppressing the accumulation of radiation-induced defects which will, in turn, affect the final radiation-induced amorphization process.

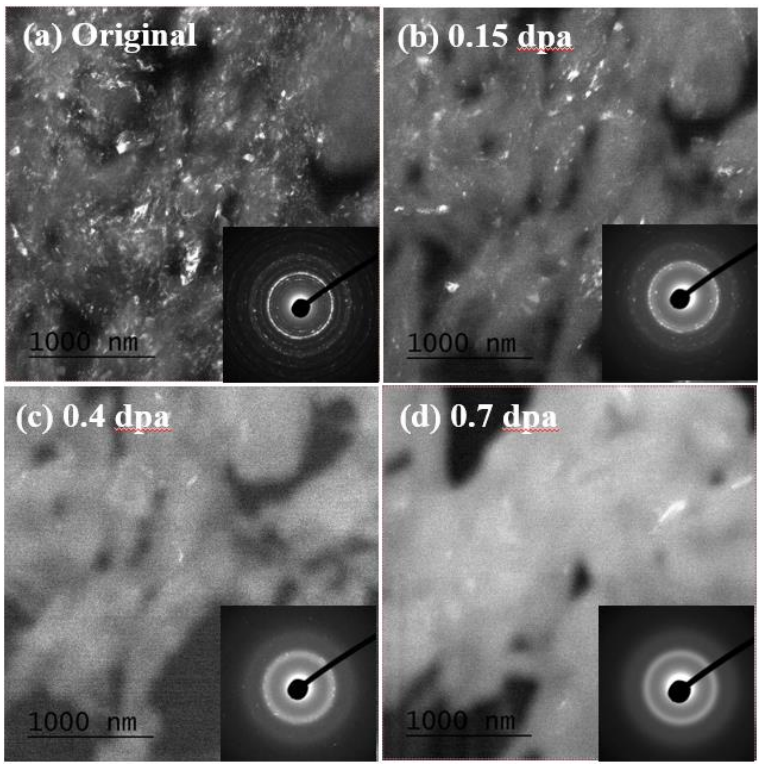

Figure 3.19 TEM dark filed images and SAED patterns show the 1 MeV Kr^{2+} ion beam irradiation induced amorphous process of densified nanocrystalline hydroxyapatite at 423 K (a) unirradiated, (b) 0.15 dpa (6×10^{14} ions/cm^2), (c) 0.4 dpa (1.6×10^{15} ions/cm^2), (d) 0.7 dpa (2.8×10^{15} ions/cm^2)

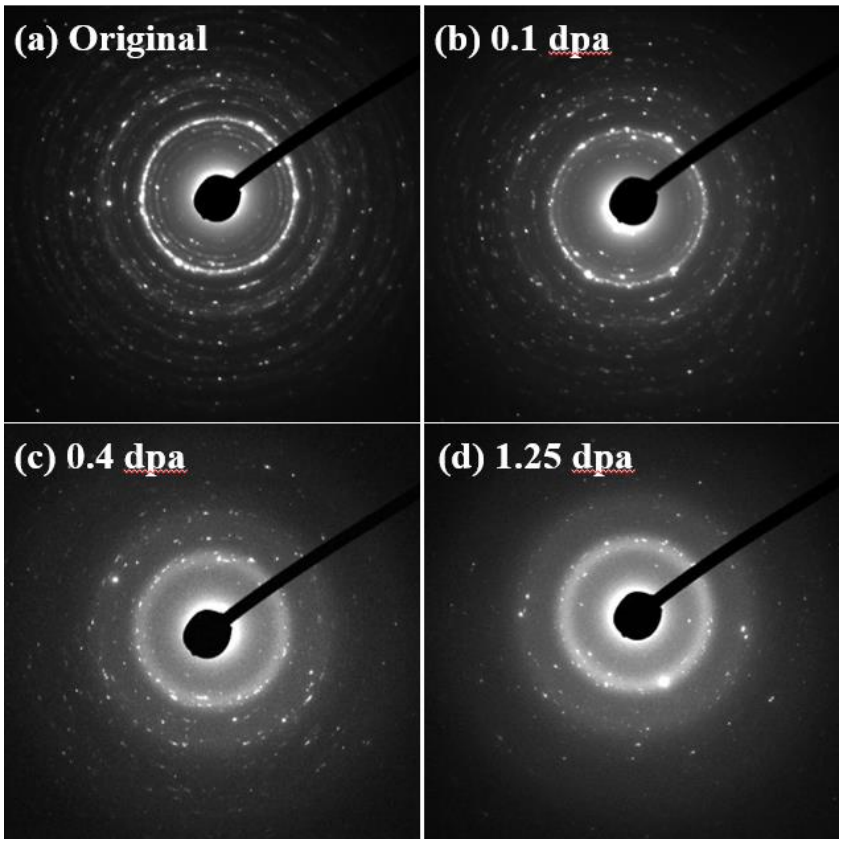

Figure 3.20 SAED patterns show the 1 MeV Kr^{2+} ion beam irradiation process of densified nanocrystalline hydroxyapatite at 473 K: (a) unirradiated, (b) 0.1 dpa (4×10^{14} ions/cm^2), (c) 0.4 dpa (1.6×10^{15} ions/cm^2), (d) 1.25 dpa (5×10^{15} ions/cm^2)

3.3.5 Interface effect on the radiation tolerance

In contrast to the findings in HAp nanoparticles in section 3.2, irradiation data of densified nanocrystalline HAp showed higher radiation resistant with significantly higher D_c and a much lower T_c (~437 K). Since both free-standing open surfaces and grain boundaries behave as effective sinks for radiation-induced point defects such as vacancies and interstitials, their presence in nanostructures can greatly enhance the migration and recombination of defects, and thus could make a strong contribution to the mitigation of radiation damage, as expected in the theory of nanostructure-enhanced radiation tolerance. Upon irradiation, open surfaces and GBs have a stronger loading ability for interstitials than vacancies, so interstitials are loaded into the GBs or

open surfaces, which can act as a source that emits interstitials to annihilation vacancies in the bulk. This recombination mechanism showed great efficiency to annihilate immobile vacancies in the nearby bulk, leading to a self-healing ability for the radiation-induced damage. However, as both free surfaces and grain boundaries exhibit similar sink strength, apparently, the drastic difference between the radiation tolerance of HAp nanoparticles and densified nanocrystalline HAp cannot be explained by defect kinetics alone. The mechanism is attributed to the thermodynamic factor, particularly the interface energy carried by different microstructures. Free-standing open surfaces carry more dangling bonds than densified grain boundaries structures since GBs are bonded together and significantly different from the isolated bonds in the open surfaces. It was demonstrated that the grain boundary energy[155] or surface free energy[156] increased with the increasing of dangling bonds numbers or density at GBs or surfaces, which means a higher excess energy will exist in the material with a higher amount of dangling bonds. Some studies[157-159] also showed free surfaces of HAp carried a much higher energy than grain boundaries, which is on a magnitude of 10^6 higher. As free surfaces carry significantly higher interface energy as a consequence of higher density of dangling bonds than grain boundaries, the energy barrier between the amorphous state and crystalline phase are lower in HAp nanoparticles than densified nanocrystalline HAp with the same grain size, resulting in the less radiation tolerant of HAp nanoparticles. In addition, the difference in crystallinity in the HAp specimens may also contribute to the difference in radiation tolerance, similar to the previous studies of other ceramic materials [154, 160-163], .

3.3.6 Summary

Densified nanocrystalline HAp and nanoparticulate HAp were synthesized through spark plasma sintering and calcination, respectively. Ion irradiation experiments with 1 MeV Kr^{2+} were

conducted for densified nanocrystalline HAp and HAp nanoparticle with the similar grain size of ~20 nm, at temperatures between 150 K and 523 K. The critical amorphization temperature (T_c) was determined to be 545K ± 12.8K, 437K ± 4K for HAp nanoparticle, densified nanocrystalline HAp, respectively. The enhanced radiation tolerance of densified nanocrystalline HAp was attributed to the lower interface energy as a result of the densified grain boundary as compared to the free surfaces of the nanoparticles, which contributes to the higher thermodynamic stability and hence higher resistance to radiation damage, highlighting the importance of interfacial structure to the radiation tolerance of nanostructured materials.

CHAPTER 4 ELECTRON-IRRADIATION-INDUCED RECRYSTALLIZATION OF HYDROXYAPATITE

4.1 Introduction

Nature apatite minerals are highly resistant to beta-decay and neutron irradiation. Crystalline-to-amorphous phase transformation of waste forms under displacive ion irradiation has been studied [73, 93, 117, 130, 154, 164] and a size effect on the ion-beam-irradiation-induced amorphization was found on monazite[14]. Similar to amorphization process, electron-beam-irradiation-induced behaviors may also have a noticeable size effect[14], critical recrystallization fluence increased with the increase of particle size. Alpha-decay of actinides, as well as beta-decay of fission products, were produced by high level nuclear waste. Waste forms must endure high doses alpha-decay of the actinides and beta-decay of the fission products for the purpose of immobilization. To investigate the effect of beta decay events on the apatite structure, electron irradiations were performed for different sized HAp under different radiation conditions. Contrary to displacive ion induced amorphization, electron-beam irradiation has been reported to enhance defect recovery, nucleation and recrystallization through ionization and electronic excitation process in $SrTiO_3$[108], $Ca_2La_8(SiO_4)_6O_2$[93], Al_2O_3[165], $CaZrTi_2O_7$, $Gd_2Ti_2O_7$[19], $LaPO_4$, $ScPO_4$[166]. Electron-beam irradiation also has a key role in microstructural evolution, phase transformation and thermodynamic properties in materials.

Study of electron-beam-induced effects in amorphous $Sr_2Nd_8(SiO_4)_6O_2$ silicate apatite under different voltages and temperatures showed an ionization-induced recrystallization process[131, 132, 167]. Direct observation of electron beam induced nucleation and growth in amorphous GaAs showed crystallization rate was closely related to current density of electron beam[168]. Study of the amorphous $Gd_2Zr_2O_7$[169] showed thermally activated ionization process for the recrystallization mechanism. In this chapter, for a better understanding of irradiation behaviors of

HAp under beta-decay events, electron-beam irradiation experiments were conducted under different radiation conditions by changing the current density to simulate the effects of beta-decay. This chapter systematically studied the electron-beam-irradiation-induced recrystallization behaviors of different particle sized HAp and a notable size dependence on the recrystallization process was observed. Furthermore, *in situ* TEM observation showed the recovery process, phase transformation, crystal nucleation and growth, and microstructural evolution of the 1 MeV Kr^{2+} ion-irradiation-induced amorphous HAp under 200 keV electron beam irradiation. The amorphous-to-crystalline phase transformation kinetics for different sized HAp and electron-irradiation-induced recrystallization mechanisms were also investigated. In addition, nanocrystalline materials have been revealed to be more inclined to ion-irradiation-induced amorphization as a result of excess surface energy leading to a more stable amorphous state, thus study of electron-irradiation revealing the defects-recovery kinetics may help to counter-balance this thermodynamic de-stability[14].

4.2 Ionizing irradiation induced recrystallization

The pre-amorphized HAp samples by 1 MeV Kr^{2+} ions were irradiated by 200 kV electron beam under different radiation conditions to study the e-beam induced irradiation behaviors at room temperature. Different radiation conditions were controlled by changing the current density, and different particle sizes varying from 20 nm to 280 nm were performed to investigate the size dependence on the irradiation performances. All samples studied in the present work were considered to have transformed into the amorphous state from the crystalline structure after 1 MeV Kr^{2+} ions irradiation. For simplicity, the samples were noted as HAp-20nm, HAp-60nm, and HAp-280nm based on the particle size. Microstructural evolution of HAp-20nm under the current density of 100 pA/cm^2 (6.25×10^8 e^- cm^{-2} s^{-1}) was revealed in Figure 4.1, showing a clear

amorphous-to-crystalline (a/c) phase transformation. Before electron irradiation, the purely amorphous phase was shown via the high-resolution TEM image and SAED pattern (Figure 4.1 (a)), where no obvious grains were observed from the high-resolution TEM image and no distinct extra diffraction rings or spots can be observed from the inserted SAED pattern. At the same region, a/c phase transformation began around 180 s (1.125×10^{11} e^-/cm^2) as some random nanocrystals nucleated (marked by arrows) shown in Figure 4.1 (b). More nucleation and further grain growth were observed with a continuous electron irradiation to 540 s (3.375×10^{11} e^-/cm^2) (Figure 4.1 (c)). A completed a/c phase transformation was reached after electron irradiation to 1120 s (7×10^{11} e^-/cm^2), where grains with an average grain size of 4.6 nm surrounded in the irradiated amorphous matrix and had a random orientation (as shown in Figure 4.1 (d)). The SAED pattern after electron fluence of 7×10^{11} e^-/cm^2 was defined and shown in Figure 4.1 (e), showing it is still the HAp structure after recrystallization. Two plausible explanations[170] for this HAp structure: first, the amorphous material may still have a structure that remains a memory of the original crystal structure; second, the SAED technique is not sensitive to low concentration of residual crystalline material which can act as seeds for the recrystallizing phase.

Microstructural evolution of HAp-20 nm under the current density of 400 pA/cm^2 (2.5×10^9 $e^- cm^{-2} s^{-1}$) was revealed in Figure 4.2, where nucleation began at a much earlier stage of 60 s (1.5×10^{11} e^-/cm^2) (Figure 4.2 (a)) and a/c phase transformation also completed at an earlier stage of 910 s (2.275×10^{12} e^-/cm^2) (Figure 4.2 (b)) as compared to the current density of 100 pA/cm^2. However, the final average grain size increased to 6.5 nm with a random orientation, which was further confirmed by the SAED pattern (Figure 4.2 (c)), showing a more discreet diffraction rings as compared to the complete rings (Figure 4.1 (e)). A shorter-range ordering created by the partial bond breaking process under the low current density will form the smaller sized structure as

compared to the larger sized structure as a result of longer free paths and larger collision probability for the atoms under the high current density[171].

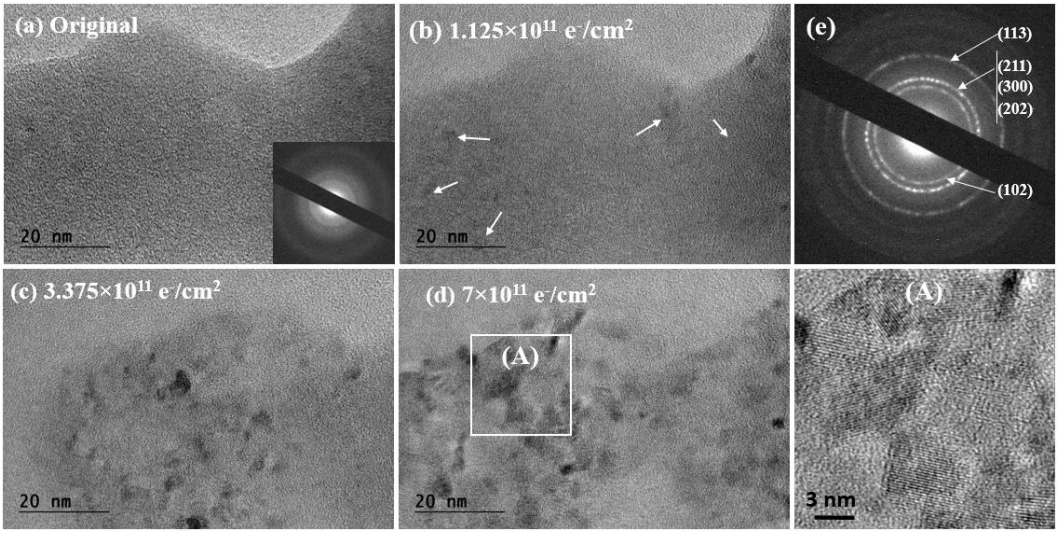

Figure 4.1 Microstructural evolution of ion-irradiation-induced amorphous hydroxyapatite $Ca_{10}(PO_4)_6(OH)_2$ with a particle size of 20 nm under the 200 keV electron irradiation at room temperature shown via *in situ* high resolution TEM images: (a) 0 s, (b) 180 s (1.125×10^{11} e^-/cm^2), (c) 540 s (3.375×10^{11} e^-/cm^2), (d) 1120 s (7×10^{11} e^-/cm^2), (e) selected area diffraction pattern after electron fluence of 7×10^{11} e^-/cm^2, showing the crystal nucleation and growth process. Current density was fixed at 100 *p*A/cm^2 (6.25×10^8 e^- cm^{-2} s^{-1})

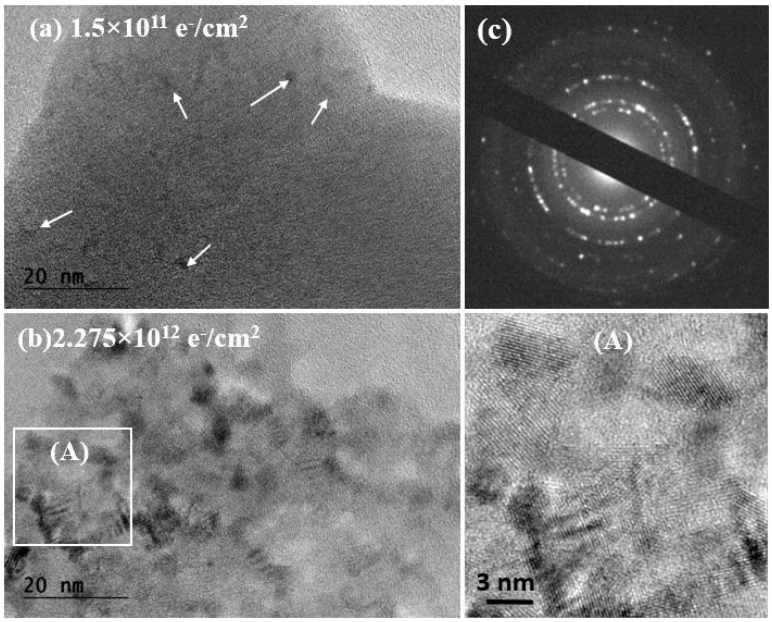

Figure 4.2 Microstructural evolution of ion-irradiation-induced amorphous hydroxyapatite

(fig. caption cont'd)

$Ca_{10}(PO_4)_6(OH)_2$ with a particle size of 20 nm under the 200 keV electron irradiation at room temperature shown via *in situ* high resolution TEM images: (a) 60 s (1.5×10^{11} e^-/cm^2), (b) 910 s (2.275×10^{12} e^-/cm^2), (c) selected area diffraction pattern after electron fluence of 2.275×10^{12} e^-/cm^2, showing the crystal nucleation and completion process. Current density was fixed at 400 *p*A/cm^2 (2.5×10^9 e^- cm^{-2} s^{-1})

A similar a/c phase transformation of HAp-60nm under the current density of 30 *p*A/cm^2 (1.875×10^8 e^- cm^{-2} s^{-1}) and 120 *p*A/cm^2 (7.5×10^8 e^- cm^{-2} s^{-1}) were revealed in Figure 4.3 and Figure 4.4, respectively. For the current density of 30 *p*A/cm^2, nucleation began around 84 s (1.575×10^{10} e^-/cm^2) and a/c phase transformation completed around 900 s (1.6875×10^{11} e^-/cm^2) with the final average grain size of 4.3 nm in a random orientation. However, an earlier nucleation stage around 70 s (5.25×10^{10} e^-/cm^2) and completion stage around 720 s (5.4×10^{11} e^-/cm^2) were also observed for a higher current density 120 *p*A/cm^2. A larger grain size of 7 nm under a higher current density of 120 *p*A/cm^2 was demonstrated by comparing the SAED patterns of Figure 4.3 (e) and Figure 4.4 (c), which more discontinuous rings were shown.

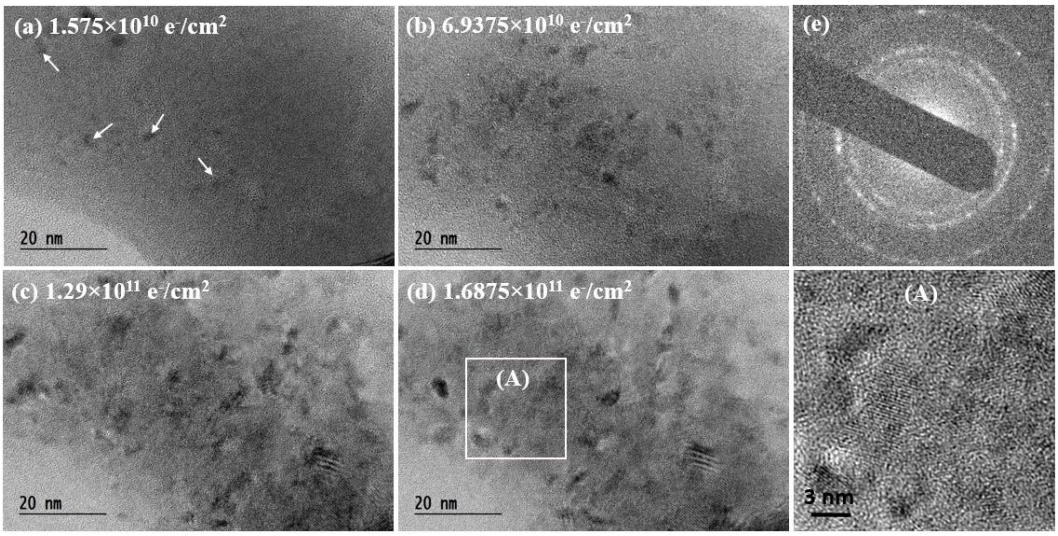

Figure 4.3 Microstructural evolution of ion-irradiation-induced amorphous hydroxyapatite $Ca_{10}(PO_4)_6(OH)_2$ with a particle size of 60 nm under the 200 keV electron irradiation at room temperature shown via *in situ* high resolution TEM images: (a) 84 s (1.575×10^{10} e^-/cm^2), (b) 370 s (6.9375×10^{10} e^-/cm^2), (c) 688 s (1.29×10^{11} e^-/cm^2), (d) 900 s (1.6875×10^{11} e^-/cm^2), (e) selected area diffraction pattern after electron fluence of 1.6875×10^{11} e^-/cm^2, showing the crystal nucleation and growth process. Current density was fixed at 30 *p*A/cm^2 (1.875×10^8 e^- cm^{-2} s^{-1})

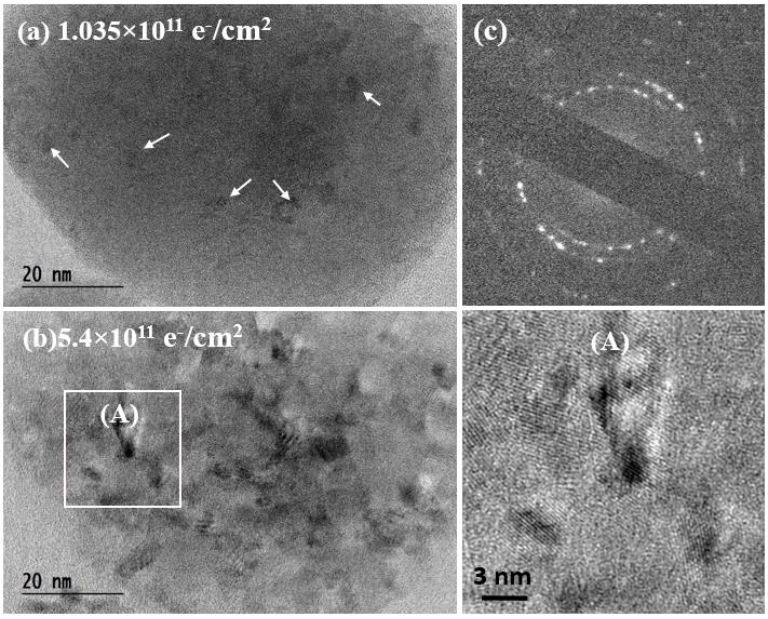

Figure 4.4 Microstructural evolution of ion-irradiation-induced amorphous hydroxyapatite $Ca_{10}(PO_4)_6(OH)_2$ with a particle size of 60 nm under the 200 keV electron irradiation at room temperature shown via *in situ* high resolution TEM images: (a) 138 s (1.035×10^{11} e^-/cm^2), (b) 720 s (5.4×10^{11} e^-/cm^2), (e) selected area diffraction pattern after electron fluence of 5.4×10^{11} e^-/cm^2, showing the crystal nucleation and completion process. Current density was fixed at 120 *p*A/cm^2 (7.5×10^8 e^- cm^{-2} s^{-1})

Microstructural evolution of HAp-280nm under the current density of 30 *p*A/cm^2 was revealed in Figure 4.5, where nucleation began at 180 s (3.75×10^{10} e^-/cm^2) and a/c phase transformation completed at 1200 s (2.25×10^{11} e^-/cm^2) with an average grain size of 5.3 nm in a random orientation. However, a quite different phenomenon was observed for HAp-280nm under the current density of 120 *p*A/cm^2. A coarse grain sized crystal in the orientation of (211) pattern nucleated at 350 s (2.625×10^{11} e^-/cm^2). The coarse grain sized crystal and nanocrystals coexist in the irradiated amorphous matrix when a/c phase transformation completed at 900 s (6.75×10^{11} e^-/cm^2), indicated by the coexistence of the diffraction spots and rings in the inserted SAED pattern in Figure 4.6 (d), suggesting the polynucleation process for HAp-280nm under the higher current density of 120 *p*A/cm^2. Study of electron irradiation of 800 keV Kr^{2+} ion-irradiation-amorphized F-rich apatite with single crystals over a range of beam energies and beam currents showed that

amorphous apatite crystallized to a coarse-grain sized apatite at 85-200 keV and fine-grain sized CaO can be formed by increasing the beam current while the crystallization of apatite was not observed even at high doses[172]. Another study also revealed the formation of CaO under the electron irradiation at 300 keV and 400 keV. However, the formation of the coarse-grain sized CaO structure in the present study may not be possible since the operating voltage of the electron irradiation was only 200 keV. Although the displacement energy for O is less than 100 keV, energy between 100 keV and 400 keV was required for Ca[173]. Therefore, the coarse sized crystal should still be the HAp structure while not CaO structure.

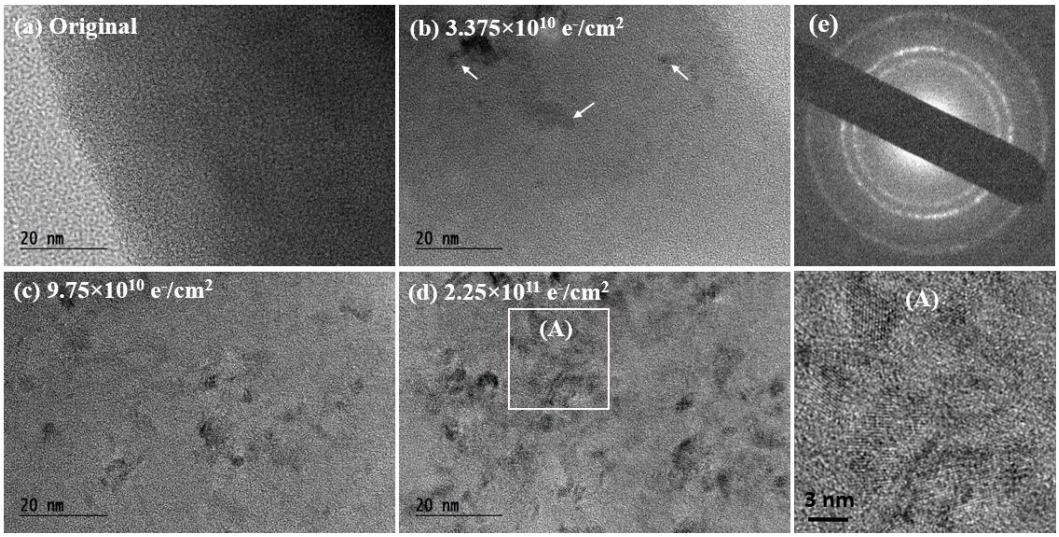

Figure 4.5 Microstructural evolution of ion-irradiation-induced amorphous hydroxyapatite $Ca_{10}(PO_4)_6(OH)_2$ with a particle size of 280 nm under the 200 keV electron irradiation at room temperature shown via *in situ* high resolution TEM images: (a) 0 s, (b) 180 s (3.375×10^{10} e^-/cm^2), (c) 520 s (9.75×10^{10} e^-/cm^2), (d) 1200 s (2.25×10^{11} e^-/cm^2), (e) selected area diffraction pattern after electron fluence of 2.25×10^{11} e^-/cm^2, showing the crystal nucleation and growth process. Current density was fixed at 30 *p*A/cm^2 (1.875×10^8 e^- cm^{-2} s^{-1})

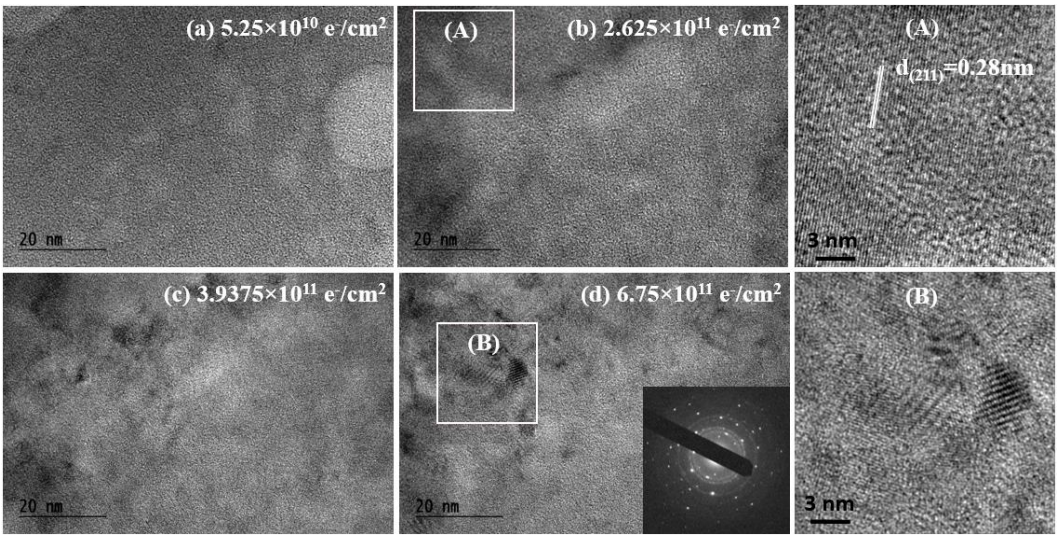

Figure 4.6 Microstructural evolution of ion-irradiation-induced amorphous hydroxyapatite $Ca_{10}(PO_4)_6(OH)_2$ with a particle size of 280 nm under the 200 keV electron irradiation at room temperature shown via *in situ* high resolution TEM images: (a) 70 s (5.25×10^{10} e^-/cm^2), (b) 350 s (2.625×10^{11} e^-/cm^2), (c) 525 s (3.9375×10^{11} e^-/cm^2), (d) 900 s (6.75×10^{11} e^-/cm^2), showing the crystal nucleation and growth process. Current density was fixed at 120 *p*A/cm^2 (7.5×10^8 e^- cm^{-2} s^{-1})

4.3 Size dependence

A recent study of monazite[14] showed a slower recrystallization rate was observed for the larger sized sample as compared to the smaller sized sample under 200 keV electron irradiation, suggesting a notable size dependence on the electron-irradiation-induced recrystallization. In this dissertation, recrystallization behaviors of different particle sized HAp, *i.e.* 20 nm, 60 nm and 280 nm, were compared under the same radiation condition (current density 30 *p*A/cm^2). The size dependence on the recrystallization fluence was revealed in Figure 4.7, which showed the smallest critical and complete recrystallization fluence for HAp-20nm. The critical and complete recrystallization fluence were determined to be 1.125×10^{10} e^-/cm^2 and 1.22×10^{11} e^-/cm^2 for HAP-20nm, 1.65×10^{10} e^-/cm^2 and 1.75×10^{11} e^-/cm^2 for HAP-60nm respectively while they are 3×10^{10} e^-/cm^2 and 2×10^{11} e^-/cm^2 for HAP-280nm, as listed in Figure 4.8. The critical recrystallization fluence was the fluence that needed to induce the nucleation for the a/c phase transformation while

the complete recrystallization fluence was the fluence that needed to finish the a/c phase transformation. The curve of recrystallization percent as a function of electron fluence showed a characteristic sigmoidal shape. It was also notable that higher electron fluences were required to induce and complete the a/c phase transformation for larger sized HAp samples.

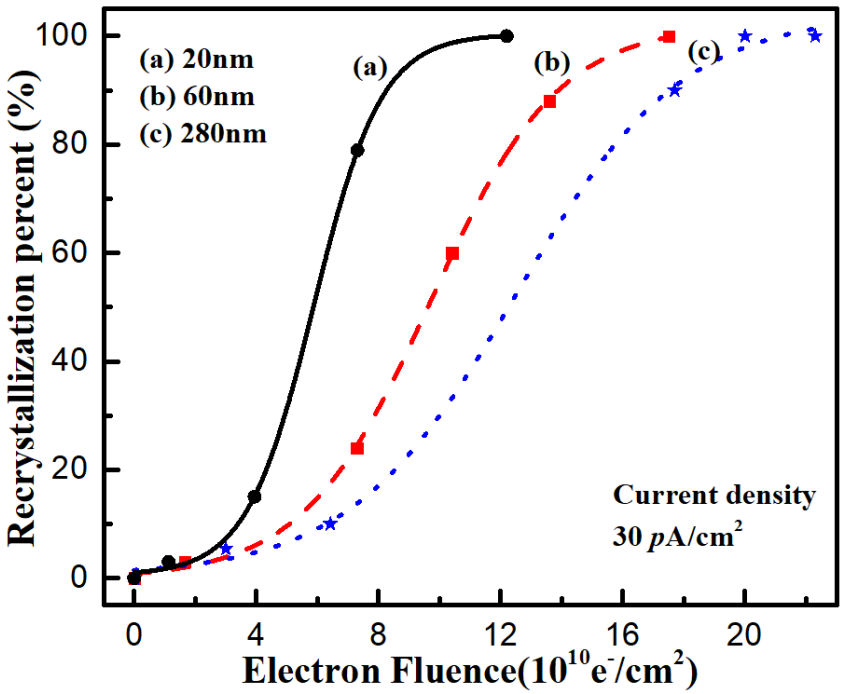

Figure 4.7 Solid phase regrowth of amorphous to crystalline transition as a function of electron fluence of 20 nm, 60 nm and 280 nm sized amorphous HAP under 200 kV electron irradiation at current density of J=30 *p*A/cm^2 (1.875×10^8 e$^-$ cm^{-2} s^{-1})

The recrystallization process induced by the electron irradiation was greatly affected by the interfaces and surfaces of materials. Recrystallization behaviors showed difference in planar interfaces (continuous layer) and irregular shaped a/c interfaces (isolated regions) as a result of the interface effects[174]. Compared to the planar interfaces, the irregular shaped interfaces may offer more preferential sites for recrystallization, and the dangling bonds along the interfaces may also cause the electronic excitation stimulated recrystallization[175]. The large surfaces of the HAp nanoparticles here exhibited a similarity with the isolated regions along the interfaces. Generally,

the surface areas of materials increased with the reduction of particle size. Compared to 60 nm sized HAP, 20nm sized HAp exhibited more free-standing open surfaces and more prominent surface effects such that the high fraction of dangling bonds at the surface provided more sites for the recrystallization nucleation and significantly enhanced the recrystallization process. The ~280 nm sized HAp nanoparticles showed less surfaces than the 20 and 60 nm sized ones, hence fewer sites can be provided for the recrystallization, which required a much higher critical and complete recrystallization fluence for the a/c phase transformation. Other studies showed the recrystallization fluence for many materials are on a magnitude of more than 10^{20} e^-/cm^2, such as 3.6×10^{21} (200 keV e-beam) for apatite[132], 3.65×10^{21} (120 keV e-beam) for $ScPO_4$[176], 1.69×10^{23} (200 keV e-beam) for zircon[17] and more than 1.5×10^{20} (200 keV e-beam) for $CePO_4$[14]. In this dissertation, the recrystallization fluence was revealed to be only on a magnitude of 10^{10} e^-/cm^2 for HAp, suggesting a better defect recovery ability under the events of beta-decay.

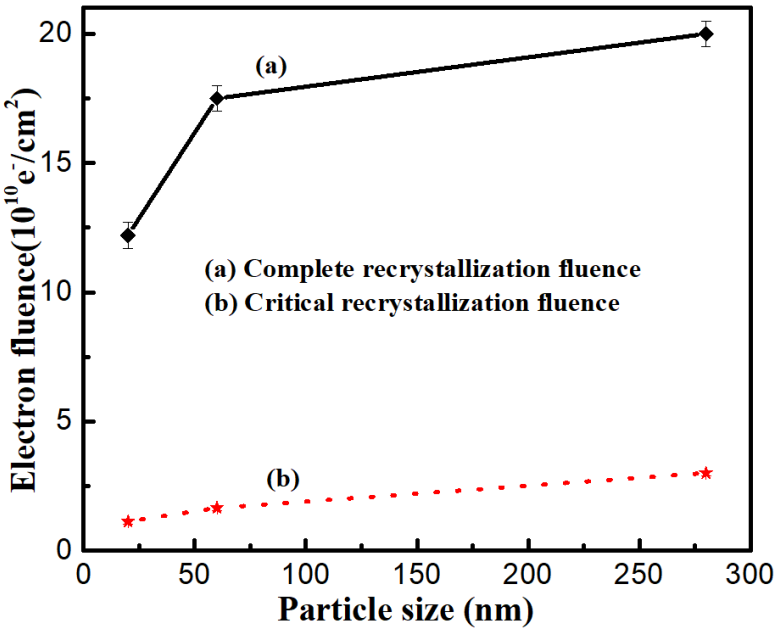

Figure 4.8 Size dependence on the critical and complete recrystallization electron fluence

4.4 Transformation kinetics

To quantitatively study the recrystallization process, the percent of recrystallization in the amorphous sample was recorded at different electron fluences. The percent of recrystallization versus electron fluence curve manifested itself in a characteristic sigmoidal curve shape with clear nucleation and growth stages. Nucleation stage is related to the existing nano-sized crystallites that were not completely amorphized by the ion beam irradiation. Miller *et al*[177] demonstrated that more than 20 vol % crystalline material may still be undetectable in an high-resolution TEM or corresponding SAED at the critical amorphization dose for heavy ion irradiation. These nano-sized crystallites can be nucleus and lower the activation energy, which allows an easier means of nucleation. Solid phase regrowth of amorphous to crystalline phase transformation as a function of irradiation time for HAp-20 nm and HAp-60 nm under different radiation conditions was shown in Figure 4.9. For HAp-20 nm, it is notable an earlier nucleation and a faster a/c phase transformation can be observed for a higher current density of 400 pA/cm^2 comparing with a lower current density of 100 pA/cm^2. The same results were also revealed for HAp-60 nm under different current density. This phenomenal may be related to the amount of the electrons penetrated into the irradiated zone. The nucleation for recrystallization is associated with the ionization processes such as the defects migration and atomic diffusion, as a result of inelastic energy loss of the electron beam. When the energy loss is large enough, nucleation forms as a result of the movement of atoms and atomic rearrangement along the interfaces[168]. The energy loss will increase with the increase of the current density, therefore, the possibility of the interfacial defect rearrangement increase leads to the enhancement of nucleation or the higher nucleation rate. More point defects may be induced under the higher current density, and recrystallization process can be facilitated by a defect-stimulated mechanism similar to ion irradiation.

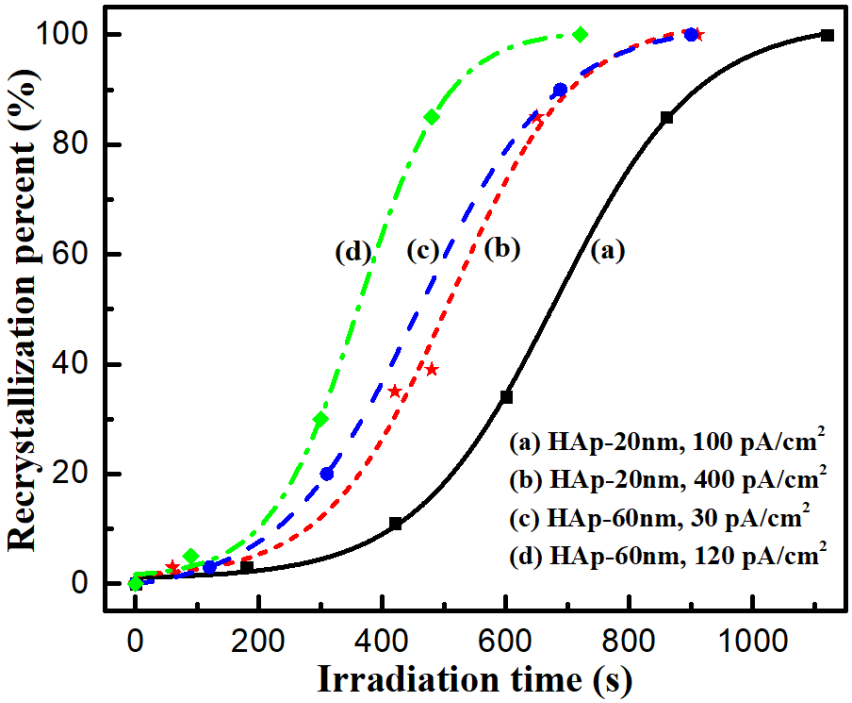

Figure 4.9 Solid phase regrowth of amorphous to crystalline phase transition as a function of irradiation time of e-beam: (a) HAP-20nm under the current density of 100 *p*A/cm^2 (6.25×10^8 e$^-$ cm^{-2} s^{-1}); (b) HAP-20nm under the current density of 400 *p*A/cm^2 (2.5×10^9 e$^-$ cm^{-2} s^{-1}); (c) HAP-60nm under the current density of 30 *p*A/cm^2 (1.875×10^8 e$^-$ cm^{-2} s^{-1}); (d) HAP-60nm under the current density of 120 *p*A/cm^2 (7.5×10^8 e$^-$ cm^{-2} s^{-1})

It should be noted that the electron diffraction pattern obtained after electron beam irradiation (shown Figure 4.10 (b)) exhibited the same features as the unirradiated sample diffraction pattern (Figure 4.10 (c)), indicted that the recrystallization was a solid phase growth. The a/c phase transformation kinetics of the HAp in this dissertation was explained by the Avrami-Erofeev equation[178], Where, f is the crystallization fraction, k is temperature dependent rate constant, and n is JMAK exponent.

$$f = 1 - \exp[-(kt)^n]$$

For HAp-20 nm, JMAK exponent n was determined to be 2.7 and 4 for the current density of 100 *p*A/cm^2 and 400 *p*A/cm^2 respectively, while it was 1.3 and 2.3 for current density of 30 *p*A/cm^2

and 120 pA/cm^2 for HAP-60 nm and 2.5 for current density of 30 pA/cm^2 for HAP-280 nm. According to Senkader *et al*[179], volume nucleation 2D growth and volume nucleation 3D growth were take placed under current density of 100 pA/cm^2 and 400 pA/cm^2 for HAP-20 nm; volume nucleation 1D growth and volume nucleation 2D growth were take placed under current density of 30 pA/cm^2 and 120 pA/cm^2 for HAP-60 nm; and volume nucleation 2D growth was take placed under current density of 30 pA/cm^2 for HAP-280 nm.

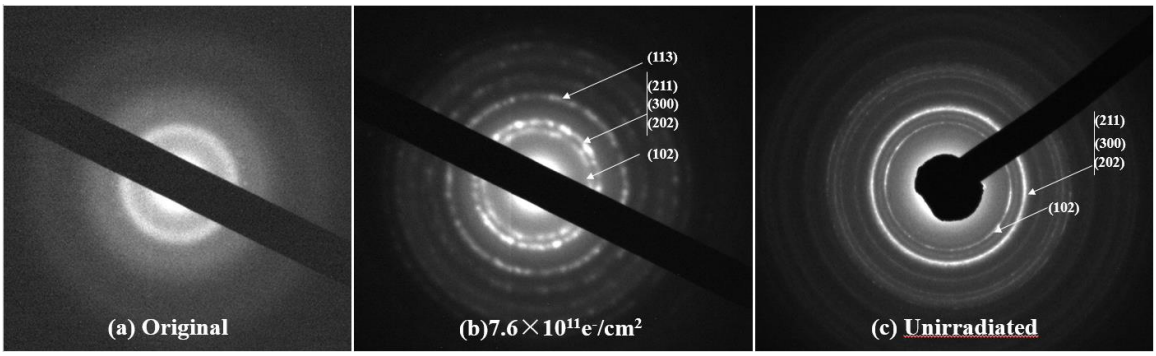

Figure 4.10 Diffraction patterns under different electron fluence: (a) Original diffraction pattern of amorphized sample at room temperature, (b) Diffraction pattern at 1440s (7.6×10^{11} e$^-$/cm^2) under electron beam irradiation at room temperature, (c) Diffraction pattern of unirradiated sample at room temperature

The reciprocal of incubation time as a function of current density for different particle sized amorphous HAp under 200 keV electron irradiation was presented in Figure 4.11. It is notable, with the decrease of current density, more incubation time was required for the electron-irradiation-induced recrystallization. And the incubation time will be close to finite as the current density increases to infinite. This figure will guide us to the future study on electron-irradiation-induced recrystallization behaviors under different radiation conditions and to better understand the irradiation behaviors of HAp under the events of beta-decay.

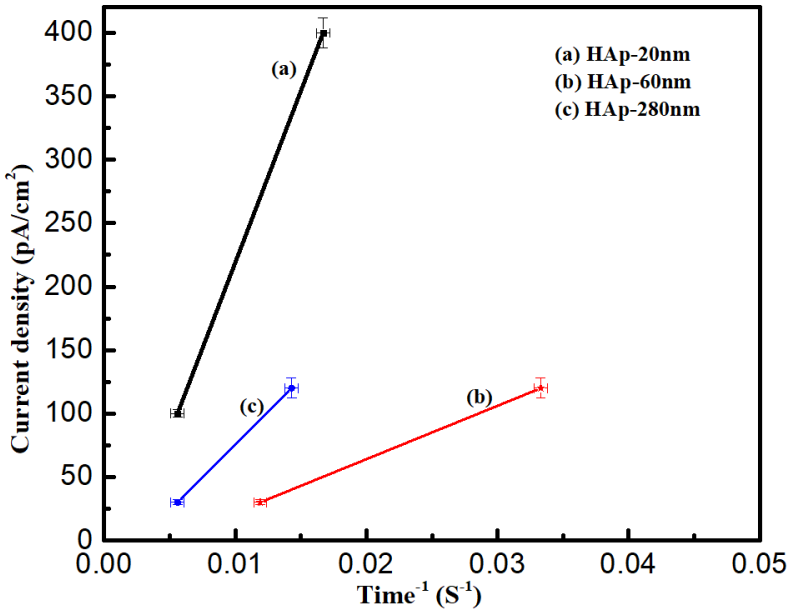

Figure 4.11 The reciprocal of incubation time as a function of current density for different particle sized amorphous hydroxyapatite under 200 keV electron irradiation

4.5 Recrystallization mechanisms

The big different irradiation behaviors, ion-irradiation-induced amorphization and electron-irradiation-induced recrystallization, lie in distinctly different mechanisms. The 1 MeV Kr^{2+} irradiation can create atomic displacements in the materials since it possesses a significant nuclear energy loss and deposits energy to materials mainly via elastic collisions. However, the 200 keV electrons interact with the HAp mainly via inelastic collision and ionization process. These electrons are considered as the sub-threshold electrons since the kinetic energy that the 200 keV electrons transferred to the materials may be too low to induce significant atomic displacements. Possible mechanisms for electron-irradiation-induced recrystallization are ionization processes involving the breaking or rearrangement of unstable bonds[180], atomic displacement effect[174, 181], and beam heating[18, 19, 182]. Although the kinetics of the recrystallization shows similarity to thermally stimulated crystallization, the likelihood of electron beam heating effect as the major driving force is clearly ruled out. The maximum temperature rise due to the beam heating can be

calculated according to the following formula [166, 180, 183],

$$\Delta T = \frac{I}{\pi \kappa e}\left(\frac{\Delta E}{d}\right) ln \frac{b}{r_o}$$

where I is beam current, κ thermal conductivity, b sample radius, r_o beam radius, e electron charge and ΔE is the total energy loss per electron in a sample of the thickness of d, which can be derived from the Bethe-Bloch formula given in the following Equation[184].

$$-\frac{dE}{dx} = \frac{2\pi Z\rho\left(\frac{e^2}{4\pi\epsilon_0}\right)^2}{mv^2}\left\{\ln\left[\frac{E(E+mc^2)^2\beta^2}{2I_e^2 mc^2}\right] + (1-\beta^2) - \left(2-\sqrt{1-\beta^2}-1+\beta^2\right)\ln 2 + \frac{1}{8}\left(1-\sqrt{1-\beta^2}\right)^2\right\},$$

where Z is the atomic number of the target, ρ is its atomic density, m is the electron mass, v is its velocity, E is electron energy, c is the speed of light, $\beta = v/c$, and I_e is the excitation energy for electrons in the target material. Based on the calculation, under 200 keV electrons, with I = 100 pA, κ = 0.36 W/mk[185], b = 1.5 mm, r_o = 100 nm and dE/dx = 0.8 eV/nm, the maximum temperature rise in HAp-20 nm was estimated to be merely 0.7 K and 3 K for current density of 100 pA/cm^2 and 400 pA/cm^2, 0.2 K and 0.9 K for current density of 30 pA/cm^2 and 120 pA/cm^2 for HAp-60 nm. Therefore, temperature increase as a result of electron beam heating is negligible, which is in agreement with other studies [108, 131, 176, 180, 186]. Notably, the electron accelerating voltage used in the irradiation (200 kV) is considered insufficient to generate significant atomic displacements. The threshold energies for displacements E_d in oxide-based ceramics are typically in the range of 20-50 eV [187]. The maximum amount of energy E_{max} that can be transferred from electrons with kinetic energy of E to a target atom is

$$E_{max} = E_0 \frac{2m}{M_A}[(\frac{E}{E_0})^2 + 2\frac{E}{E_0}]$$

where m is the mass of an electron, M_A is the mass of the target, and $E_0 = mc^2$. Accordingly, the E_{max} for the major atoms in HAp are below their threshold energy E_d, so that the atomic displacement assisted growth is also unlikely.

The most tenable mechanism of the sub-threshold electron irradiation induced recrystallization of HAp is the breaking and reforming of the dangling bonds along the amorphous-crystalline (a/c) interface. Compared to bonds in crystalline materials, the weak dangling bonds at the (a/c) interface are relatively easy to break under the ionizing electrons, which is followed by the rearrangement of the nearby atoms in non-equilibrium bonding configurations to form the energetically favored complete bonds, thus driving the recrystallization process. In addition, the nucleation stage is likely heterogeneous as there could be sub-nanometer to nanometer sized residual crystals that were not completely amorphized by the preceding ion beam irradiation. These residual crystals can lower the activation energy and provide seeding sites for nucleation to proceed at an enhanced rate. The other possibility is that the residual crystals after ion irradiation can lower the activation energy and provide seeding sites for nucleation of the recrystallization. In contrast to elastic collision caused amorphization, electron excitation enhanced recrystallization have been reported in many other amorphous materials, such as apatite[132], $ScPO_4$[176], zircon[17] and $CePO_4$[14]. These results showed the recrystallization fluence are on a magnitude around 10^{20} e^-/cm^2 whereas the recrystallization fluences for HAp here are only on a magnitude of 10^{10} e^-/cm^2, suggesting a better defect recovery ability of HAp.

4.6 Synergistic effect of ion and electron beam irradiation

It is worth noting for potential nuclear waste forms, both alpha-decay (producing alpha-

particles and heavier recoils) of actinides and beta-decay (producing beta-particles, low energy recoils, and gama-rays) of fission products are the primary radiation types in a nuclear waste repository environment. The performance of nano-sized HAp as a nuclear waste form is conducted through simultaneous ion and electron beam irradiation in the IVEM-Tandem facility at Argonne National Lab, showing synergistic radiation effects of alpha- and beta-decay. Figure 4.12 showed the set of SAED patterns of 20 nm sized HAp irradiated under simultaneous 1 MeV Kr^{2+} ion beam and 200 keV electron beam irradiation. It is notable the SAED pattern still showed a little intensity of diffraction rings and the dark field image showed sharp contrast at a Kr^{2+} dose of 0.05 dpa, while it is the critical amorphization dose of 20 nm sized HAp irradiated by 1 MeV Kr^{2+} ion beam only at room temperature. The critical amorphization dose of 20 nm sized HAp irradiated under simultaneous 1 MeV Kr^{2+} ion beam and 200 keV electron beam irradiation was 0.15 dpa, as shown in Figure 4.12 (c). Obviously, 20 nm sized HAp had a better radiation tolerance under simultaneous 1 MeV Kr^{2+} ion beam and 200 keV electron beam irradiations. As demonstrated in the previous sections, displacive 1 MeV Kr^{2+} ion beam will cause amorphization process while enhanced defect recovery to promote an inverse amorphous-to-crystalline transformation was observed under 200 keV electron beam irradiation. Radiation behavior of nano-sized HAp was determined by these two processes to compete with each other. Amorphization process was suppressed if ionizing induced electron defect recovery exceeds ion induced displacement under simultaneous ion and electron beam irradiations.

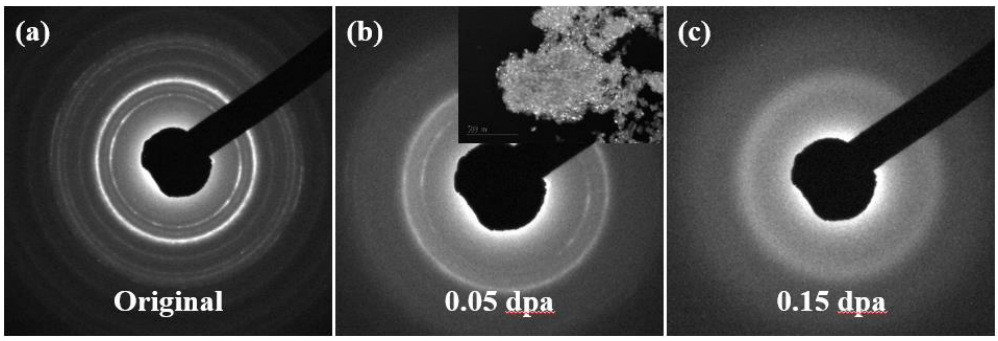

Figure 4.12 Room temperature TEM dark field image and selected area diffraction patterns of (a) the unirradiated (b) 1 MeV Kr^{2+} irradiated at 0.05 dpa and (c) 1 MeV Kr^{2+} irradiated at 0.15 dpa, indicating the ion irradiation-induced amorphization process

4.7 Summary

Electron-irradiation-induced recrystallization behaviors of differently sized HAp varying from 20 nm to 280 nm were studied under 200 keV electron irradiation at different radiation conditions by changing the current density. Firstly, it was revealed the amorphous HAp can recrystallize rapidly upon electron irradiation, *i.e.* a clear amorphous-to-crystalline phase transformation was shown via *in situ* TEM technique. Then, a notable size dependence was observed, which a higher electron fluence was required for the nucleation and completion of the phase transformation for a larger sized sample, which is attributed to the higher density of dangling bonds at the more free-standing open surfaces of the smaller sized sample, greatly enhanced the electronic excitation simulated recrystallization. In addition, the transformation kinetics were also analyzed and different nucleation/growth mechanisms were observed under different radiation conditions. In the final, recrystallization mechanism was attributed to ionization process as a result of breaking and rearrangement of unstable bonds along the amorphous/crystalline interfaces since the maximum temperature rise due to beam heating was negligible and 200 keV electrons were not enough to induce atomic displacement effects.

CHAPTER 5 RADIATION RESPONSE OF HIGH ENTROPY ALLOY UNDER 1 MEV KR^{2+} IONS

5.1 Radiation-induced grain growth of $Al_xCoCrFeNi$ alloys

5.1.1 Introduction

The $Al_xCoCrFeNi$ HEAs have great potential for structural materials due to their excellent mechanical properties, and their microstructure, phase evolution and mechanical response have been previously investigated [188-190]. The irradiation performance, such as precipitation behaviors[64] and phase stability at high doses[191], have also been reported for coarse-grained $Al_xCoCrFeNi$ with varied Al concentrations. However, the radiation behavior of nanostructured $Al_xCoCrFeNi$ HEAs is little understood. As nanostructured material design strategy has become a major focus in advanced nuclear material research, the radiation-induced microstructural development such as grain growth of nanostructures [192-196] is highly relevant to their applications in nuclear reactors. Conventional mechanism of grain growth in nanostructured materials was attributed to a thermally assisted, curvature-driven, grain boundary migration[197, 198]. However, under radiations, rapid increase of grain size was observed in nano-crystalline ceria[199], zirconia[194], CeO_2[195], austenite steel[136], ferrite/martensite steel[200] at a low temperature, ruling out the thermally activated growth process. A study of ceria thin film[199], under the irradiation temperature of 160 K, revealed an oxygen vacancy, defects-driven, grain growth mechanism. A study of nanocrystalline oxides[201] showed a disorder-driven growth process of grain size as a result of the high disorder density near grain boundaries upon ion irradiation. In this section, nanocrystalline $Al_xCoCrFeNi$ HEAs were irradiated with 1 MeV Kr^{2+} ions, and a significant grain growth was observed with strong chemical composition dependence. The microstructures and irradiation behaviors of three different Al concentrations were compared and characterized via XRD, TEM, and EDS. In addition, the mechanisms behind for the grain

growth behaviors of this particular type of alloys were also proposed.

5.1.2 Sample characterization by XRD and TEM

XRD patterns of the as-milled nanocrystalline $Al_xCoCrFeNi$ HEAs were shown in Figure 5.1. For x=0, all the diffraction peaks can be identified in a single phase with the FCC crystal structure, suggesting the pure FCC structure had been formed. As the Al concentration increased to x=1, a new structure identified as BCC crystal structure was observed instead of the FCC crystal structure, however, a mirrored phase with FCC crystal structure corresponding to FCC (200) and (220) can be detected. With continuous increase of the Al content to x=2, a primary BCC and a mirrored FCC crystal structure can be also observed. BCC structure is not close-packed compared to FCC structure, and a phase transformation from the initial FCC to BCC structure can occur in order to reduce the lattice distortion induced by the atomic size mismatch due to the increase of Al concentration[202].

Characterization of nanocrystalline $Al_xCoCrFeNi$ HEAs with different Al concentration varying from x=0 to x=2 was revealed in Figure 5.2, Figure 5.3 and Figure 5.4, respectively by TEM techniques. A representative high-resolution TEM image of Al-0 alloy was shown in Figure 5.2 (a) and the corresponding invert FFT images showing the d-spacing and grain orientation were given in inset. The SAED pattern with a typical poly-crystal diffraction rings defined to be the FCC structure was exhibited in Figure 5.2 (b), and the corresponding BF image was inserted in the left corner. Figure 5.2 (a) displayed the sample with nanostructures in random orientations and the determination of the SAED pattern showed a single FCC structure which is in agreement with the XRD result. A representative high-resolution TEM image of Al-1 alloy was shown in Figure 5.3 (a), and the preferable grain orientation of BCC (110) was in agreement with the highest peak of BCC (110) position in the XRD result. The SAED pattern given in Figure 5.3 (b) showed a

combined BCC+FCC crystal structure, furtherly proved the mirrored peaks corresponding to FCC structure in the XRD result. The same observation can be also found for Al-2 alloy, as shown in Figure 5.4. In different areas of the sample, single BCC crystal structure and combined BCC+FCC crystal structures were revealed via SAED technique, as shown in Figure 5.4 (b) and (d), respectively.

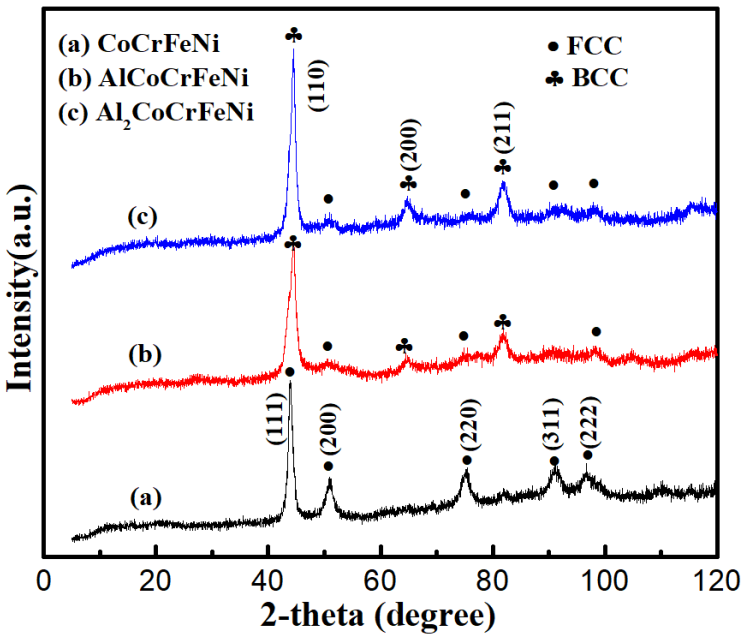

Figure 5.1 XRD analyses of nanocrystalline $Al_xCoCrFeNi$ high entropy alloys with various Al contents (x=0, 1, 2), showing the pure FCC crystal structure for CoCrFeNi alloy, and primary BCC with mirror FCC crystal structure for AlCoCrFeNi and $Al_2CoCrFeNi$ alloys

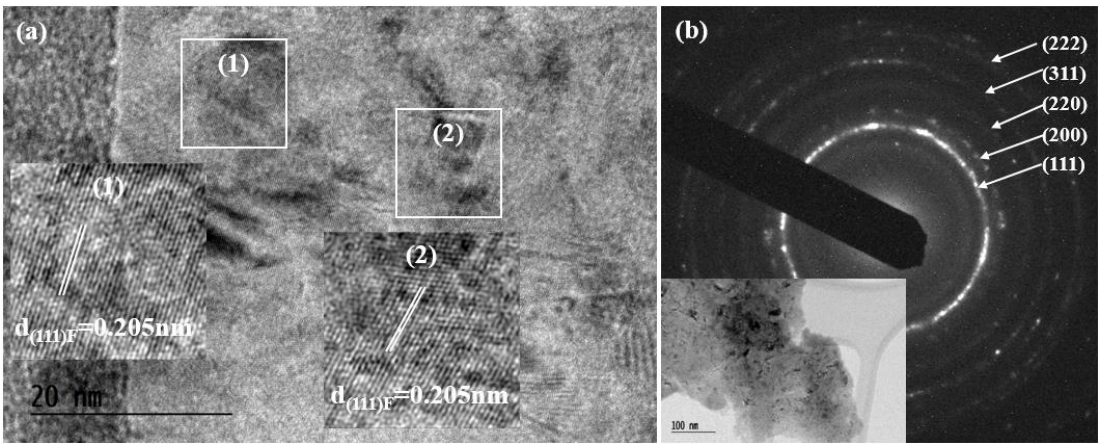

Figure 5.2 Characterization of the CoCrFeNi high entropy alloy: (a) high-resolution TEM image showing nanocrystals in a random orientation, the white square indicates the area from which the inset invert FFT images were obtained; (b) SAED pattern with pure FCC crystal structural, the corresponding bright field image was inserted in the left corner

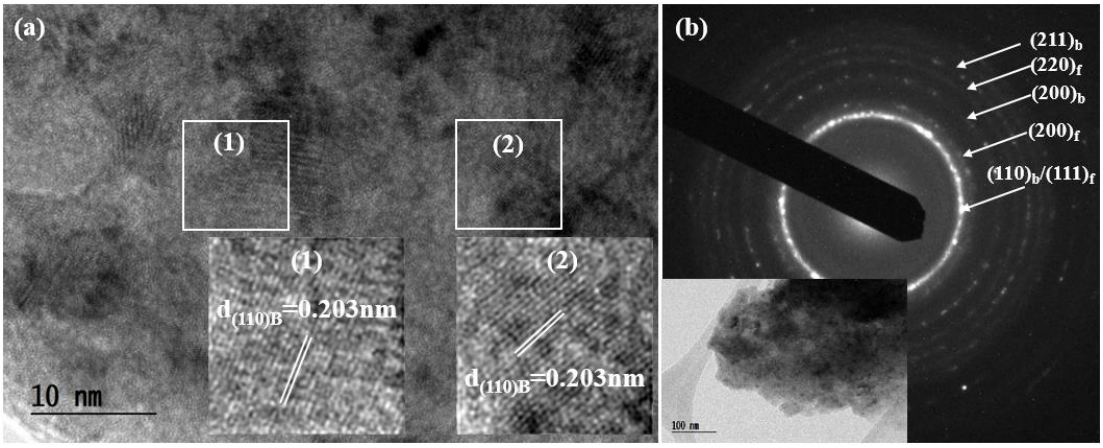

Figure 5.3 Characterization of the AlCoCrFeNi high entropy alloy: (a) high-resolution TEM image showing nanocrystals in a random orientation, the white square indicates the area from which the inset invert FFT images were obtained; (b) SAED pattern with BCC+FCC crystal structural, the bright field image was inserted in the left corner

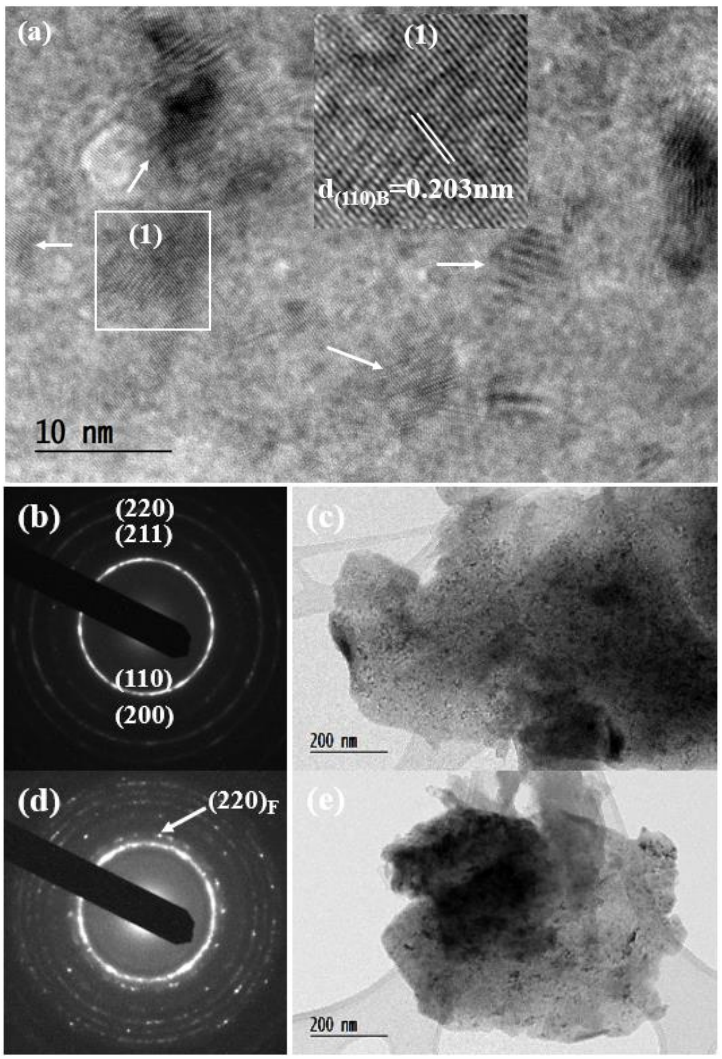

Figure 5.4 Characterization of the $Al_2CoCrFeNi$ high entropy alloy: (a) high-resolution TEM image showing nanocrystals in a random orientation, the white square indicates the area from which the inset invert FFT images were obtained; (b) (c) SAED pattern with pure BCC crystal structural and the corresponding bright field image in area 1 of the sample; (d) (e) SAED pattern with combined BCC+FCC crystal structural and the corresponding bright field image in different area 2 of the sample

5.1.3 Ion-irradiation induced grain growth

At room temperature, *in situ* TEM observation revealed a significant ion-irradiation induced grain growth of nanocrystalline $Al_xCoCrFeNi$ with doses up to 5.625 dpa. A set of TEM BF images and SAED patterns for Al-0 alloy, as shown in Figure 5.5, showed a notable grain size increase. Compared to the SAED pattern with complete rings in Figure 5.5 (e), which indicated a typical

poly-crystalline structure. Figure 5.5 (f) had discreet points, suggesting increased grain size and more aligned orientations. This phenomenon was enhanced by the increase of irradiation dose, indicated by irradiation-induced grain size increase, as shown in Figure 5.5 (g) & (h). Moreover, the growth of nano-grains was clearly demonstrated by comparing contrast of the TEM BF images from Figure 5.5 (a) to Figure 5.5 (d). The *in-situ* TEM observations of grain growth process for Al-1 and Al-2 alloys were shown in Figure 5.6 and Figure 5.7 respectively. By manually measuring the size of more than 35 particles, the average grain size can be obtained, assuming a spherical geometry from TEM BF images acquired from different regions and averaging them according to the Gaussian distribution. The grain size increased with irradiation dose from 13.8±3 nm, 7.4±1 nm, and 11±1 nm before irradiation to 36±8 nm, 25±5 nm and 26.6±3 nm at the irradiation dose of 5.625 dpa for Al-0, Al-1, and Al-2 alloys respectively. In order to determine if there was a phase transformation under ion irradiation, a set of SAED patterns were taken and compared for Al-0 alloy, as shown in Figure 5.5 (e) & (f). The ring index under different irradiation doses was the same and no new diffraction rings were observable due to irradiation, suggesting there was no phase transformation for Al-0 alloy and the phase stability can be observed under intensive ion irradiation. Nanostructured materials showed a high concentration of grain boundaries and interfaces, leading to the different radiation-induced defects behaviors compared with bulk materials due to the limited size in one or more directions. Nano-sized materials may be traversed by energetic ions and the amount of atomic displacement damage in nanostructured materials may be low. Furthermore, a large fraction of GBs and interfaces provide a special environment for defect production, migration, and recombination. Therefore, phase stability can be expected as a result of different irradiation damage mechanisms and self-healing behaviors via unique nano-structural evolution in HEAs.

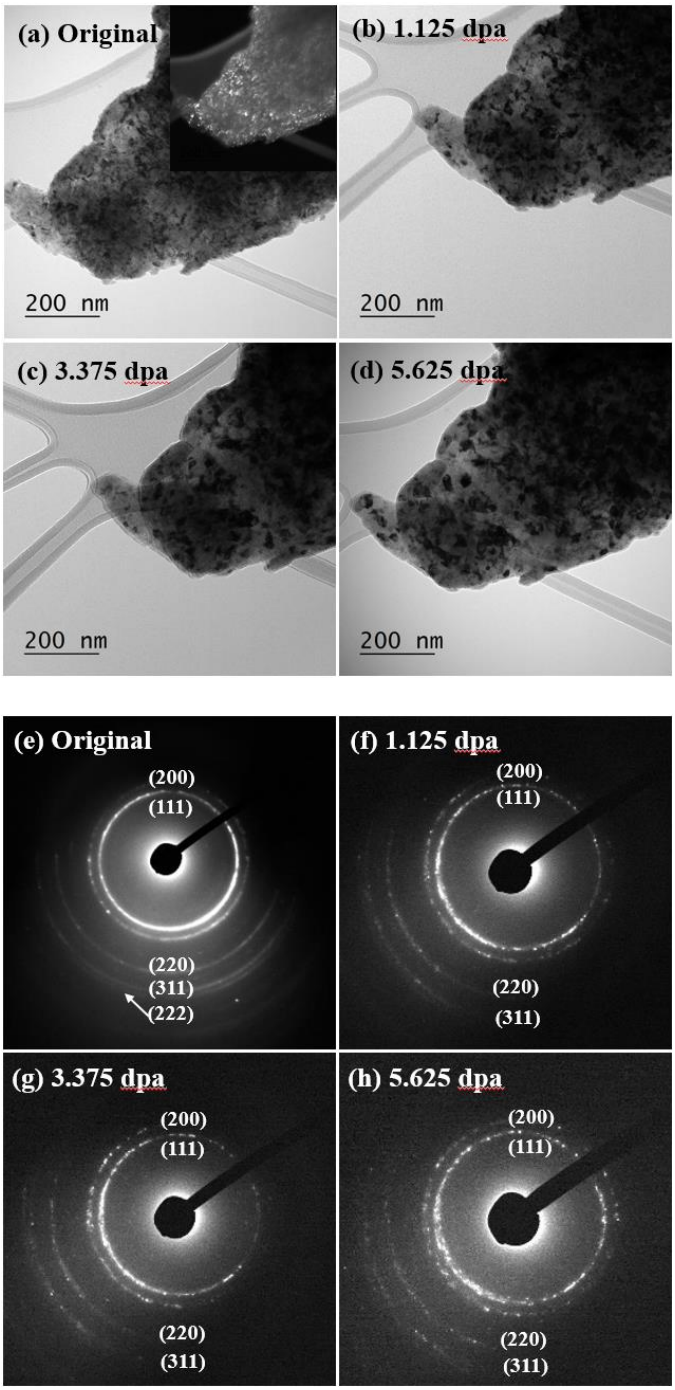

Figure 5.5 Sequence of bright field, dark field TEM images and selected area diffraction patterns taken at different ion doses during irradiation of CoCrFeNi irradiated with 1 MeV Kr^{2+} ions at room temperature, showing ion-irradiation-induced grain growth: (a) (e) Original, (b) (f) 1.125 dpa (5.625×10^{14} ion/cm^2), (c) (g) 3.375 dpa (1.6875×10^{15} ion/cm^2), (d) (h) 5.625 dpa (2.8125×10^{15} ion/cm^2)

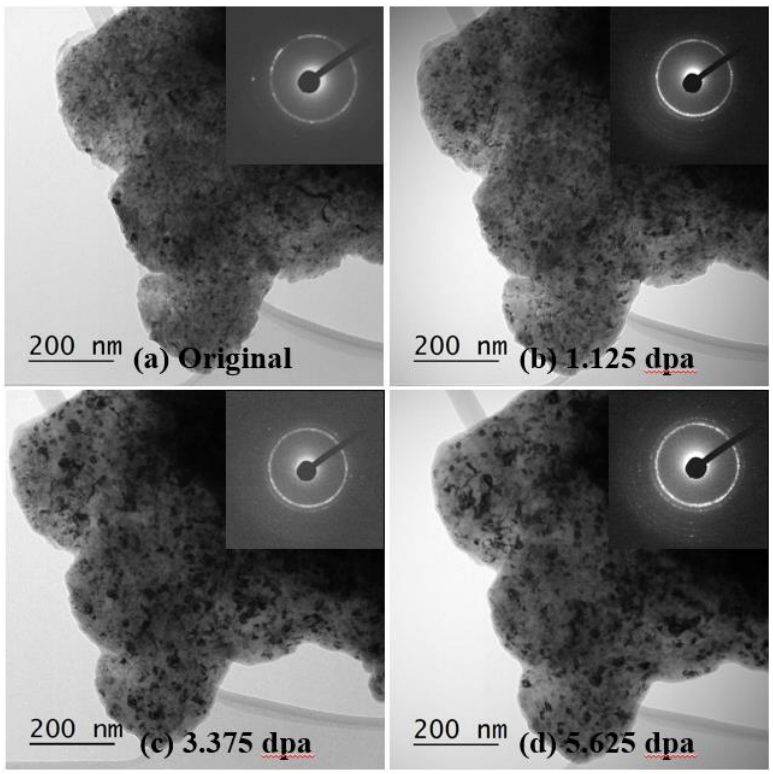

Figure 5.6 Sequence of bright field TEM images and selected area diffraction patterns taken at different ion doses during irradiation of AlCoCrFeNi irradiated with 1 MeV Kr^{2+} ions at room temperature, showing ion-irradiation-induced grain growth: (a) Original, (b) 1.125 dpa (5.625×10^{14} ion/cm^2), (c) 3.375 dpa (1.6875×10^{15} ion/cm^2), (d) 5.625 dpa (2.8125×10^{15} ion/cm^2)

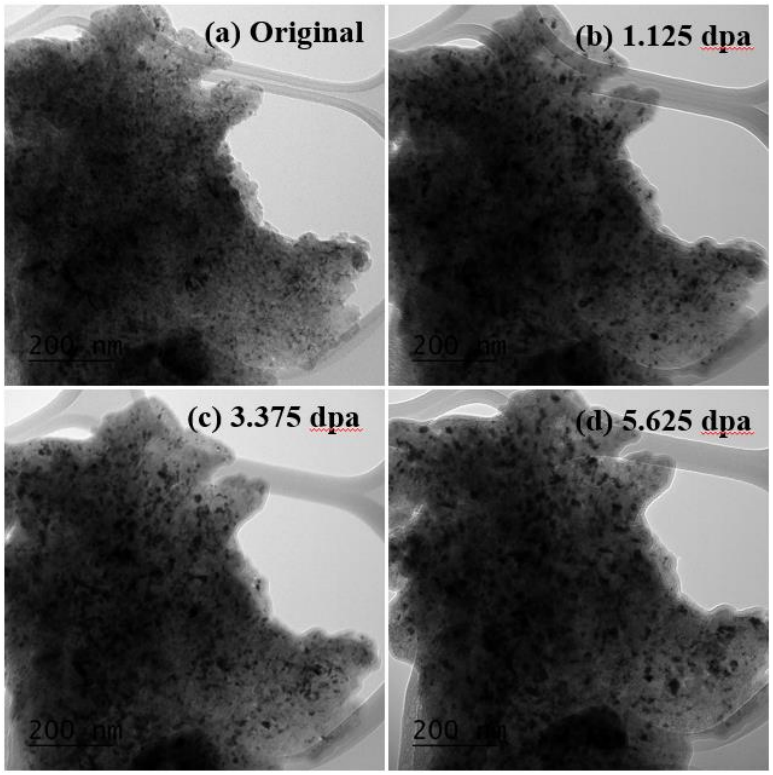

Figure 5.7 Sequence of bright field TEM images taken at different ion doses during irradiation of $Al_2CoCrFeNi$ irradiated with 1 MeV Kr^{2+} ions at room temperature, showing ion-irradiation-induced grain growth: (a) Original, (b) 1.125 dpa (5.625×10^{14} ion/cm^2), (c) 3.375 dpa (1.6875×10^{15} ion/cm^2), (d) 5.625 dpa (2.8125×10^{15} ion/cm^2)

5.1.4 Grain growth kinetics

In the ion-solid interaction, the atomic displacement cascades can create thermal spikes with drastically elevated temperature inside the solid material. Such transient localized melting under ion irradiation can result in the grain growth in irradiation affected regions [203-205]. The driving force was the grain boundary migration and curvature induced by atomic jumps as a result of displacement collision cascade. However, grain growth cannot be induced by the simply isolated displacements but only attributed to the displacement collision cascades that traverse the grain boundary[205]. This was further confirmed by the result that no grain size increase occurred under 1 MeV electron irradiation up to 180 dpa for Zr-based thin film, suggesting only defects created within thermal spikes influence the grain-growth kinetics. Under electron irradiation, there may

be no cascades and thermal spikes, therefore, no increase of grain size can be observed. In order to further demonstrate that grain growth was caused by the thermal spike model in this work, the Al-1 alloy was irradiated with 200 keV electrons at room temperature. Sequences of TEM BF images, SAED patterns as well as high-resolution TEM images taken at different electron doses were shown in Figure 5.8. No growth of grain size can be observed even after a high electron dose by comparing the contrast of the TEM BF images and the diffraction rings in the SAED patterns. The diffraction rings remained to be coherent and no notable discreet points can be observed, and the contrast of the TEM BF images showed no big change after electron irradiation, indicating no grain grow under 200 keV electrons irradiation.

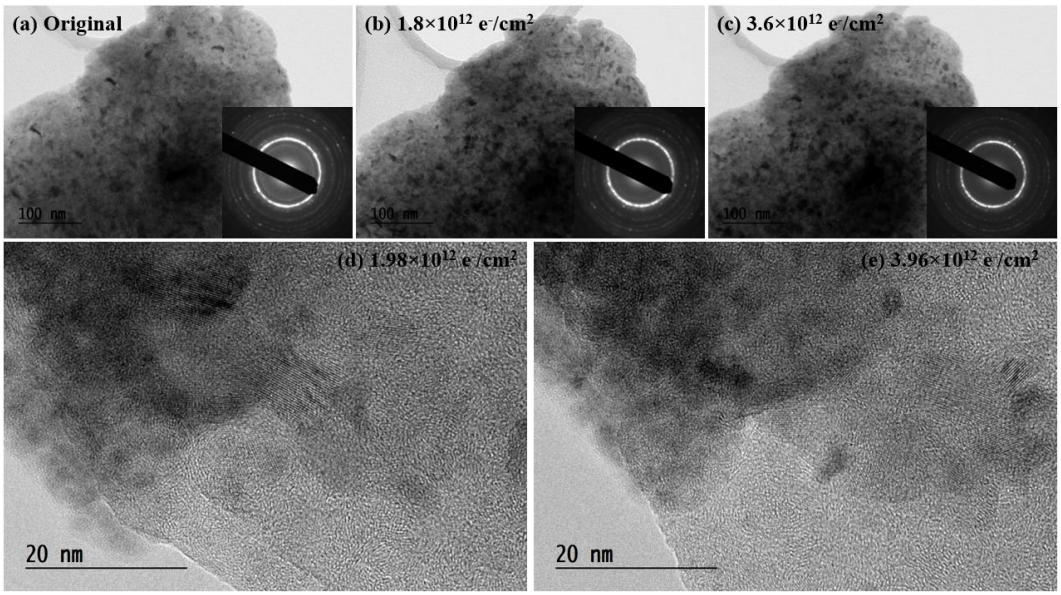

Figure 5.8 Sequences of bright field TEM images, selected area diffraction patterns, and high resolution TEM images taken at different electron doses for AlCoCrFeNi high entropy alloy irradiated with 200 keV electrons at room temperature, showing no electron-irradiation-induced grain growth: (a) Original, (b) 1800s (1.8×10^{12} e^-/cm^2), (c) 3600s (3.6×10^{12} e^-/cm^2), (d) 1800s (1.98×10^{12} e^-/cm^2), (e) 3600s (3.96×10^{12} e^-/cm^2)

Based on this thermal spike model, a power law expression showing the relation between the average grain size and the ion dose was proposed. This expression (listed below) is predicted for

the tendency of grain size increase, where D_0 is the initial average grain size, n is a constant standing for grain growth rate, K is proportional to the GB mobility of the materials and driving force, Φ is ion dose. The grain growth constant n may be the dominating factor affect growth mechanisms, which may be an intrinsic parameter depending on the material system.

$$D^n - D_0^n = K\Phi$$

The fitting parameter n was determined to be 3, 3.5 and 4 for Al-0, Al-1, and Al-2 alloy based on the coefficient of determination R^2 and K is determined to be 9028±663 nm^n/dpa, 13572±1049 nm^n/dpa, and 80458±5794 nm^n/dpa, respectively. Chemical composition dependence on the grain growth has been revealed[205]. A faster growth of grain size was observed in materials with a lower cohesive energy ΔH_{coh} assuming the atomic jump activation energy scales with the cohesive energy[206]. In this dissertation, in order to understand the chemical composition effects on the grain growth kinetics of the $Al_xCoCrFeNi$ HEAs, the intrinsic material properties, cohesive energy, was also analyzed. Cohesive energy of an alloy is determined to be a sum of $a\times\Delta H_{coh}(A)+b\times\Delta H_{coh}(B)$, where a and b are the atomic fraction of the corresponding component A and B, $\Delta H_{coh}(A)$ and $\Delta H_{coh}(B)$ are the cohesive energies for pure metal A and B respectively[207]. The cohesive energies for Al-0, Al-1, and Al-2 alloys were determined to be 4.30 eV, 4.12 eV, and 4.00 eV respectively[208]. It is notable grain growth rate n increased from 3.0 to 4.0 with the increase of the concentration of Al from x=0 to x=2 as a consequence of the reduction of the cohesive energies. In addition, parameter K also showed a significant variation, which Al-2 alloy shows a much higher K value than Al-1 and Al-0 alloys, probably indicating a higher grain boundary mobility and driving force for grain growth process.

It was also noted that, in all grain-growth curves, the grain growth rate decreased as the

irradiation dose increased such that the grain size saturated at relatively high doses, which may be partly attributed to the loss of driving force with the reduction of the curvature of the GBs. Grain boundary migration is a major driving force for ion-irradiation-induced grain size increase for nanostructured materials under ion bombardment[204]. As the grain curvature becomes smaller with increasing grain size, the loss of driving force accounts for the growth of grain size saturation in Figure 5.9. Moreover, as the grain size far exceeds the cascade size, the probability of defect cascades occurring near or at the GBs decreases, resulting in the saturation of grain size after a certain ion dose.

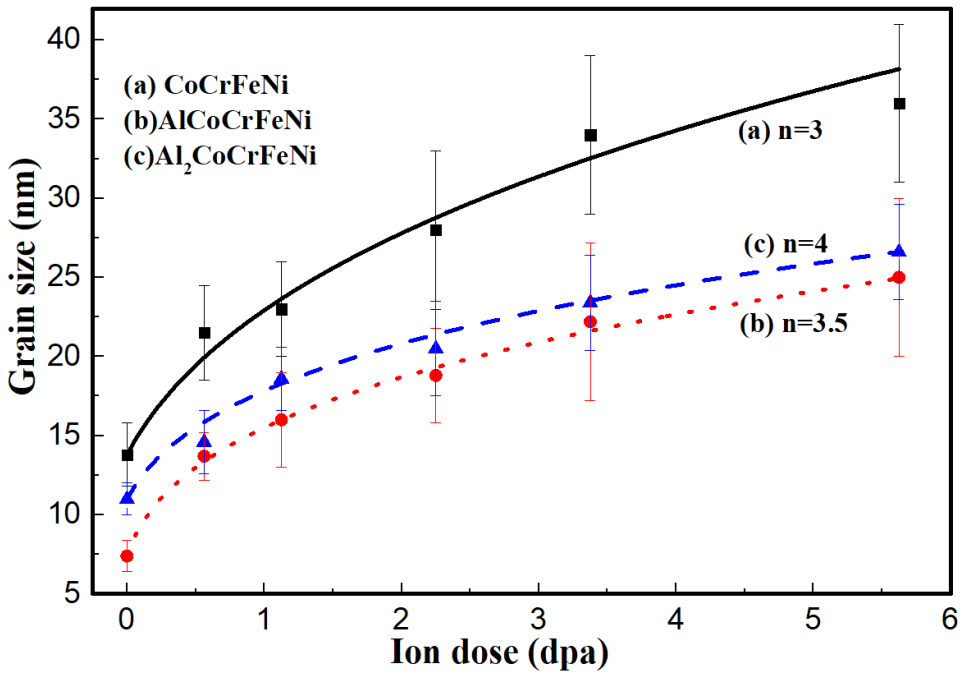

Figure 5.9 Grain growth stimulated by 1 MeV Kr^{2+} ions irradiation at 298 K for $Al_xCoCrFeNi$ high entropy alloys with different Al concentration (x=0, 1, 2). The grain size variation is within the error bars indicated

Radiation-induced grain growth has been revealed in many materials [194, 195, 200, 201]. The conventional mechanisms without irradiations were attributed to the thermally-assisted grain rotation and curvature-driven mechanisms to reduce the grain boundary curvature. However, we observed grain growth in this work at room temperature, and such low-temperature grain growth

does not follow the thermally activated mechanisms. It is worth noting that the grain growth rate decreased rapidly with the increase of the average grain size (as shown in Figure 5.10). For example, the growth decreased significantly from 11 nm/dpa at the grain size of 13.8 nm to 0.8 nm/dpa at the grain size around 35 nm for Al-0 alloy. The decreased grain growth with the increase of grain size was also observed for Al-1 and Al-2 alloys. A disorder-driven grain growth mechanism was proposed by Aidhy *et al*[195], in which the growth of the grains can be primarily attributed to the loss of crystalline order due to atomic disorders at or near GBs upon displacive ion irradiation. The atomic and lattice disordering originating from GBs can induce grain growth in nanocrystalline materials since a large lateral damage volume can be caused by ion irradiation. The lateral damage induces a disordered and non-equilibrium state, which most atoms disfavor. Therefore, under this condition, grain boundaries are likely to migrate and grain size will increase to restore an ordered and equilibrium state of atoms. If the initial grain size is no bigger than the damage volume, which is around the order of 10 nm magnitude according to the reference[201], the grain growth will occur and reach its minimum rate when the grain size is larger than the ion irradiation-induced damage volume[209]. This fast growth mechanism is in a good agreement with the present experimental data of the rapid initial grain size increase, and thus this disorder-driven mechanism is proposed as the dominating growth mechanism for the initial stage of grain growth upon ion irradiation as a result of the very high disorders that spread throughout the grains. In contrast, this disorder-driven mechanism was evaded as the grain grew since a smaller amount of initial disorder cannot induce the movement of grain boundaries for the damaged grains. On the other side, the damaged grains are likely to recover back to its original crystalline order, meaning this disorder-driven mechanism cannot explain the further slower grain growth process. With continuous ion irradiation, a large fraction of point defects (interstitials and vacancies) was induced,

and these defects can be accumulated and absorbed by the GBs, which causes large defects concentration difference near GBs. This defects concentration gradient created a non-equilibrium condition, under which atoms of one grain will be activated to jump across the grain boundary to an available vacant site of the other grain, resulting in the migration of grain boundary and hence the grain growth. Therefore, the further slower grain growth stage was attributed to the defects-simulated mechanism.

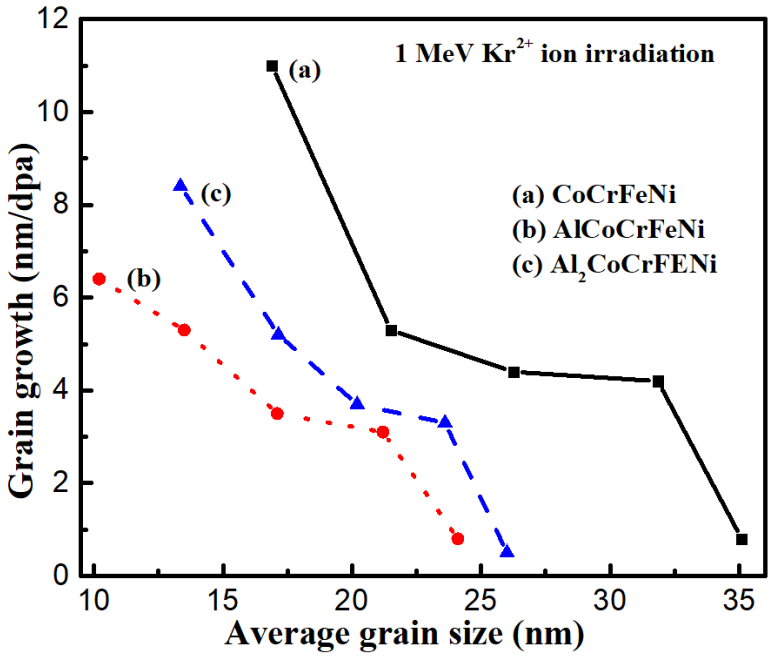

Figure 5.10 Grain growth with the change of average grain size, showing the faster grain growth in the smaller grains as compared to the slower grain size increase in the larger grains

5.1.5 Summary

Nanocrystalline $Al_xCoCrFeNi$ high entropy alloys with different Al content (x=0, 1, 2) were synthesized by high-energy ball milling at room temperature. The crystal structure was determined to be FCC for Al-0 alloy, and BCC+FCC for Al-1 and Al-2 alloys by XRD and TEM techniques. Firstly, a notable grain growth was observed under 1 MeV Kr^{2+} ion irradiation, in which grain size increases with irradiation dose from 13.8±3 nm, 7.4±1 nm, and 11±1 nm before irradiation to 36±8

nm, 25±5 nm, and 26.6±3 nm at an irradiation dose of 5.625 dpa for Al-0, Al-1, and Al-2 alloys, respectively and whose kinetics was elucidated by the thermal spike model. On the other hand, radiation-induced grain growth showed a significant composition dependence that the highest grain growth rate was found in Al-2 alloy as a result of the lowest cohesive energy, which resulted in the lowest activation energy for atomic jump under ion irradiation. Finally, the initial fast grain growth was attributed to the disorder-driven mechanism, which was caused by the loss of the crystalline order as a result of ion-irradiation induced large lateral damage volume. The relatively slow grain growth was attributed to the defect-driven mechanism, in which defects concentration difference near grain boundaries was created by the radiation-induced point defects, creating a non-equilibrium environment via atomic collision cascades that is likely to induce the grain boundary migration, leading to the grain size increase.

5.2 Phase stability of HfNbTaTiVZr alloy

5.2.1 Introduction

A new HEA of six components (Hf, Nb, Ta, Ti, V, Zr) at equimolar ratio was chosen for irradiation studies at different temperatures. Ta, Ti, V were selected because of their radiation resistance properties and Zr due to its ability to collect free gases at low temperature[210]. Nb can enhance corrosion and irradiation-induced swelling resistance[211]. Enhanced microstructure and mechanical properties of HfNbTaTiVZr alloys [212-217] have been previously reported, but its radiation behavior remains largely unexplored. In this section, the phase stability of HfNbTaTiVZr alloy was investigated using 1 MeV Kr^{2+} ion irradiation with the IVEM-tandem facility at 298 K and 423 K.

5.2.2 Sample characterization by XRD and TEM

The X-ray diffraction pattern of the as-cast HfNbTaTiVZr alloy was shown in Figure 5.11. All

the major diffraction peaks were identified as belonging to a BCC crystal structure. The indexes of the crystal planes corresponding to the X-ray diffraction peaks were indicated in Figure 5.12, and the lattice parameter of the BCC phase was determined to be a=0.334 nm. In addition, metallographic examination of the HfNbTaTiVZr alloy specimen revealed a typical dendritic structure with an average grain size of around 20 μm based on the measurements of the SEM images[213]. Moreover, the XRD result was confirmed furtherly via the TEM techniques of high-resolution TEM and SAED. The high-resolution TEM image of HfNbTaTiVZr alloy was shown in Figure 5.12 with SAED pattern inserted in the lower right corner, indicating a single phase poly-crystal BCC structure. This result is also in agreement with the highest diffraction peak in the XRD pattern.

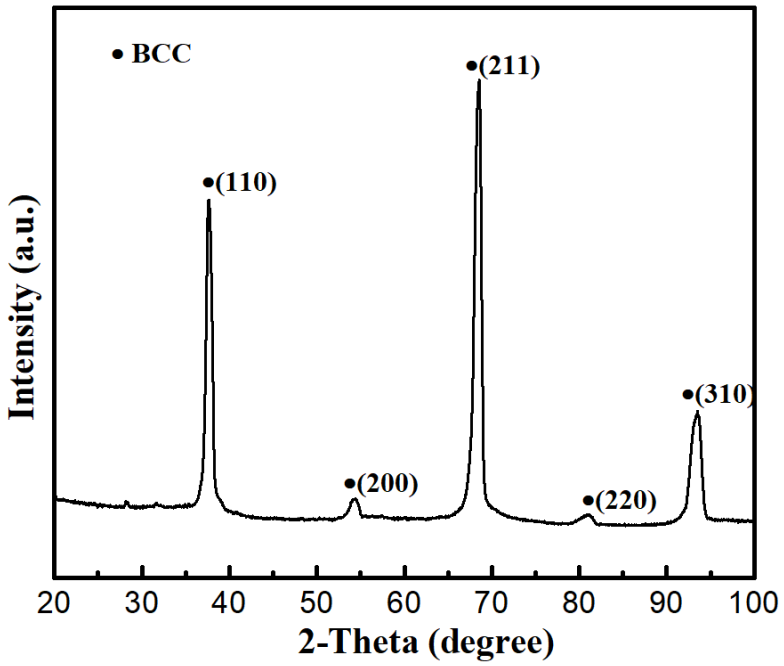

Figure 5.11 X-ray diffraction pattern of the as-cast HfNbTaTiVZr alloy. The indexed peaks belong to a BCC crystal structure with the lattice parameter a=0.334 nm

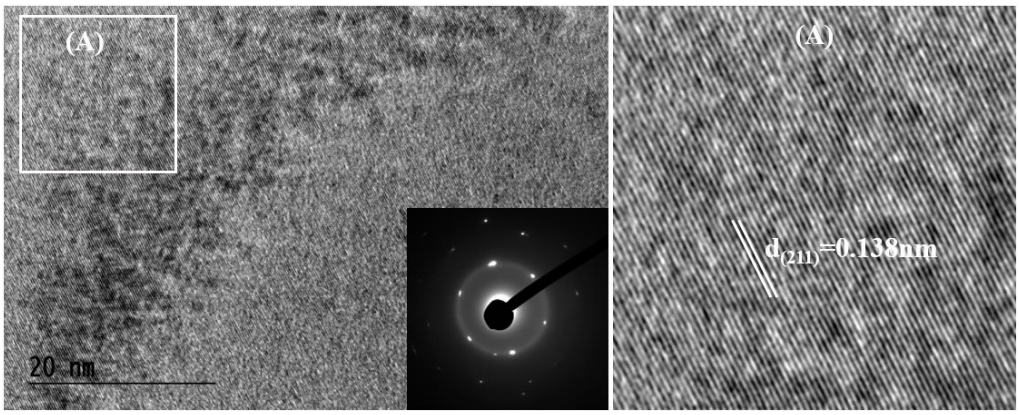

Figure 5.12 High-resolution TEM image of the as-cast HfNbTaTiVZr alloy before ion irradiation and the selected area diffraction pattern was inserted in the right corner.

5.2.3 Radiation-induced phase transformation

Phase stability of HfNbTaTiVZr alloy was investigated with 1 MeV Kr^{2+} ion irradiation under different temperatures (298 K and 423 K). Figure 5.13 shows a set of BF images and SAED patterns with a clear crystal-to-amorphous (c/a) phase transformation by *in situ* TEM observation at 298 K. A poly-crystal structure before ion irradiation was shown in Figure 5.13 (a), indicated by the contrast of the BF image and diffraction spots of the SAED pattern. With the irradiation dose increased to 1 dpa (4×10^{14} ion/cm^2), BF image began to lose its sharp contrast and partial diffraction spots in the SAED pattern was amorphized (as shown in Figure 5.13 (b)), suggesting the specimen cannot maintain the original phase under the intensive ion bombardment. The crystal phase totally transformed to amorphous state at the irradiation dose of 2 dpa (8×10^{14} ion/cm^2), denoted by the completely missing of the sharp contrast in the BF image and the replacement of the diffraction spots by the halos in the SAED pattern completely (as shown in Figure 5.13 (c)). The amorphous state was further confirmed by the inserted DF image showing little contrast in Figure 5.13 (c). The irradiation experiment was also conducted at 423 K up to an irradiation dose of 12.5 dpa. However, no phase transformation was observed at this temperature, as shown in Figure 5.14. The crystalline phase still remained under intensive ion bombardment without halo

formation, although a slight loss of order may have occurred. The amorphization of HfNbTaTiVZr by ion irradiations at 298 K is a relatively rare case for HEA, as there are very few such reports, of which one being the radiation-induced amorphization of $Al_{0.5}$TiZrPdCuNi HEA was also observed under 2 MeV electrons irradiation[218].

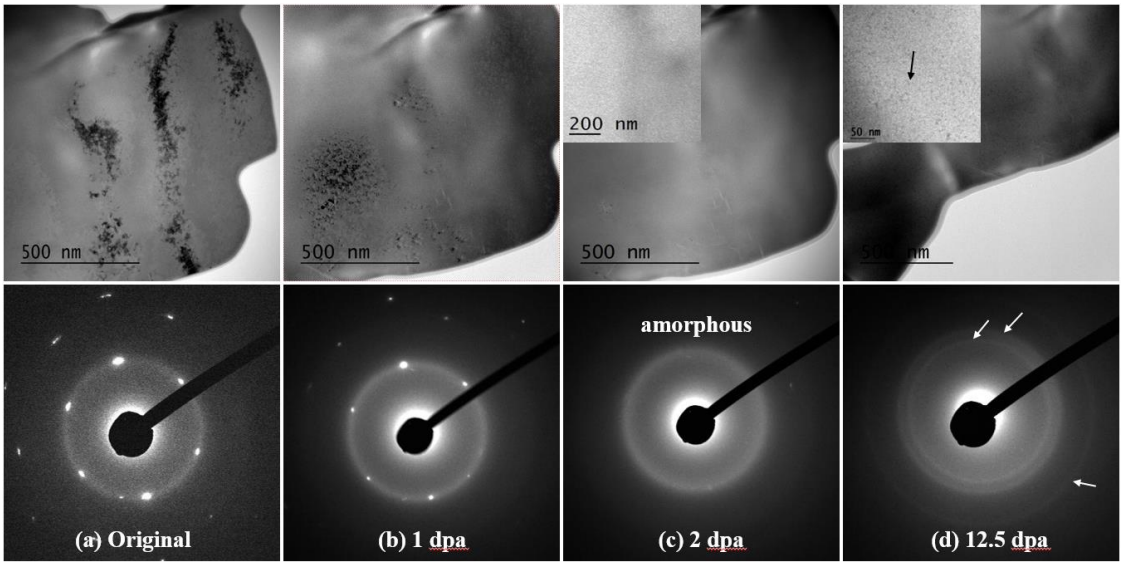

Figure 5.13. Series of TEM bright field images, dark field image (inserted), and selected area diffraction patterns of HfNbTaTiVZr alloy irradiated up to a dose of 12.5 dpa at room temperature, (a) unirradiated, (b) 1 dpa (4×10^{14} ion/cm^2), (c) 2 dpa (8×10^{14} ion/cm^2), (d) 12.5 dpa (5×10^{15} ion/cm^2), showing the crystalline-to-amorphous phase transformation and radiation-induced sputtering under 1 MeV Kr^{2+} ions

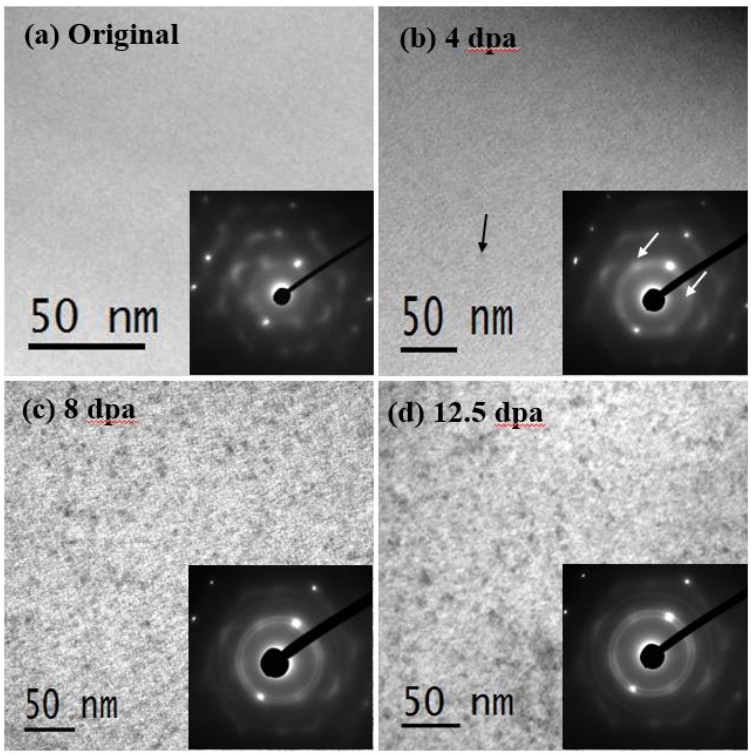

Figure 5.14 Consequence of TEM bright field images and selected area diffraction patterns irradiated at different doses up to 12.5 dpa at 423 K, (a) unirradiated, (b) 4 dpa (1.6×10^{15} ion/cm^2), (c) 8 dpa (3.2×10^{15} ion/cm^2), (d) 12.5 dpa (5×10^{15} ion/cm^2)

Similar to the case of HAp, the amorphization of HfNbTaTiVZr was mainly attributed to the ballistic interaction and subsequent atomic displacements under ion irradiation. With the increasing ion irradiation, radiation-induced point defects accumulate in the material, and eventually lead to the amorphous structure. However, the higher radiation stability at 423 K was again associated with the increased dynamic defect annealing effect, which results in the suppression of radiation damage. Despite the occurrence of amorphization, HfNbTaTiVZr still shows decent radiation tolerance with a critical amorphization dose of 2 dpa. Besides the amorphization process, radiation-induced sputtering was also observed at 298 K and 423 K. At 298 K, sputtering happened at the dose of 7.8 dpa (3.12×10^{15} ion/cm^2). The sputtered materials began to aggregate and grow with the continuous irradiation dose increase to 12.5 dpa (5×10^{15} ion/cm^2), as shown by the dark-contrast nano-features (marked by black arrow) in the BF image

and the Debye rings (marked by white arrows) in the SAED pattern in Figure 5.13 (d). The sputtering was facilitated by elevated temperature, such that at 423 K, sputtering was observed at an earlier stage of 4 dpa (1.6×10^{15} ion/cm^2).

5.2.4 Summary

The phase stability of HfNbTaTiVZr high entropy alloy synthesized by vacuum arc melting method was studied at 298 K and 423 K under 1 MeV Kr^{2+} ion irradiation via *in situ* TEM techniques. A notable temperature dependence on the irradiation behaviors was observed, which showed a clear crystal-to-amorphous phase transformation at 2 dpa for the irradiation temperature of 298 K while the specimen remained crystalline at 12.5 dpa at 423 K. Radiation-induced amorphization at 298 K was mainly attributed to the ballistic interaction and the subsequent accumulation of defects. Significant sputtering was also observed, which was enhanced at the elevated temperature of 423K.

CHAPTER 6 CONCLUSIONS AND FUTURE RESEARCH WORKS

6.1 Conclusions

In order to design advanced ceramic crystalline waste forms and nuclear structural materials, radiation effects in apatite and high entropy alloy structure were studied in this doctoral dissertation. Radiation-induced amorphization and recrystallization of apatite structure under alpha-decay and beta-decay events were simulated by 1 MeV Kr^{2+} ions and 200 keV electrons, respectively. Experimental data showed radiation tolerance of apatite can be tailored by chemical composition, grain size, interfacial structure, and radiation conditions. Various experimental methods, including TEM, XRD, SEM, EDS were used to characterize microstructural evolution, phase transformation and damage mechanisms of apatite under irradiations.

The effect of chemical composition on the radiation response of apatite was investigated using silicate apatite $Mg_2Y_8(SiO_4)_6O_2$ doped with cerium. The radiation tolerance of silicate apatite was found to increase with higher cerium content at the A^I site of the apatite structure. HAp was chosen as a model system to study the effects of grain size, interface and radiation condition. Irradiation data showed that the critical temperature (T_c) for the displacive radiation-induced amorphization of HAp nanoparticles increased with the reduction of the particle size from 280 nm to 20 nm, indicating a reduced radiation tolerance, which can be attributed to the excess surface energy in nanoparticles that lowered the energy gap between amorphous and crystalline states, facilitating the radiation-induced amorphization process. In order to understand the effect of the interface on the radiation tolerance of HAp, free-standing HAp nanoparticles with large surface-area-to-volume ratio and densified nanocrystalline HAp with dense grain boundaries, fabricated by spark plasma sintering, were also investigated. The results indicated that the nanocrystalline sample with dense grain boundaries exhibited higher radiation tolerance as a result of the lower interface energy

compared to the free surfaces of nanoparticles.

The behaviors of apatite under beta-decay events were studied using 200 keV electron irradiation in TEM. *In-situ* TEM observations revealed a rapid recrystallization process of pre-amorphized HAp under 200 keV electrons. Under the same current density, the recrystallization showed a significant size effect such that smaller HAp nanoparticles nucleated and fully recrystallized under lower electron fluences, as a result of the higher density of dangling bonds at the surfaces, which can greatly enhance the electronic excitation simulated recrystallization. Recrystallization mechanism was attributed to the ionization process as a result of breaking and rearrangement of unstable bonds along the amorphous/crystalline interfaces.

The other goal of this dissertation is to develop advanced structural materials for improved nuclear reactor performances. Two types of high entropy alloys, nanocrystalline $Al_xCoCrFeNi$, and micro-sized HfNbTaTiVZr alloys were investigated using 1 MeV Kr^{2+} ions. The study of nanocrystalline $Al_xCoCrFeNi$ alloys showed a notable chemical composition dependence on the ion-irradiation-induced grain growth. A higher growth rate was observed for compositions with higher Al concentration, which can be attributed to the lower cohesive energy which can lower the activation energy of atomic jump under ion irradiation. The initial fast grain growth was explained by the disorder-driven mechanism caused by the loss of the crystalline order as a result of ion-irradiation induced large lateral damage volume. The later stage of slow grain growth was attributed to the defect-driven mechanism, in which grain boundary is likely to migrate under a non-equilibrium environment created by the defects concentration difference near grain boundaries as a result of radiation-induced point defects. HfNbTaTiVZr alloy showed a clear crystal-to-amorphous (c/a) phase transformation at 298 K under ion irradiation. However, no phase transformation was observed at 423 K, indicating enhanced dynamic annealing of radiation-

induced defects.

6.2 Future works

6.2.1 Incorporating iodine into apatite structure

Iodine-129 is a product of nuclear fission which is radiotoxic for human beings. It is a radionuclide with a half-life as long as 15.7×10^6 years, and it cannot be immobilized in the conventional glass waste forms because it has a tendency to transform into volatile I_2 under heat treatment and low incorporation rate in matrix-like glasses and cement. Investigations have been conducted to understand how iodine can immobilize in nuclear waste repositories. Iodine can be incorporated into the apatite structure in the form of iodide like $Pb_{10}(VO_4)_{4.8}(PO_4)_{1.2}I_2$ and $Ca_{15}(PO_4)_9IO$[219] and in the form of iodate like $Ca_{10}(PO_4)_6(OH)_{1.6}(IO_3)_{0.4}$[220] and $Ca_{10}(PO_4)_6(OH)_{1.17}\ (IO_3)_{0.83}$[221]. The apatite structure-type $A^I_4A^{II}_6(BO_4)_6X_2$ has an open frame structure to incorporate large anionic species such as iodine. Its high structural flexibility and excellent chemical durability make it a promising host phase for the immobilization of a wide range of radionuclides, especially the volatile I-129[154]. Before incorporating iodine into the apatite structure, fluorine was used as a surrogate to understand how the HAp structure change after incorporating fluorine. The fluorine was incorporated into the HAp structure by wet precipitation method. XRD data showed two different fluorine-HAp: $Ca_{10}(PO_4)_6(OH)_{0.8}F_{1.2}$ and $Ca10(PO_4)_6(OH)_{0.06}F_{1.94}$ were synthesized, shown in Appendix E.1. However, iodine cannot be incorporated into HAp structure using the same method. From the SEM-EDS result, iodine can be detected, but the XRD patterns showed no difference compared to the pure HAp structure, suggesting iodine was not actually incorporated into the structure but physically soaked on the surface of HAp nanoparticle.

In order to incorporate the iodine into the apatite structure, size of the channel in the apatite

structure has to fit the size of the iodide ion. Wang[222] studied the apatite structure to investigate iodide incorporation into the channel of the structure using Artificial Neural Network and gave the prediction of possible apatite compositions with iodide ion in the structure channel as shown in Figure 6.1. Possible A site cations include Ag^{+}, Sr^{2+}, Pb^{2+}, K^{2+}, Ba^{2+}, Cs^{2+}, possible X site cations include Si^{4+}, Mn^{5+}, As^{5+}, Cr^{5+}, V^{5+}, Re^{7+}, Ge^{4+}, Mo^{5+} and combination of A site= Sr^{2+}, Pb^{2+}, Ba^{2+}, Cs^{2+}, and X site= As^{5+}, Cr^{5+}, V^{5+}, Mo^{5+} may provide suitable channel size for iodide. In the future works, we will continue working on the iodine incorporated apatite projects by increasing channel size through doping chemicals like Ba and V into the A and B sites of apatite structure via wet chemical precipitation method and high energy ball milling. The wet chemical precipitation method will use staring material of $Ca(NO_3)_2$, $(NH_4)_2(HPO_4)$, KI while the high energy ball milling method will use starting material of BaO, V_2O_5, BaI_2. Based on our research process, we found iodine can be incorporated in the apatite structure in the form of $Ba_{10}(VO_4)_6I_2$ via high energy ball milling method.

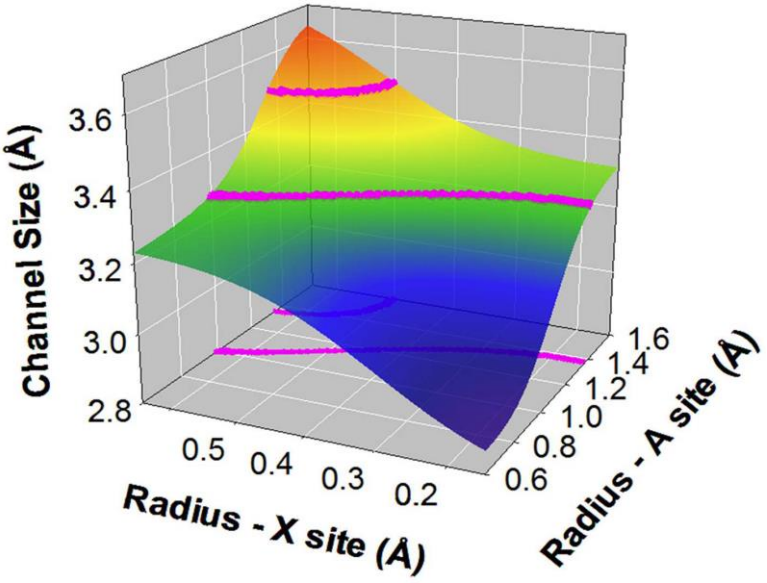

Figure 6.1 Prediction of unknown apatite compositions with iodide ion in the structural channel. The region between pink lines is possible average radii of A and X cations[222]

6.2.2 Future research on HfNbTaTiVZr alloy

In section 5.2, we revealed the phase transformation of HfNbTaTiVZr alloy at 298 K. Other irradiation behaviors like radiation-induced precipitation and segregation, voids formation and swelling *et al* will also affect the performance of this HEA as a structural material. During our irradiation experiments, other interesting observations were also made. In Figure 6.2, we used the overfocus, focus and underfocus bright field images to observe the voids formation process in the HEA. According to our observation, no void formation can be observed at 3.1 dpa and 7.8 dpa at 298 K, and during our irradiation experiments at 423 K, we did not observe vacancy-cluster, dislocations or voids. This indicates a good void swelling resistant ability of this alloy since voids were observed in irradiated single phase materials[44, 223, 224] above 1 dpa, such as void swelling in Fe-Cr-Ni alloys. And some other materials like ferritic-martensitic steels[225], electron-irradiated Zn and Co, neutron irradiated Ti[226], and both neutron and electron irradiated Zr[227] also revealed the formation of voids under irradiation. Designing swelling resistant alloys is of great importance since dimensional instability due to void swelling will affect the performance of structural materials in nuclear reactors, and void swelling has a deleterious impact on the reactor operations and allowable lifetime.

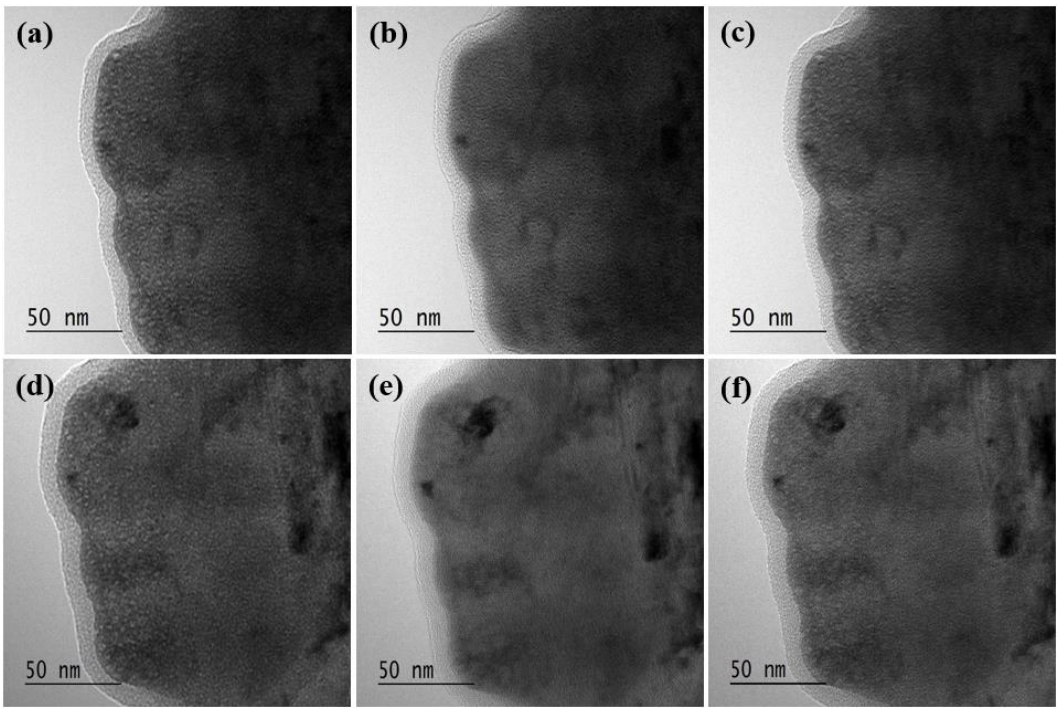

Figure 6.2 Bright field TEM images of HfNbTaTiVZr alloy irradiated at different doses at 298 K: (a) under focus, (b) focus, (c) over focus, showing no voids were observed irradiated at a dose of 3.1 dpa; (d) under focus, (e) focus, (f) over focus, showing no voids were observed irradiated at a dose of 7.8 dpa

In addition to the observation of void formation, investigate on radiation-induced segregation was also made. Figure 6.3 showed the chemical composition concentration profiles for different elements across the interface boundary in HfNbTaTiVZr alloy upon irradiation dose of 12.5 dpa at 298 K. The chemical composition analysis along the interface boundary were performed via TEM-EDS technique at a distance gap of 150 nm, and the EDS analysis was listed in Appendix. F.1-Appendix. F.7. The element concentration analysis as a function of distance along the interface boundary revealed a depletion of Ti and V elements along with an enrichment of Hf and Ta to a comparable level of 2-6 at% near IB relative to the composition of irradiated matrix. Radiation-induced segregation at sinks such as grain boundaries, dislocations as well as precipitate/matrix interfaces may cause extensive local chemical composition change, which may lead to precipitation and phase instability[228]. Radiation-induced segregation was usually attributed to

nonzero chemical fluxes resulting from the build-up of permanent nonzero net fluxes of point defects as a result of the continuous production of point defects combined with the preferential recombination or elimination at the localized extended regions[229, 230].

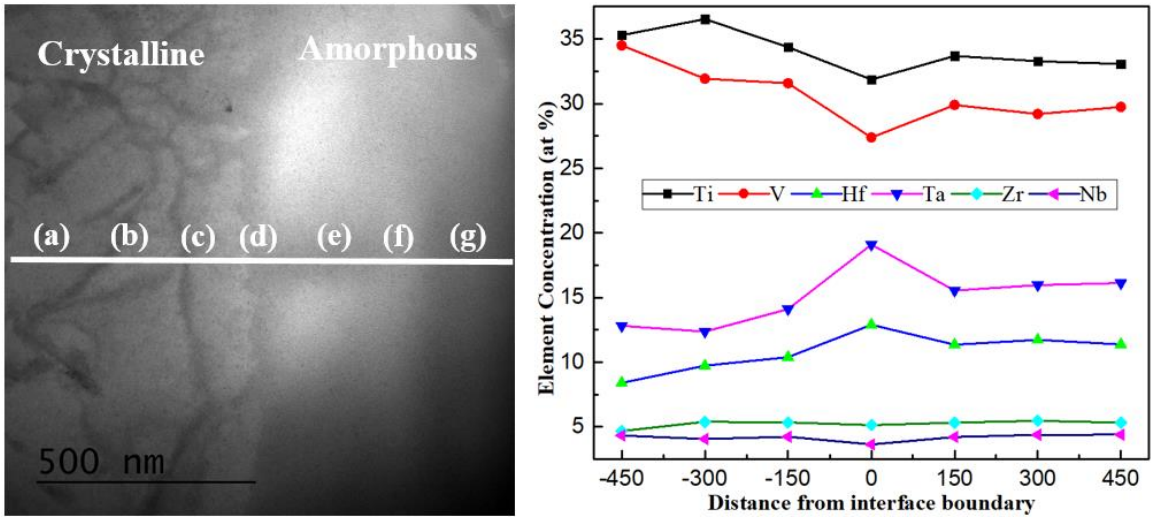

Figure 6.3 (Left) TEM BF image shows interface boundary of HfNbTaTiVZr alloy at 12.5 dpa at 298 K; (Right) Radiation-induced segregation: change in concentrations at the interface boundary of the individual elements with respect to the distance from interface boundary

It is well known advanced nuclear energy systems are highly dependent on the enhanced performance of structural materials to retain their functionality under extreme radiation conditions. Harsher requirements were needed with the improvement of nuclear technology. High entropy alloys have shown many promising properties for the structural application, especially at high temperatures. For this particular alloy, the first future work will be to study the mechanism for enhanced void swelling ability and radiation-induced segregation systematically. Some other future research should also be conducted, including irradiated this alloy to higher doses to confirm and extend the current observation. Some other compositions with four or five main elements, should also be synthesized and irradiated and compared with the HfNbTaTiVZr alloy to study the composition complexity effect on the radiation response.

REFERENCES

[1] N.A. Chapman, I.G. Mc Kinley, The geological disposal of nuclear waste, (1987).

[2] P.A. Baisden, G.R. Choppin, Nuclear waste management and the nuclear fuel cycle, Radiochemistry and Nuclear Chemistry (2007) 1-63.

[3] I. Donald, B. Metcalfe, R.J. Taylor, The immobilization of high level radioactive wastes using ceramics and glasses, Journal of Materials Science 32(22) (1997) 5851-5887.

[4] W. Walker, The back-end of the nuclear fuel-cycle, History and Technology, an International Journal 9(1-4) (1992) 189-201.

[5] E.R. Vance, M. Carter, G. Lumpkin, R. Day, B. Begg, Solid Solubilities of Pu, U, Gd and Hf in Candidate Ceramic Nuclear Wasteforms, Australian Nuclear Science and Technology Organization, Menai, NSW 2234, Australia (US), 2001.

[6] E.E. Jay, Atomistic scale modelling of phosphate mineral phases for nuclear waste form development, Imperial College London, 2012.

[7] N.R. Council, Disposition of High-Level Waste and Spent Nuclear Fuel: The Continuing Societal and Technical Challenges, National Academies Press, 2001.

[8] C. Lopez, X. Deschanels, J. Bart, J. Boubals, C. Den Auwer, E. Simoni, Solubility of actinide surrogates in nuclear glasses, Journal of Nuclear Materials 312(1) (2003) 76-80.

[9] I.W. Donald, Waste immobilization in glass and ceramic based hosts: radioactive, toxic and hazardous wastes, John Wiley & Sons, 2010.

[10] W. Lutze, R.C. Ewing, Radioactive waste forms for the future, (1988).

[11] H. Rawson, Properties and applications of glass, North-Holland, 1980.

[12] R.C. Ewing, The design and evaluation of nuclear-waste forms: clues from mineralogy, The Canadian Mineralogist 39(3) (2001) 697-715.

[13] N.T. Rempe, Permanent underground repositories for radioactive waste, Progress in Nuclear Energy 49(5) (2007) 365-374.

[14] F. Lu, Y. Shen, X. Sun, Z. Dong, R.C. Ewing, J. Lian, Size dependence of radiation-induced amorphization and recrystallization of synthetic nanostructured $CePO_4$ monazite, Acta Materialia 61(8) (2013) 2984-2992.

[15] J. Wen, C. Sun, P. Dholabhai, Y. Xia, M. Tang, D. Chen, D. Yang, Y. Li, B. Uberuaga, Y. Wang, Temperature dependence of the radiation tolerance of nanocrystalline pyrochlores $A_2Ti_2O_7$ (A= Gd, Ho and Lu), Acta Materialia 110 (2016) 175-184.

[16] J. Lian, J. Chen, L. Wang, R.C. Ewing, J.M. Farmer, L.A. Boatner, K. Helean, Radiation-induced amorphization of rare-earth titanate pyrochlores, Physical Review B 68(13) (2003) 134107.

[17] J. Zhang, J. Lian, A.F. Fuentes, F. Zhang, M. Lang, F. Lu, R.C. Ewing, Enhanced radiation resistance of nanocrystalline pyrochlore $Gd_2(Ti_{0.65}Zr_{0.35})_2O_7$, Applied Physics Letters 94(24) (2009) 243110.

[18] R.C. Ewing, T.J. Headley, Alpha-recoil damage in natural zirconolite ($CaZrTi_2O_7$), Journal of Nuclear Materials 119(1) (1983) 102-109.

[19] W. Weber, J. Wald, H. Matzke, Effects of self-radiation damage in Cm-doped $Gd_2Ti_2O_7$ and $CaZrTi_2O_7$, Journal of Nuclear Materials 138(2-3) (1986) 196-209.

[20] W.J. Weber, R.C. Ewing, L.M. Wang, The radiation-induced crystalline-to-amorphous transition in zircon, Journal of Materials Research 9(03) (1994) 688-698.

[21] R.C. Ewing, A. Meldrum, L. Wang, W.J. Weber, L.R. Corrales, Radiation effects in zircon, Reviews in Mineralogy and Geochemistry 53(1) (2003) 387-425.

[22] C.E.H. Cao, Wet-chemical synthesis of apatite-based ceramic waste forms for the immobilization of radioactive iodine (i-129), Rutgers University-Graduate School-New Brunswick, 2017.

[23] S.A. Redfern, S.E. Smith, E.R. Maddrell, High-temperature breakdown of synthetic iodovanadinite, $Pb_5(VO_4)_3I$: an apatite-related compound for iodine radioisotope immobilisation? Mineralogical Magazine, 76(4) (2012) 997–1003.

[24] W. Suchanek, M. Yoshimura, Processing and properties of hydroxyapatite-based biomaterials for use as hard tissue replacement implants, Journal of Materials Research 13(01) (1998) 94-117.

[25] L. Wang, J. Chen, R. Ewing, Radiation and thermal effects on porous and layer structured materials as getters of radionuclides, Current Opinion in Solid State and Materials Science 8(6) (2004) 405-418.

[26] R. Suganthi, S.P. Parthiban, K. Elayaraja, E. Girija, P. Kulariya, Y. Katharria, F. Singh, K. Asokan, D. Kanjilal, S.N. Kalkura, Investigations on the in vitro bioactivity of swift heavy oxygen ion irradiated hydroxyapatite, Journal of Materials Science: Materials in Medicine 20(1) (2009) 271-275.

[27] S.J. Zinkle, J.T. Busby, Structural materials for fission & fusion energy, Materials Today 12(11) (2009) 12-19.

[28] K. Jin, H. Bei, Y. Zhang, Ion irradiation induced defect evolution in Ni and Ni-based FCC equiatomic binary alloys, Journal of Nuclear Materials 471 (2016) 193-199.

[29] L. Malerba, Molecular dynamics simulation of displacement cascades in α-Fe: A critical review, Journal of nuclear materials 351(1) (2006) 28-38.

[30] A. Calder, D.J. Bacon, A. Barashev, Y.N. Osetsky, Effect of mass of the primary knock-on atom on displacement cascade debris in α-iron, Philosophical Magazine Letters 88(1) (2008) 43-53.

[31] J.H. Shim, H.J. Lee, B.D. Wirth, Molecular dynamics simulation of primary irradiation defect formation in Fe-10% Cr alloy, Journal of Nuclear Materials 351(1) (2006) 56-64.

[32] M. Griffiths, A review of microstructure evolution in zirconium alloys during irradiation, Journal of Nuclear Materials 159 (1988) 190-218.

[33] A.V. Nikulina, V. Markelov, M. Peregud, Y.K. Bibilashvili, V. Kotrekhov, A. Lositsky, N. Kuzmenko, Y.P. Shevnin, V. Shamardin, G. Kobylyansky, Zirconium alloy E635 as a material for fuel rod cladding and other components of VVER and RBMK cores, Zirconium in the Nuclear Industry: Eleventh International Symposium, ASTM International, 1996.

[34] F. Garner, Radiation damage in austenitic steels, Comprehensive Nuclear Materials 4 (2012) 33-95.

[35] F. Garner, M. Toloczko, B. Sencer, Comparison of swelling and irradiation creep behavior of fcc-austenitic and bcc-ferritic/martensitic alloys at high neutron exposure, Journal of Nuclear Materials 276(1) (2000) 123-142.

[36] M. Desormeaux, B. Rouxel, A. Motta, M. Kirk, C. Bisor, Y. de Carlan, A. Legris, Development of radiation damage during in-situ Kr++ irradiation of Fe-Ni-Cr model austenitic steels, Journal of Nuclear Materials 475 (2016) 156-167.

[37] K. Vörtler, C. Björkas, D. Terentyev, L. Malerba, K. Nordlund, The effect of Cr concentration on radiation damage in Fe-Cr alloys, Journal of Nuclear Materials 382(1) (2008) 24-30.

[38] R. Klueh, Reduced-activation bainitic and martensitic steels for nuclear fusion applications, Current Opinion in Solid State and Materials Science 8(3-4) (2004) 239-250.

[39] R.L. Klueh, N. Hashimoto, P.J. Maziasz, New nano-particle-strengthened ferritic/martensitic steels by conventional thermo-mechanical treatment, Journal of Nuclear Materials 367 (2007) 48-53.

[40] D.T. Hoelzer, J. Bentley, M.A. Sokolov, M.K. Miller, G.R. Odette, M. Alinger, Influence of particle dispersions on the high-temperature strength of ferritic alloys, Journal of Nuclear Materials 367 (2007) 166-172.

[41] A. Kimura, T. Sawai, K. Shiba, A. Hishinuma, S. Jitsukawa, S. Ukai, A. Kohyama, Recent progress in reduced activation ferritic steels R&D in Japan, Nuclear Fusion 43(10) (2003) 1246.

[42] G. Kalinin, V. Barabash, A. Cardella, J. Dietz, K. Ioki, R. Matera, R. Santoro, R. Tivey, Assessment and selection of materials for ITER in-vessel components, Journal of Nuclear Materials 283 (2000) 10-19.

[43] N. Baluc, K. Abe, J. Boutard, V. Chernov, E. Diegele, S. Jitsukawa, A. Kimura, R. Klueh, A. Kohyama, R.J. Kurtz, Status of R&D activities on materials for fusion power reactors, Nuclear Fusion 47(10) (2007) S696.

[44] B. Singh, S. Zinkle, Defect accumulation in pure fcc metals in the transient regime: a review, Journal of Nuclear Materials 206(2-3) (1993) 212-229.

[45] W.E. King, S.J. Tumey, J. Rest, G.H. Gilmer, The effect of lattice and grain boundary diffusion on the redistribution of Xe in metallic nuclear fuels: Implications for the use of ion implantation to study fission-gas-bubble nucleation mechanisms, Journal of Nuclear Materials 415(1) (2011) 38-54.

[46] C.L. Fu, M. Krčmar, G.S. Painter, X.Q. Chen, Vacancy mechanism of high oxygen solubility and nucleation of stable oxygen-enriched clusters in Fe, Physical Review Letters 99(22) (2007) 225502.

[47] B. Cantor, I. Chang, P. Knight, A. Vincent, Microstructural development in equiatomic multicomponent alloys, Materials Science and Engineering: A 375 (2004) 213-218.

[48] C.Y. Hsu, J.W. Yeh, S.K. Chen, T.T. Shun, Wear resistance and high-temperature compression strength of Fcc $CuCoNiCrAl_{0.5}Fe$ alloy with boron addition, Metallurgical and Materials Transactions A 35(5) (2004) 1465-1469.

[49] F. Otto, A. Dlouhý, C. Somsen, H. Bei, G. Eggeler, E.P. George, The influences of temperature and microstructure on the tensile properties of a CoCrFeMnNi high-entropy alloy, Acta Materialia 61(15) (2013) 5743-5755.

[50] A. Gali, E.P. George, Tensile properties of high-and medium-entropy alloys, Intermetallics 39 (2013) 74-78.

[51] B. Gludovatz, A. Hohenwarter, D. Catoor, E.H. Chang, E.P. George, R.O. Ritchie, A fracture-resistant high-entropy alloy for cryogenic applications, Science 345(6201) (2014) 1153-1158.

[52] C.J. Tong, M.R. Chen, J.W. Yeh, S.J. Lin, S.K. Chen, T.T. Shun, S.Y. Chang, Mechanical performance of the $Al_xCoCrCuFeNi$ high-entropy alloy system with multiprincipal elements, Metallurgical and Materials Transactions A 36(5) (2005) 1263-1271.

[53] J.M. Wu, S.J. Lin, J.W. Yeh, S.K. Chen, Y.S. Huang, H.C. Chen, Adhesive wear behavior of $Al_xCoCrCuFeNi$ high-entropy alloys as a function of aluminum content, Wear 261(5) (2006) 513-519.

[54] Y. Chen, T. Duval, U. Hung, J. Yeh, H. Shih, Microstructure and electrochemical properties of high entropy alloys-a comparison with type-304 stainless steel, Corrosion Science 47(9) (2005) 2257-2279.

[55] Y.J. Hsu, W.C. Chiang, J.K. Wu, Corrosion behavior of $FeCoNiCrCu_x$ high-entropy alloys in 3.5% sodium chloride solution, Materials Chemistry and Physics 92(1) (2005) 112-117.

[56] A.L. Greer, Confusion by design, Nature 366(6453) (1993) 303-304.

[57] W. Guo, W. Dmowski, J.Y. Noh, P. Rack, P.K. Liaw, T. Egami, Local atomic structure of a high-entropy alloy: an x-ray and neutron scattering study, Metallurgical and Materials Transactions A 44(5) (2013) 1994-1997.

[58] L.J. Santodonato, Y. Zhang, M. Feygenson, C.M. Parish, M.C. Gao, R.J. Weber, J.C. Neuefeind, Z. Tang, P.K. Liaw, Deviation from high-entropy configurations in the atomic distributions of a multi-principal-element alloy, Nature Communications 6 (2015).

[59] Y. Zhang, T.T. Zuo, Z. Tang, M.C. Gao, K.A. Dahmen, P.K. Liaw, Z.P. Lu, Microstructures and properties of high-entropy alloys, Progress in Materials Science 61 (2014) 1-93.

[60] M.C. Gao, J.W. Yeh, P.K. Liaw, Y. Zhang, High-Entropy Alloys, Springer 2016.

[61] T. Nagase, S. Anada, P.D. Rack, J.H. Noh, H. Yasuda, H. Mori, T. Egami, Electron-irradiation-induced structural change in Zr-Hf-Nb alloy, Intermetallics 26 (2012) 122-130.

[62] T. Nagase, S. Anada, P.D. Rack, J.H. Noh, H. Yasuda, H. Mori, T. Egami, MeV electron-irradiation-induced structural change in the bcc phase of Zr-Hf-Nb alloy with an approximately equiatomic ratio, Intermetallics 38 (2013) 70-79.

[63] T. Nagase, P.D. Rack, J.H. Noh, T. Egami, In-situ TEM observation of structural changes in nano-crystalline CoCrCuFeNi multicomponent high-entropy alloy (HEA) under fast electron irradiation by high voltage electron microscopy (HVEM), Intermetallics 59 (2015) 32-42.

[64] T. Yang, S. Xia, S. Liu, C. Wang, S. Liu, Y. Fang, Y. Zhang, J. Xue, S. Yan, Y. Wang, Precipitation behavior of $Al_xCoCrFeNi$ high entropy alloys under ion irradiation, Scientific Reports 6 (2016).

[65] N.K. Kumar, C. Li, K. Leonard, H. Bei, S. Zinkle, Microstructural stability and mechanical behavior of FeNiMnCr high entropy alloy under ion irradiation, Acta Materialia 113 (2016) 230-244.

[66] S. Xia, X. Yang, T. Yang, S. Liu, Y. Zhang, Irradiation resistance in $Al_xCoCrFeNi$ high entropy alloys, Jom 67(10) (2015) 2340-2344.

[67] I. Jencic, Radiation damage in nuclear waste materials, (2000).

[68] O. Ménard, T. Advocat, J. Ambrosi, A. Michard, Behaviour of actinides (Th, U, Np and Pu) and rare earths (La, Ce and Nd) during aqueous leaching of a nuclear glass under geological disposal conditions, Applied Geochemistry 13(1) (1998) 105-126.

[69] E. Pichot, N. Dacheux, V. Brandel, M. Genet, Investigation of $137Cs^{+}$, $85Sr^{2+}$ and $241Am^{3+}$ ion exchange on thorium phosphate hydrogenphosphate and their immobilization in the thorium phosphate diphosphate, New Journal of Chemistry 24(12) (2000) 1017-1023.

[70] J. Lian, L. Wang, J. Chen, R. Ewing, K. Kutty, Heavy ion irradiation of zirconate pyrochlores, MRS Proceedings, Cambridge Univ Press, 2002, p. JJ11. 35.

[71] S. Buckley, Structural damage in $MgAl_2O_4$ spinel after high dose electron irradiation at elevated temperatures, Journal of Nuclear Materials 141 (1986) 387-391.

[72] Y. Satoh, C. Kinoshita, K. Nakai, Kinetic study of defect clusters in the $MgO\text{-}Al_2O_3$ system under electron-and/or ion-irradiation, Journal of Nuclear Materials 179 (1991) 399-402.

[73] F. Lu, Z. Dong, J. Zhang, T. White, R.C. Ewing, J. Lian, Tailoring the radiation tolerance of vanadate-phosphate fluorapatites by chemical composition control, RSC Advances 3(35) (2013) 15178-15184.

[74] S. Müller, M. Jenkins, C. Abromeit, H. Wollenberger, The influence of the surface on the production and development of displacement cascades in Ni_3Al and Cu_3Au, Philosophical Magazine A 75(6) (1997) 1625-1640.

[75] E. Fu, M. Caro, L. Zepeda-Ruiz, Y. Wang, K. Baldwin, E. Bringa, M. Nastasi, A. Caro, Surface effects on the radiation response of nanoporous Au foams, Applied Physics Letters 101(19) (2012) 191607.

[76] C. Sun, D. Bufford, Y. Chen, M. Kirk, Y. Wang, M. Li, H. Wang, S. Maloy, X. Zhang, In situ study of defect migration kinetics in nanoporous Ag with enhanced radiation tolerance, Scientific Reports 4 (2014).

[77] E. Bringa, J. Monk, A. Caro, A. Misra, L. Zepeda-Ruiz, M. Duchaineau, F. Abraham, M. Nastasi, S. Picraux, Y. Wang, Are nanoporous materials radiation resistant?, Nano Letters 12(7) (2011) 3351-3355.

[78] M. Demkowicz, R. Hoagland, J. Hirth, Interface structure and radiation damage resistance in Cu-Nb multilayer nanocomposites, Physical Review Letters 100(13) (2008) 136102.

[79] M. Demkowicz, A. Misra, A. Caro, The role of interface structure in controlling high helium concentrations, Current Opinion in Solid State and Materials Science 16(3) (2012) 101-108.

[80] E. Fu, A. Misra, H. Wang, L. Shao, X. Zhang, Interface enabled defects reduction in helium ion irradiated Cu/V nanolayers, Journal of Nuclear Materials 407(3) (2010) 178-188.

[81] A. Misra, M. Demkowicz, X. Zhang, R. Hoagland, The radiation damage tolerance of ultra-high strength nanolayered composites, Jom 59(9) (2007) 62-65.

[82] X. Zhang, N. Li, O. Anderoglu, H. Wang, J. Swadener, T. Höchbauer, A. Misra, R. Hoagland, Nanostructured Cu/Nb multilayers subjected to helium ion-irradiation, Nuclear Instruments and Methods in Physics Research Section B: Beam Interactions with Materials and Atoms 261(1) (2007) 1129-1132.

[83] Y. Gao, T. Yang, J. Xue, S. Yan, S. Zhou, Y. Wang, D.T. Kwok, P.K. Chu, Y. Zhang, Radiation tolerance of Cu/W multilayered nanocomposites, Journal of Nuclear Materials 413(1) (2011) 11-15.

[84] C. Sun, M. Song, K. Yu, Y. Chen, M. Kirk, M. Li, H. Wang, X. Zhang, In situ evidence of defect cluster absorption by grain boundaries in Kr ion irradiated nanocrystalline Ni, Metallurgical and Materials Transactions A 44(4) (2013) 1966-1974.

[85] W. Han, M. Demkowicz, E. Fu, Y. Wang, A. Misra, Effect of grain boundary character on sink efficiency, Acta Materialia 60(18) (2012) 6341-6351.

[86] A. Arjhangmehr, S.A.H. Feghhi, A. Esfandiyarpour, F. Hatami, An energetic and kinetic investigation of the role of different atomic grain boundaries in healing radiation damage in nickel, Journal of Materials Science 51(2) (2016) 1017-1031.

[87] X.M. Bai, A.F. Voter, R.G. Hoagland, M. Nastasi, B.P. Uberuaga, Efficient annealing of radiation damage near grain boundaries via interstitial emission, Science 327(5973) (2010) 1631-1634.

[88] D. Chen, F. Gao, B. Liu, Grain boundary resistance to amorphization of nanocrystalline silicon carbide, Scientific Reports 5 (2015).

[89] X.M. Bai, B.P. Uberuaga, The influence of grain boundaries on radiation-induced point defect production in materials: a review of atomistic studies, Jom 65(3) (2013) 360-373.

[90] S. Soulet, J. Carpéna, J. Chaumont, O. Kaitasov, M.O. Ruault, J.C. Krupa, Simulation of the α-annealing effect in apatitic structures by He-ion irradiation: Influence of the silicate/phosphate ratio and of the OH^-/F^- substitution, Nuclear Instruments and Methods in Physics Research Section B: Beam Interactions with Materials and Atoms 184(3) (2001) 383-390.

[91] S. Soulet, J. Carpéna, J. Chaumont, J.C. Krupa, M.O. Ruault, Determination of the defect creation mechanism in the mono-silicated fluoroapatite. Disorder modeling under repository conditions, Journal of Nuclear Materials 299(3) (2001) 227-234.

[92] S. Utsunomiya, S. Yudintsev, L. Wang, R. Ewing, Ion-beam and electron-beam irradiation of synthetic britholite, Journal of Nuclear Materials 322(2) (2003) 180-188.

[93] L. Wang, W. Weber, Transmission electron microscopy study of ion-beaminduced amorphization of $Ca_2La_8(SiO_4)_6O_2$, Philosophical Magazine A 79(1) (1999) 237-253.

[94] F. Lu, T. Yao, Y. Danon, J. Zhou, R.C. Ewing, J. Lian, Radiation Stability of Spark-Plasma-Sintered Lead Vanadate Iodoapatite, Journal of the American Ceramic Society 98(10) (2015) 3361-3366.

[95] F. Lu, M. Nyman, Y. Shen, Z. Dong, G. Wang, F. Zhang, R. Ewing, J. Lian, Ion Beam Irradiation-induced Amorphization in Nano-sized $K_xLn_yTa_2O_{7-v}$ Tantalate Pyrochlore, MRS Proceedings, Cambridge Univ Press, 2011, pp. mrsf10-1298-r06-02.

[96] J. Zhang, J. Lian, F. Zhang, J. Wang, A.F. Fuentes, R.C. Ewing, Intrinsic structural disorder and radiation response of nanocrystalline $Gd_2(Ti_{0.65}Zr_{0.35})_2O_7$ pyrochlore, The Journal of Physical Chemistry C 114(27) (2010) 11810-11815.

[97] H. Wang, R. Araujo, J. Swadener, Y. Wang, X. Zhang, E. Fu, T. Cagin, Ion irradiation effects in nanocrystalline TiN coatings, Nuclear Instruments and Methods in Physics Research Section B: Beam Interactions with Materials and Atoms 261(1) (2007) 1162-1166.

[98] T. Shen, Radiation tolerance in a nanostructure: Is smaller better?, Nuclear Instruments and Methods in Physics Research Section B: Beam Interactions with Materials and Atoms 266(6) (2008) 921-925.

[99] G. McMahon, T. Malis, Ultramicrotomy of nanocrystalline materials, Microscopy Research and Technique 31(4) (1995) 267-274.

[100] R. Birtcher, M. Kirk, K. Furuya, G. Lumpkin, M. Ruault, In situ transmission electron microscopy investigation of radiation effects, Journal of Materials Research 20(7) (2005) 1654-1683.

[101] C. Meis, Computational study of plutonium–neodymium fluorobritholite $Ca_9Nd_{0.5}Pu_{0.5}(SiO_4)(PO_4)_5F_2$ thermodynamic properties and threshold displacement energies, Journal of Nuclear Materials 289(1) (2001) 167-176.

[102] P. Lei, G. Ran, C. Liu, C. Ye, D. Lv, J. Lin, Y. Wu, J. Xu, In situ TEM study of microstructure evolution of Zr-Nb-Fe alloy irradiated by 800 keV Kr^{2+} ions, Materials 10(4) (2017) 437.

[103] S. Nakayama, M. Sakamoto, M. Higuchi, K. Kodaira, M. Sato, S. Kakita, T. Suzuki, K. Itoh, Oxide ionic conductivity of apatite type $Nd_{9.33}(SiO_4)_6O_2$ single crystal, Journal of the European Ceramic Society 19(4) (1999) 507-510.

[104] Y. Masubuchi, M. Higuchi, S. Kikkawa, K. Kodaira, S. Nakayama, Single crystal growth and oxide ion conductivity of oxyapatite type Sr-bearing neodymium silicate, Solid State Ionics 175(1) (2004) 357-360.

[105] W.J. Weber, A. Navrotsky, S. Stefanovsky, E.R. Vance, E. Vernaz, Materials science of high-level nuclear waste immobilization, MRS Bulletin 34(01) (2009) 46-53.

[106] R. Tisserand, M. Rebetez, M. Grivet, S. Bouffard, A. Benyagoub, F. Levesque, J. Carpena, Comparative amorphization quantification of two apatitic materials irradiated with heavy ions using XRD and RBS results, Nuclear Instruments and Methods in Physics Research Section B: Beam Interactions with Materials and Atoms 215(1) (2004) 129-136.

[107] R. Ewing, W. Weber, F. Clinard, Radiation effects in nuclear waste forms for high-level radioactive waste, Progress in Nuclear Energy 29(2) (1995) 63-127.

[108] Y. Zhang, J. Lian, C.M. Wang, W. Jiang, R.C. Ewing, W.J. Weber, Ion-induced damage accumulation and electron-beam-enhanced recrystallization in $SrTiO_3$, Physical Review B 72(9) (2005) 094112.

[109] J. Zhang, F. Zhang, M. Lang, F. Lu, J. Lian, R.C. Ewing, Ion-irradiation-induced structural transitions in orthorhombic Ln_2TiO_5, Acta Materialia 61(11) (2013) 4191-4199.

[110] A. Meldrum, L.A. Boatner, W.J. Weber, R.C. Ewing, Amorphization and recrystallization of the ABO_3 oxides, Journal of Nuclear Materials 300(2-3) (2002) 242-254.

[111] J. Lian, R.C. Ewing, L. Wang, K. Helean, Ion-beam irradiation of $Gd_2Sn_2O_7$ and $Gd_2Hf_2O_7$ pyrochlore: bond-type effect, Journal of Materials Research 19(05) (2004) 1575-1580.

[112] R.C. Ewing, A. Meldrum, L. Wang, S. Wang, Radiation-induced amorphization, Reviews in Mineralogy and Geochemistry 39(1) (2000) 319-361.

[113] J. Lian, J. Zhang, V. Pointeau, F. Zhang, M. Lang, F. Lu, C. Poinssot, R. Ewing, Response of synthetic coffinite to energetic ion beam irradiation, Journal of Nuclear Materials 393(3) (2009) 481-486.

[114] T. Chilalla, J. Mendel, Ceramics in nuclear waste management, Proceedings of an Intern. Symp. held in Cincinnati, Ohio, 30 Apr.-2 May 1979, sponsored in part by the Nuclear Division of the American Ceramic Society, 1979.

[115] W. Weber, J. Wald, H. Matzke, Effects of self-radiation damage in Cm-doped $Gd_2Ti_2O_7$ and $CaZrTi_2O_7$, Journal of Nuclear Materials 138(2) (1986) 196-209.

[116] L.L. Hench, D.E. Clark, E.L. Yen-Bower, Corrosion of glasses and glass-ceramics, Nuclear and Chemical Waste Management 1(1) (1980) 59-75.

[117] W.J. Weber, Y. Zhang, H. Xiao, L. Wang, Dynamic recovery in silicate-apatite structures under irradiation and implications for long-term immobilization of actinides, RSC Advances 2(2) (2012) 595-604.

[118] W. Weber, L. Wang, Effect of temperature and recoil-energy spectra on irradiation-induced amorphization in $Ca_2La_8(SiO_4)_6O_2$, Nuclear Instruments and Methods in Physics Research Section B: Beam Interactions with Materials and Atoms 91(1-4) (1994) 63-66.

[119] W. Weber, R. Ewing, A. Meldrum, The kinetics of alpha-decay-induced amorphization in zircon and apatite containing weapons-grade plutonium or other actinides, Journal of Nuclear Materials 250(2) (1997) 147-155.

[120] R. Devanathan, K. Sickafus, W. Weber, M. Nastasi, Effects of ionizing radiation in ceramics, Journal of Nuclear Materials 253(1) (1998) 113-119.

[121] A. Najib, J. Sansom, J. Tolchard, P. Slater, M. Islam, Doping strategies to optimise the oxide ion conductivity in apatite-type ionic conductors, Dalton Transactions (19) (2004) 3106-3109.

[122] A. Orera, E. Kendrick, D. Apperley, V. Orera, P. Slater, Effect of oxygen content on the 29 Si NMR, Raman spectra and oxide ion conductivity of the apatite series, $La_{8+x}Sr_{2-x}(SiO_4)_6O_{2+x/2}$, Dalton Transactions (39) (2008) 5296-5301.

[123] J.E. Sansom, J.R. Tolchard, M.S. Islam, D. Apperley, P.R. Slater, Solid state 29Si NMR studies of apatite-type oxide ion conductors, Journal of Materials Chemistry 16(15) (2006) 1410-1413.

[124] A.C.S. Meeting, Environmental Issues and Waste Management Technologies in the Ceramic and Nuclear Industries, American Ceramic Society 2000.

[125] S. Wang, L. Wang, R. Ewing, Irradiation-induced amorphization: effects of temperature, ion mass, cascade size, and dose rate, Physical Review B 63(2) (2000) 024105.

[126] G. Li, D. Geng, M. Shang, Y. Zhang, C. Peng, Z. Cheng, J. Lin, Color tuning luminescence of $Ce^{3+}/Mn^{2+}/Tb^{3+}$-triactivated $Mg_2Y_8(SiO_4)_6O_2$ via energy transfer: potential single-phase white-light-emitting phosphors, The Journal of Physical Chemistry C 115(44) (2011) 21882-21892.

[127] Y. Shen, A. Tok, Z. Dong, Synthesis and crystal structure characterization of silicate apatite $Sr_2Y_8(SiO_4)_6O_2$, Journal of the American Ceramic Society 93(4) (2010) 1176-1182.

[128] I. Brown, The chemical bond in inorganic chemistry, the bond valence model. IUCr monographs on crystallography 12. International Union of Crystallography, Oxford Science Publications, Oxford, 2002.

[129] G. Blasse, Influence of local charge compensation on site occupation and luminescence of apatites, Journal of Solid State Chemistry 14(2) (1975) 181-184.

[130] W. Weber, L. Wang, Effect of temperature and recoil-energy spectra on irradiation-induced amorphization in $Ca_2La_8(SiO_4)_6O_2$, Nuclear Instruments and Methods in Physics Research Section B: Beam Interactions with Materials and Atoms 91(1) (1994) 63-66.

[131] I.T. Bae, Y. Zhang, W.J. Weber, M. Higuchi, L.A. Giannuzzi, Electron-beam induced recrystallization in amorphous apatite, Applied Physics Letters 90(2) (2007) 21912-21912.

[132] I.T. Bae, Y. Zhang, W.J. Weber, M. Ishimaru, Y. Hirotsu, M. Higuchi, Temperature dependence of electron-beam induced effects in amorphous apatite, Nuclear Instruments and Methods in Physics Research Section B: Beam Interactions with Materials and Atoms 266(12) (2008) 3037-3042.

[133] J. Reyes-Gasga, R. Garcia-Garcia, E. Brès, Electron beam interaction, damage and reconstruction of hydroxyapatite, Physica B: Condensed Matter 404(12) (2009) 1867-1873.

[134] B.P. Uberuaga, S. Choudhury, A. Caro, Ideal sinks are not always ideal: Radiation damage accumulation in nanocomposites, Journal of Nuclear Materials 462 (2015) 402-408.

[135] S. Dey, J.W. Drazin, Y. Wang, J.A. Valdez, T.G. Holesinger, B.P. Uberuaga, R.H. Castro, Radiation Tolerance of Nanocrystalline Ceramics: Insights from Yttria Stabilized Zirconia, Scientific Reports 5 (2015).

[136] B. Radiguet, A. Etienne, P. Pareige, X. Sauvage, R. Valiev, Irradiation behavior of nanostructured 316 austenitic stainless steel, Journal of Materials Science 43(23-24) (2008) 7338-7343.

[137] R.W. Grimes, R.J. Konings, L. Edwards, Greater tolerance for nuclear materials, Nature Materials 7(9) (2008) 683-685.

[138] T.D. Shen, S. Feng, M. Tang, J.A. Valdez, Y. Wang, K.E. Sickafus, Enhanced radiation tolerance in nanocrystalline $MgGa_2O_4$, Applied Physics Letters 90(26) (2007) 263115-263500.

[139] J. Lian, K. Helean, B. Kennedy, L. Wang, A. Navrotsky, R. Ewing, Effect of structure and thermodynamic stability on the response of lanthanide stannate pyrochlores to ion beam irradiation, The Journal of Physical Chemistry B 110(5) (2006) 2343-2350.

[140] F. Lu, J. Zhang, M. Huang, F. Namavar, R.C. Ewing, J. Lian, Phase transformation of nanosized ZrO_2 upon thermal annealing and intense radiation, The Journal of Physical Chemistry C 115(15) (2011) 7193-7201.

[141] J. Jiang, J. Olsen, L. Gerward, D. Frost, D. Rubie, J. Peyronneau, Structural stability in nanocrystalline ZnO, EPL (Europhysics Letters) 50(1) (2000) 48.

[142] J. McHale, A. Auroux, A. Perrotta, A. Navrotsky, Surface energies and thermodynamic phase stability in nanocrystalline aluminas, Science 277(5327) (1997) 788-791.

[143] A. Meldrum, L.A. Boatner, R.C. Ewing, Size effects in the irradiation-induced crystalline-to-amorphous transformation, Nuclear Instruments and Methods in Physics Research Section B: Beam Interactions with Materials and Atoms 207(1) (2003) 28-35.

[144] G. Kachurin, M.O. Ruault, A. Gutakovsky, O. Kaıtasov, S. Yanovskaya, K. Zhuravlev, H. Bernas, Light particle irradiation effects in Si nanocrystals, Nuclear Instruments and Methods in Physics Research Section B: Beam Interactions with Materials and Atoms 147(1) (1999) 356-360.

[145] L. Jamison, K. Sridharan, S. Shannon, I. Szlufarska, Temperature and irradiation species dependence of radiation response of nanocrystalline silicon carbide, Journal of Materials Research 29(23) (2014) 2871-2880.

[146] J. Lian, L. Wang, K. Sun, R.C. Ewing, In situ TEM of radiation effects in complex ceramics, Microscopy Research and Technique 72(3) (2009) 165-181.

[147] W. Weber, Models and mechanisms of irradiation-induced amorphization in ceramics, Nuclear Instruments and Methods in Physics Research Section B: Beam Interactions with Materials and Atoms 166 (2000) 98-106.

[148] R. De Tendler, C. Rodriguez, L. Gallego, J. Alonso, Free-energies of the Ti-Ni, Fe-Ni and Mo-Ni alloys in relation to their behaviour under particle irradiation, Journal of Materials Science 31(24) (1996) 6395-6402.

[149] F. Lu, J. Wang, M. Lang, M. Toulemonde, F. Namavar, C. Trautmann, J. Zhang, R.C. Ewing, J. Lian, Amorphization of nanocrystalline monoclinic ZrO_2 by swift heavy ion irradiation, Physical Chemistry Chemical Physics 14(35) (2012) 12295-12300.

[150] S. Ishino, A review of in situ observation of defect production with energetic heavy ions, Journal of Nuclear Materials 251 (1997) 225-236.

[151] M. Ghaly, K. Nordlund, R. Averback, Molecular dynamics investigations of surface damage produced by kiloelectronvolt self-bombardment of solids, Philosophical Magazine A 79(4) (1999) 795-820.

[152] D. Norris, The use of the high voltage electron microscope to simulate fast neutron-induced void swelling in metals, Journal of Nuclear Materials 40(1) (1971) 66-76.

[153] E. Landi, A. Tampieri, G. Celotti, S. Sprio, Densification behaviour and mechanisms of synthetic hydroxyapatites, Journal of the European Ceramic Society 20(14) (2000) 2377-2387.

[154] F. Lu, T. Yao, Y. Danon, J. Zhou, R.C. Ewing, J. Lian, Radiation Stability of Spark-Plasma-Sintered Lead Vanadate Iodoapatite, Journal of the American Ceramic Society 98(10) (2015) 3361-3366.

[155] H.S. Lee, T. Mizoguchi, J. Mistui, T. Yamamoto, S.J. Kang, Y. Ikuhara, Defect energetics in $SrTiO_3$ symmetric tilt grain boundaries, Physical Review B 83(10) (2011) 104110.

[156] F. Ma, K.W. Xu, Using dangling bond density to characterize the surface energy of nanomaterials, Surface and Interface Analysis 39(7) (2007) 611-614.

[157] W. Zhu, P. Wu, Surface energetics of hydroxyapatite: a DFT study, Chemical Physics Letters 396(1-3) (2004) 38-42.

[158] E. Dos Santos, M. Farina, G. Soares, K. Anselme, Surface energy of hydroxyapatite and β-tricalcium phosphate ceramics driving serum protein adsorption and osteoblast adhesion, Journal of Materials Science: Materials in Medicine 19(6) (2008) 2307-2316.

[159] Q. Song, C. Wang, S. Wen, Electron structure of a grain boundary and a crystal of calcium phosphate bioceramic (hydroxyapatite), Philosophical Magazine A 77(5) (1998) 1309-1321.

[160] X. Zhang, H. Yin, H.G. Boyen, P. Ziemann, M. Ozawa, Effects of crystalline quality on the phase stability of cubic boron nitride thin films under medium-energy ion irradiation, Diamond and Related Materials 14(9) (2005) 1482-1488.

[161] G. Paternò, V. Robbiano, K. Fraser, C. Frost, V.G. Sakai, F. Cacialli, Neutron Radiation Tolerance of Two Benchmark Thiophene-Based Conjugated Polymers: the Importance of Crystallinity for Organic Avionics, Scientific Reports 7 (2017).

[162] E.M. Kornacka, G. Przybytniak, W. Święszkowski, The influence of crystallinity on radiation stability of UHMWPE, Radiation Physics and Chemistry 84 (2013) 151-156.

[163] X. Zhong, L. Yu, W. Zhao, Y. Zhang, J. Sun, Radiation stability of PTFE with different crystallinity, Journal of Applied Polymer Science 48(4) (1993) 741-744.

[164] J. Zhou, T. Yao, J. Lian, Y. Shen, Z. Dong, F. Lu, Radiation-induced amorphization of Ce-doped $Mg_2Y_8(SiO_4)_6O_2$ silicate apatite, Nuclear Instruments and Methods in Physics Research Section B: Beam Interactions with Materials and Atoms 379 (2016) 102-106.

[165] S. Zinkle, V. Skuratov, D. Hoelzer, On the conflicting roles of ionizing radiation in ceramics, Nuclear Instruments and Methods in Physics Research Section B: Beam Interactions with Materials and Atoms 191(1) (2002) 758-766.

[166] A. Meldrum, L. Boatner, R. Ewing, Electron-irradiation-induced nucleation and growth in amorphous $LaPO_4$, $ScPO_4$, and zircon, Journal of Materials Research 12(07) (1997) 1816-1827.

[167] I.T. Bae, Y. Zhang, W.J. Weber, M. Ishimaru, Y. Hirotsu, M. Higuchi, Ionization-induced effects in amorphous apatite at elevated temperatures, Journal of Materials Research 23(04) (2008) 962-967.

[168] Z. Li, H. Zhang, Y. Xu, Direct observation of electron-beam-induced nucleation and growth in amorphous GaAs, Materials Science in Semiconductor Processing 7(1) (2004) 19-25.

[169] Z. Huang, J. Qi, L. Zhou, Z. Feng, X. Yu, Y. Gong, M. Yang, Q. Shi, N. Wei, T. Lu, Fast crystallization of amorphous $Gd_2Zr_2O_7$ induced by thermally activated electron-beam irradiation, Journal of Applied Physics 118(21) (2015) 214901.

[170] A. Meldrum, L.A. Boatner, W.J. Weber, R.C. Ewing, Amorphization and recrystallization of the ABO_3 oxides, Journal of Nuclear Materials 300(2) (2002) 242-254.

[171] Z. Xu, A. Ngan, TEM study of electron beam-induced crystallization of amorphous GeSi films, Philosophical Magazine Letters 84(11) (2004) 719-728.

[172] A. Meldrum, L. Wang, R. Ewing, Electron-irradiation-induced phase segregation in crystalline and amorphous apatite: A TEM study, American Mineralogist 82(9-10) (1997) 858-869.

[173] J. Reyes-Gasga, R. Garcıa-Garcıa, Analysis of the electron-beam radiation damage of TEM samples in the acceleration energy range from 0.1 to 2MeV using the standard theory for fast electrons, Radiation Physics and Chemistry 64(5) (2002) 359-367.

[174] G. Lulli, P. Merli, M.V. Antisari, Solid-phase epitaxy of amorphous silicon induced by electron irradiation at room temperature, Physical Review B 36(15) (1987) 8038.

[175] M. Bench, I. Robertson, M. Kirk, I. Jenčič, Production of amorphous zones in GaAs by the direct impact of energetic heavy ions, Journal of Applied Physics 87(1) (2000) 49-56.

[176] A. Meldrum, L. Boatner, R. Ewing, Electron-irradiation-induced nucleation and growth in amorphous $LaPO_4$, $ScPO_4$, and zircon, Journal of Materials Research 12(7) (1997) 1816-1827.

[177] M.L. Miller, R.C. Ewing, Image simulation of partially amorphous materials, Ultramicroscopy 48(1) (1993) 203-237.

[178] R.M. Roque-Malherbe, The physical chemistry of materials: Energy and environmental applications, CRC Press 2009.

[179] S. Senkader, C. Wright, Models for phase-change of $Ge_2Sb_2Te_5$ in optical and electrical memory devices, Journal of Applied Physics 95(2) (2004) 504-511.

[180] I. Jencic, M. Bench, I. Robertson, M. Kirk, Electron-beam-induced crystallization of isolated amorphous regions in Si, Ge, GaP, and GaAs, Journal of Applied Physics 78(2) (1995) 974-982.

[181] G. Lulli, P. Merli, Comparison of results and models of solid-phase epitaxial growth of implanted Si layers induced by electron-and ion-beam irradiation, Physical Review B 47(21) (1993) 14023.

[182] R. Elliman, D. Jacobson, J. Linnros, J. Poate, Ion-beam-induced epitaxy and interfacial segregation of Au in amorphous silicon, Applied Physics Letters 51(5) (1987) 314-316.

[183] S. Fisher, On the temperature rise in electron irradiated foils, Radiation Effects 5(2) (1970) 239-243.

[184] E. Segrè, Experimental nuclear physics, 1953.

[185] T. Coelho, E. Nogueira, W. Weinand, W. Lima, A. Steimacher, A. Medina, M. Baesso, A. Bento, Thermal properties of natural nanostructured hydroxyapatite extracted from fish bone waste, Journal of Applied Physics 101(8) (2007) 084701.

[186] J. Frantz, J. Tarus, K. Nordlund, J. Keinonen, Mechanism of electron-irradiation-induced recrystallization in Si, Physical Review B 64(12) (2001) 125313.

[187] S. Zinkle, C. Kinoshita, Defect production in ceramics, Journal of Nuclear Materials 251 (1997) 200-217.

[188] T. Yang, S. Xia, S. Liu, C. Wang, S. Liu, Y. Zhang, J. Xue, S. Yan, Y. Wang, Effects of Al addition on microstructure and mechanical properties of $Al_xCoCrFeNi$ high-entropy alloy, Materials Science and Engineering: A 648 (2015) 15-22.

[189] W.R. Wang, W.L. Wang, S.C. Wang, Y.C. Tsai, C.H. Lai, J.W. Yeh, Effects of Al addition on the microstructure and mechanical property of $Al_xCoCrFeNi$ high-entropy alloys, Intermetallics 26 (2012) 44-51.

[190] Z. Tang, M.C. Gao, H. Diao, T. Yang, J. Liu, T. Zuo, Y. Zhang, Z. Lu, Y. Cheng, Y. Zhang, Aluminum alloying effects on lattice types, microstructures, and mechanical behavior of high-entropy alloys systems, Jom 65(12) (2013) 1848-1858.

[191] S. Xia, M.C. Gao, T. Yang, P.K. Liaw, Y. Zhang, Phase stability and microstructures of high entropy alloys ion irradiated to high doses, Journal of Nuclear Materials 480 (2016) 100-108.

[192] J. Lian, J. Zhang, F. Namavar, Y. Zhang, F. Lu, H. Haider, K. Garvin, W.J. Weber, R.C. Ewing, Ion beam-induced amorphous-to-tetragonal phase transformation and grain growth of nanocrystalline zirconia, Nanotechnology 20(24) (2009) 245303.

[193] Y. Zhang, P.D. Edmondson, T. Varga, S. Moll, F. Namavar, C. Lan, W.J. Weber, Structural modification of nanocrystalline ceria by ion beams, Physical Chemistry Chemical Physics 13(25) (2011) 11946-11950.

[194] Y. Zhang, W. Jiang, C. Wang, F. Namavar, P.D. Edmondson, Z. Zhu, F. Gao, J. Lian, W.J. Weber, Grain growth and phase stability of nanocrystalline cubic zirconia under ion irradiation, Physical Review B 82(18) (2010) 184105.

[195] D.S. Aidhy, Y. Zhang, W.J. Weber, A fast grain-growth mechanism revealed in nanocrystalline ceramic oxides, Scripta Materialia 83 (2014) 9-12.

[196] D. Kaoumi, A. Motta, R. Birtcher, Grain growth in nanocrystalline metal thin films under in situ ion-beam irradiation, Effects of Radiation on Materials: 23rd International Symposium, ASTM International, 2008.

[197] A. Haslam, S. Phillpot, D. Wolf, D. Moldovan, H. Gleiter, Mechanisms of grain growth in nanocrystalline fcc metals by molecular-dynamics simulation, Materials Science and Engineering: A 318(1) (2001) 293-312.

[198] L.J. Moore, R.D. Dear, M.D. Summers, R.P. Dullens, G.A. Ritchie, Direct observation of grain rotation-induced grain coalescence in two-dimensional colloidal crystals, Nano letters 10(10) (2010) 4266-4272.

[199] P. Edmondson, Y. Zhang, S. Moll, F. Namavar, W.J. Weber, Irradiation effects on microstructure change in nanocrystalline ceria-Phase, lattice stress, grain size and boundaries, Acta Materialia 60(15) (2012) 5408-5416.

[200] W. Liu, C. Zhang, Y. Ji, Z. Yang, H. Zang, T. Shen, L. Chen, Irradiation-induced grain growth in nanocrystalline reduced activation ferrite/martensite steel, Applied Physics Letters 105(12) (2014) 121905.

[201] Y. Zhang, D.S. Aidhy, T. Varga, S. Moll, P.D. Edmondson, F. Namavar, K. Jin, C.N. Ostrouchov, W.J. Weber, The effect of electronic energy loss on irradiation-induced grain growth in nanocrystalline oxides, Physical Chemistry Chemical Physics 16(17) (2014) 8051-8059.

[202] Y. Zhou, Y. Zhang, F. Wang, G. Chen, Phase transformation induced by lattice distortion in multiprincipal component $CoCrFeNiCu_xAl_{1-x}$ solid-solution alloys, Applied Physics Letters 92(24) (2008) 241917.

[203] J.C. Liu, J. Li, J. Mayer, Temperature effect on ion-irradiation-induced grain growth in Cu thin films, Journal of Applied Physics 67(5) (1990) 2354-2358.

[204] D. Kaoumi, A. Motta, R. Birtcher, Grain growth in Zr-Fe thin films during in situ ion irradiation in a TEM, Nuclear Instruments and Methods in Physics Research Section B: Beam Interactions with Materials and Atoms 242(1) (2006) 490-493.

[205] D. Kaoumi, A. Motta, R. Birtcher, A thermal spike model of grain growth under irradiation, Journal of Applied Physics 104(7) (2008) 073525.

[206] W. Johnson, Y. Cheng, M. Van Rossum, M. Nicolet, When is thermodynamics relevant to ion-induced atomic rearrangements in metals?, Nuclear Instruments and Methods in Physics Research Section B: Beam Interactions with Materials and Atoms 7 (1985) 657-665.

[207] J.C. Liu, Ion-irradiation-induced grain growth and lateral thin-film reactions, Cornell University, Ithaca, NY (USA), 1989.

[208] C. Kittel, Introduction to solid state physics, Wiley 2005.

[209] J.C. Liu, M. Nastasi, J. Mayer, Ion irradiation induced grain growth in Pd polycrystalline thin films, Journal of Applied Physics 62(2) (1987) 423-428.

[210] M.S. Anzorena, A. Bertolo, L. Gagetti, A. Kreiner, H. Mosca, G. Bozzolo, M. del Grosso, Characterization and modeling of a MoTaVWZr high entropy alloy, Materials & Design 111 (2016) 382-388.

[211] H.G. Kim, Y.H. Kim, B.K. Choi, Y.H. Jeong, Effect of alloying elements (Cu, Fe, and Nb) on the creep properties of Zr alloys, Journal of Nuclear Materials 359(3) (2006) 268-273.

[212] C.C. Juan, K.K. Tseng, W.L. Hsu, M.H. Tsai, C.W. Tsai, C.M. Lin, S. K. Chen, S.J. Lin, J.W. Yeh, Solution strengthening of ductile refractory $HfMo_xNbTaTiZr$ high-entropy alloys, Materials Letters 175 (2016) 284-287.

[213] M.C. Gao, B. Zhang, S. Yang, S. Guo, Senary refractory high-entropy alloy HfNbTaTiVZr, Metallurgical and Materials Transactions A 47(7) (2016) 3333-3345.

[214] Z. Han, X. Liu, S. Zhao, Y. Shao, J. Li, K. Yao, Microstructure, phase stability and mechanical properties of Nb-Ni-Ti-Co-Zr and Nb-Ni-Ti-Co-Zr-Hf high entropy alloys, Progress in Natural Science: Materials International 25(5) (2015) 365-369.

[215] O. Senkov, J. Scott, S. Senkova, D. Miracle, C. Woodward, Microstructure and room temperature properties of a high-entropy TaNbHfZrTi alloy, Journal of Alloys and Compounds 509(20) (2011) 6043-6048.

[216] O. Senkov, J. Scott, S. Senkova, F. Meisenkothen, D. Miracle, C. Woodward, Microstructure and elevated temperature properties of a refractory TaNbHfZrTi alloy, Journal of Materials Science 47(9) (2012) 4062-4074.

[217] G. Dirras, L. Lilensten, P. Djemia, M. Laurent-Brocq, D. Tingaud, J.P. Couzinié, L. Perrière, T. Chauveau, I. Guillot, Elastic and plastic properties of as-cast equimolar TiHfZrTaNb high-entropy alloy, Materials Science and Engineering: A 654 (2016) 30-38.

[218] T. Nagase, A. Takeuchi, K. Amiya, T. Egami, Solid state amorphization of metastable $Al_{0.5}$TiZrPdCuNi high entropy alloy investigated by high voltage electron microscopy, Materials Chemistry and Physics 210 (2018) 291-300.

[219] D. Laurencin, D. Vantelon, V. Briois, C. Gervais, A. Coulon, A. Grandjean, L. Campayo, Investigation of the local environment of iodate in hydroxyapatite by combination of X-ray absorption spectroscopy and DFT modeling, RSC Advances 4(28) (2014) 14700-14707.

[220] L. Campayo, A. Grandjean, A. Coulon, R. Delorme, D. Vantelon, D. Laurencin, Incorporation of iodates into hydroxyapatites: a new approach for the confinement of radioactive iodine, Journal of Materials Chemistry 21(44) (2011) 17609-17611.

[221] A. Coulon, D. Laurencin, A. Grandjean, C.C.D. Coumes, S. Rossignol, L. Campayo, Immobilization of iodine into a hydroxyapatite structure prepared by cementation, Journal of Materials Chemistry A 2(48) (2014) 20923-20932.

[222] J. Wang, Incorporation of iodine into apatite structure: a crystal chemistry approach using Artificial Neural Network, Frontiers in Earth Science 3 (2015) 20.

[223] M. Lambrecht, L. Malerba, Positron annihilation spectroscopy on binary Fe-Cr alloys and ferritic/martensitic steels after neutron irradiation, Acta Materialia 59(17) (2011) 6547-6555.

[224] J.F. Stubbins, Void swelling and radiation-induced phase transformation in high purity Fe-Ni-Cr alloys, Journal of Nuclear Materials 141 (1986) 748-753.

[225] E. Getto, K. Sun, A. Monterrosa, Z. Jiao, M. Hackett, G. Was, Void swelling and microstructure evolution at very high damage level in self-ion irradiated ferritic-martensitic steels, Journal of Nuclear Materials 480 (2016) 159-176.

[226] M. Griffiths, D. Faulkner, R. Styles, Neutron damage in α-titanium, Journal of Nuclear Materials 119(2-3) (1983) 189-207.

[227] M. Griffiths, R. Gilbert, C. Coleman, Grain boundary sinks in neutron-irradiated Zr and Zr-alloys, Journal of Nuclear Materials 159 (1988) 405-416.

[228] Z. Jiao, G. Was, Segregation behavior in proton-and heavy-ion-irradiated ferritic–martensitic alloys, Acta Materialia 59(11) (2011) 4467-4481.

[229] T. Allen, J. Busby, G. Was, E. Kenik, On the mechanism of radiation-induced segregation in austenitic Fe–Cr–Ni alloys, Journal of Nuclear Materials 255(1) (1998) 44-58.

[230] Y. Grandjean, P. Bellon, G. Martin, Kinetic model for equilibrium and nonequilibrium segregation in concentrated alloys under irradiation, Physical Review B 50(6) (1994) 4228.

APPENDIX A DAMAGE PRODUCTION UNDER 1 MEV KR IONS BY USING SRIM

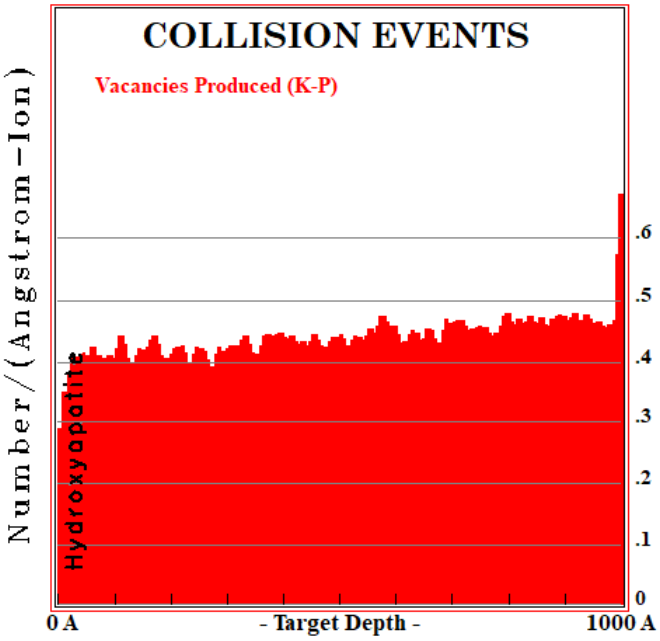

Figure A.1 Damage production of hydroxyapatite under 1 MeV Kr ions by using SRIM. The number of target displacements per ion per angstrom is estimated to be 0.42/angstrom/ion

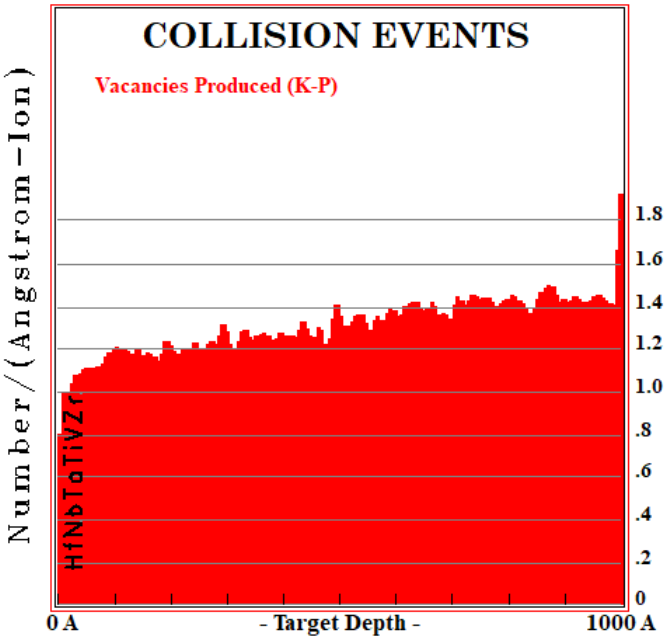

Figure A.2 Damage production of HfNbTaTiVZr alloy under 1 MeV Kr ions by using SRIM. The number of target displacements per ion per angstrom is estimated to be 1.4/angstrom/ion

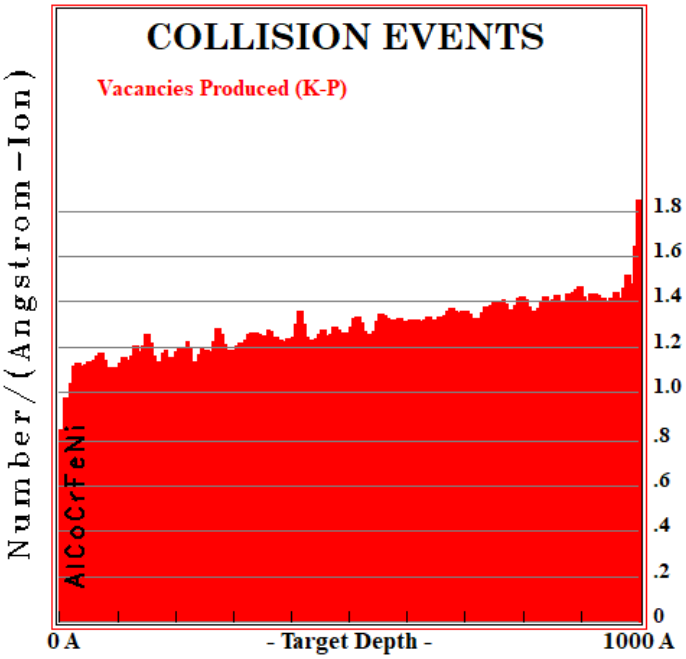

Figure A.3 Damage production of AlCoCrFeNi alloy under 1 MeV Kr ions by using SRIM. The number of target displacements per ion per angstrom is estimated to be 1.4/angstrom/ion

APPENDIX B TEM SAMPLE PREPARATION BY FOCUS ION BEAM

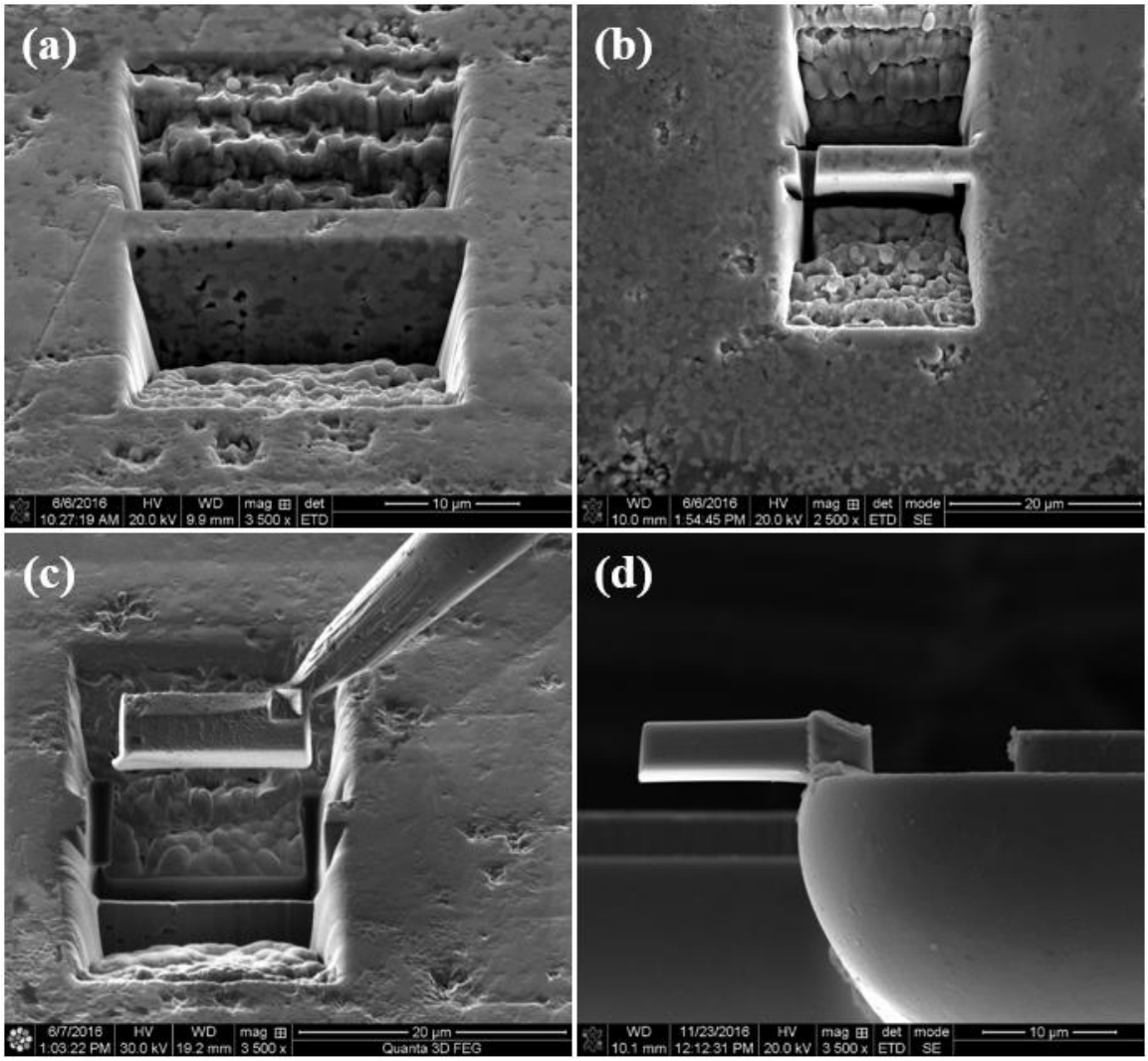

Figure B. TEM sample preparation of HfNbTaTiVZr alloy by focus ion beam: (a) (b) G-cut, (c) Lift-out, (d) Attachment on Cu TEM grid. The following sample thinning was not listed here

APPENDIX C SEM IMAGE OF NANOPARTICLE AND NANOCRYSTALLINE HYDROXYAPATITE

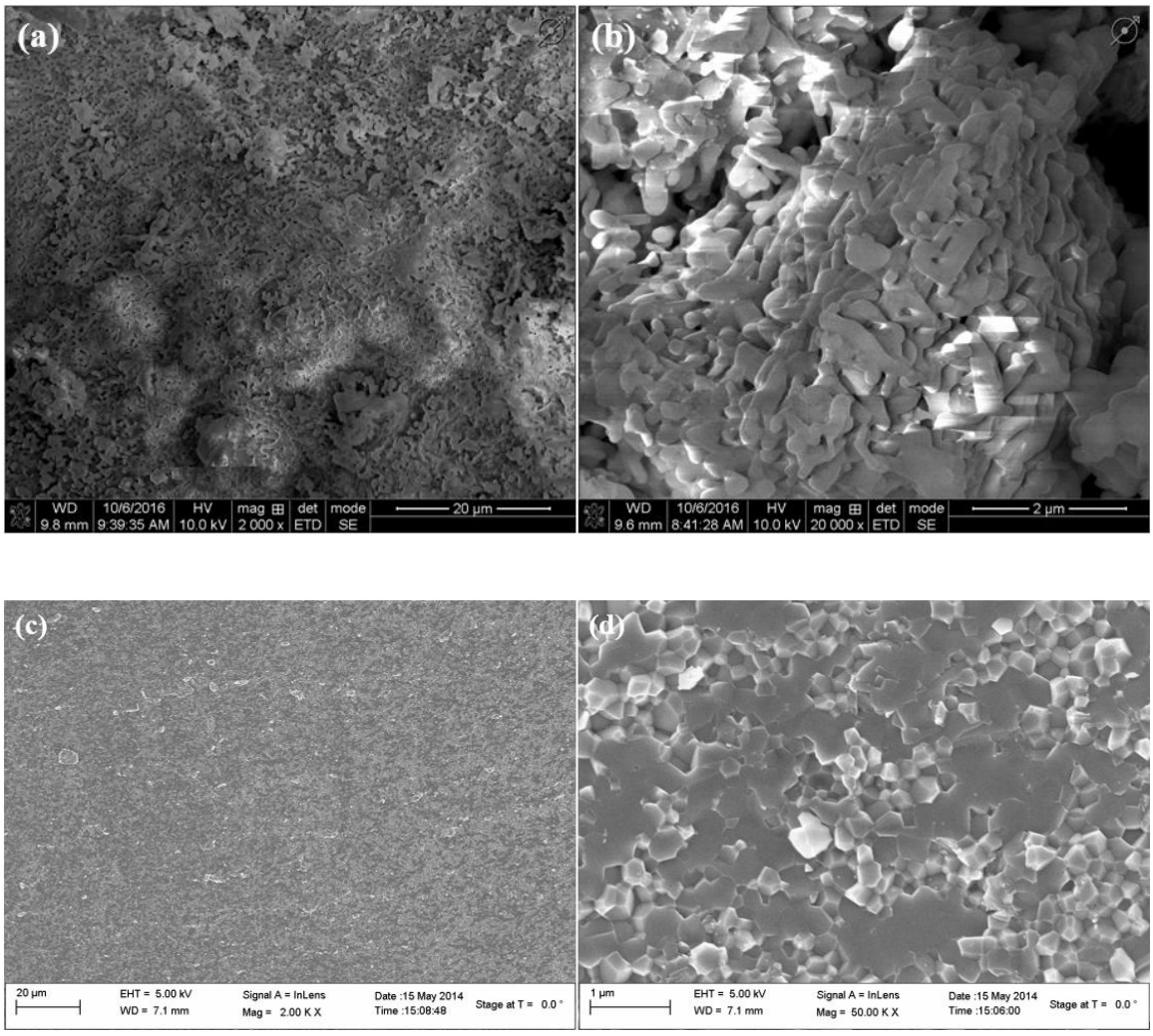

Figure C. SEM image showed the morphology of (a)(b) hydroxyapatite nanoparticle, (c)(d) densified nanocrystalline hydroxyapatite

APPENDIX D GRAIN SIZE DISTRIBUTION OF ELECTRON IRRADIATED HYDROXYAPATITE

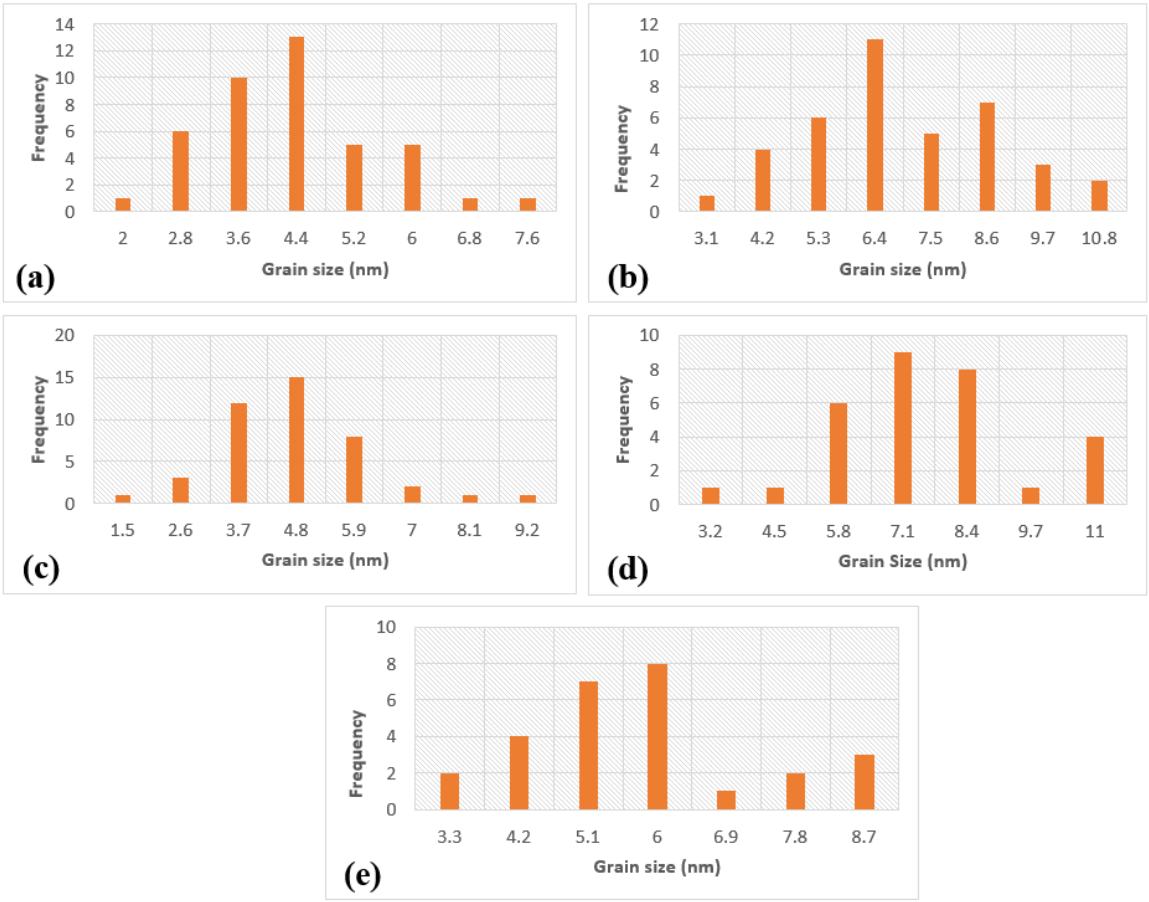

Figure D. Grain size distribution of ion-irradiation-induced amorphous hydroxyapatite $Ca_{10}(PO_4)_6(OH)_2$ under the 200 keV electron irradiation at room temperature: (a) particle size of 20 nm and current density of 100 *p*A/cm^2 (6.25×10^8 e$^-$ cm^{-2} s^{-1}); (b) particle size of 20 nm and current density of 400 *p*A/cm^2 (2.5×10^9 e$^-$ cm^{-2} s^{-1}); (c) particle size of 60 nm and current density of 30 *p*A/cm^2 (1.875×10^8 e$^-$ cm^{-2} s^{-1}); (d) particle size of 60 nm and current density of 120 *p*A/cm^2 (7.5×10^8 e$^-$ cm^{-2} s^{-1}); (e) particle size of 280 nm and current density of 30 *p*A/cm^2 (1.875×10^8 e$^-$ cm^{-2} s^{-1}).

APPENDIX E IODINE INCORPORATED APATITE STRUCTURE

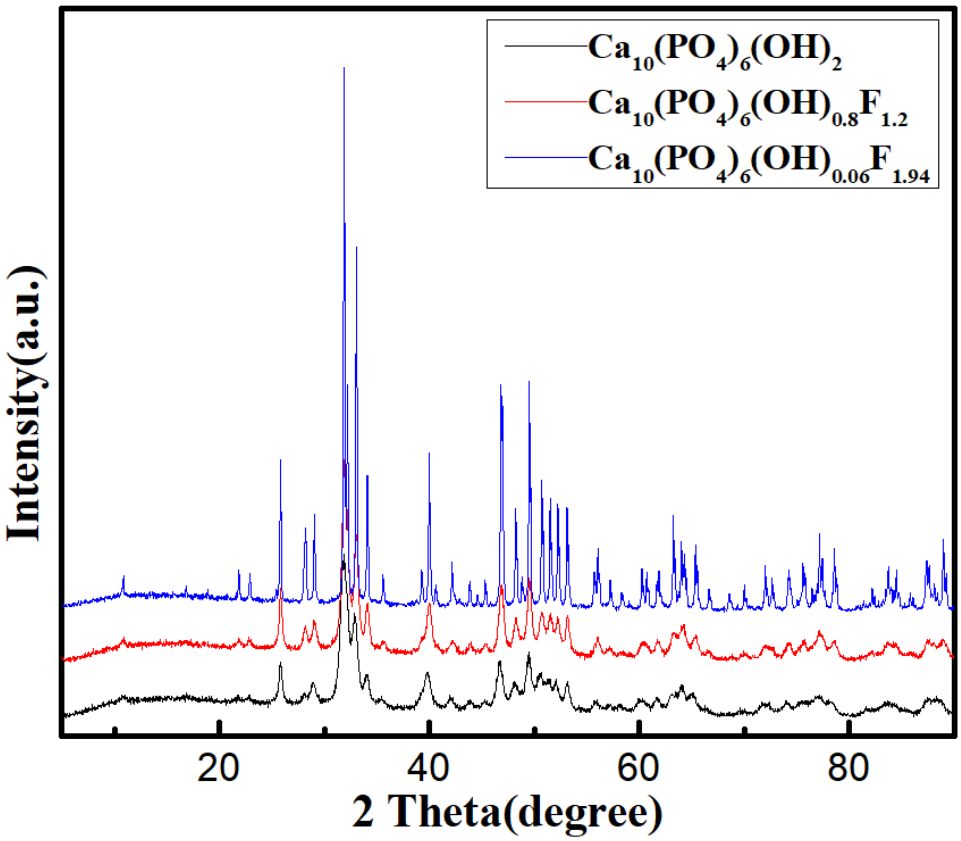

Figure E.1 XRD patterns for the different content of fluorine incorporated hydroxyapatite, showed different fluorine can be incorporated into the hydroxyapatite structure

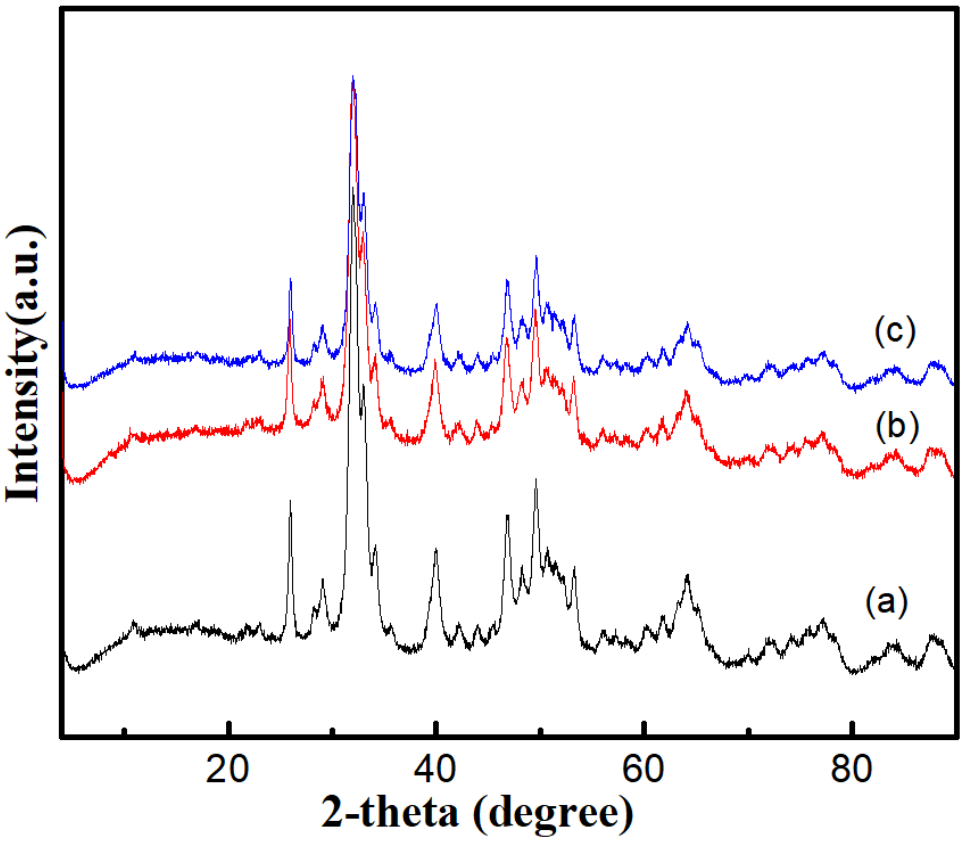

Figure E.2 XRD patterns for iodine incorporated hydroxyapatite, the patterns showed no difference, suggesting iodine was only physically soaked on the nanoparticle surface, not incorporated into the structure: (a) hydroxyapatite database, (b) (c) different iodine soaked hydroxyapatite structure

APPENDIX F TEM-EDS ANALYSIS OF RIS FOR HFNBTATIVZR ALLOY

eZAF Smart Quant Results

Element	Weight %	Atomic %	Net Int.	Error %	Kratio	Z	R	A	F
TiK	20.88	35.29	3141.46	8.14	0.0577	1.0074	0.8466	0.2581	1.0623
V K	21.71	34.50	3608.88	8.04	0.0623	0.9909	0.8537	0.2707	1.0693
HfL	18.53	8.40	3844.68	3.21	0.1686	0.9956	1.1947	0.7940	1.1504
TaL	28.64	12.81	5703.81	2.75	0.2506	0.9982	1.2011	0.8021	1.0924
ZrK	5.26	4.67	1278.87	8.92	0.0233	0.9976	0.9757	0.3360	1.3231
NbK	4.97	4.33	1182.12	8.76	0.0246	1.0068	0.9828	0.3662	1.3438

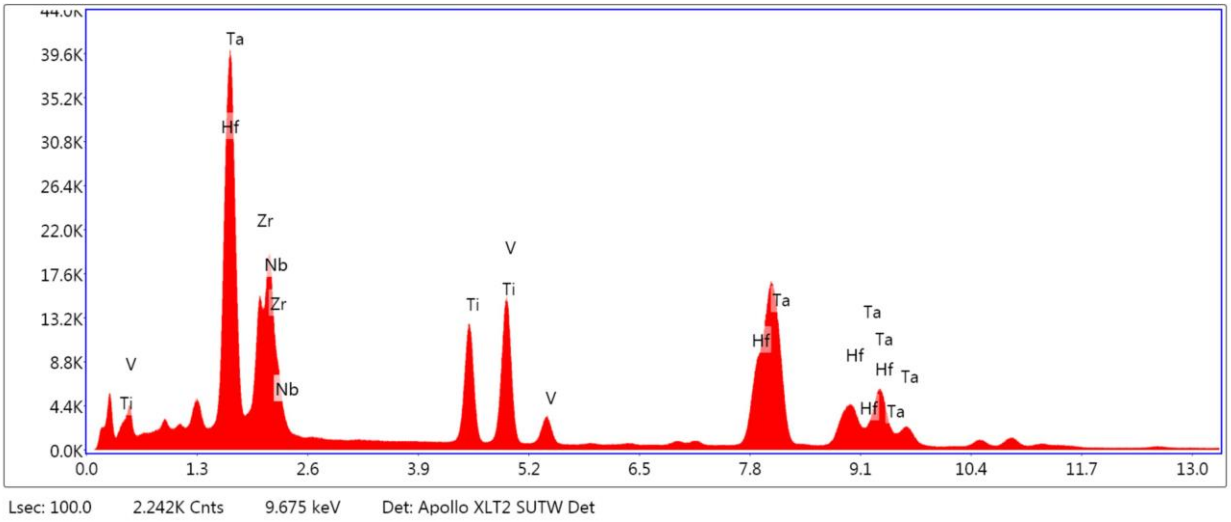

Figure F.1 EDS analysis of radiation-induced segregation for HfNbTaTiVZr alloy showed the chemical composition percentage of different elements corresponding to Figure 6.3 point a

eZAF Smart Quant Results

Element	Weight %	Atomic %	Net Int.	Error %	Kratio	Z	R	A	F
TiK	21.29	36.53	2030.90	8.29	0.0580	1.0074	0.8430	0.2544	1.0628
V K	19.79	31.93	2087.90	8.18	0.0560	0.9908	0.8501	0.2668	1.0712
HfL	21.12	9.73	2831.10	3.13	0.1931	0.9955	1.1895	0.8028	1.1435
TaL	27.23	12.37	3513.10	2.76	0.2400	0.9980	1.1959	0.8081	1.0927
ZrK	5.98	5.39	924.17	9.04	0.0262	0.9975	0.9715	0.3332	1.3194
NbK	4.59	4.06	692.71	9.05	0.0225	1.0066	0.9786	0.3624	1.3426

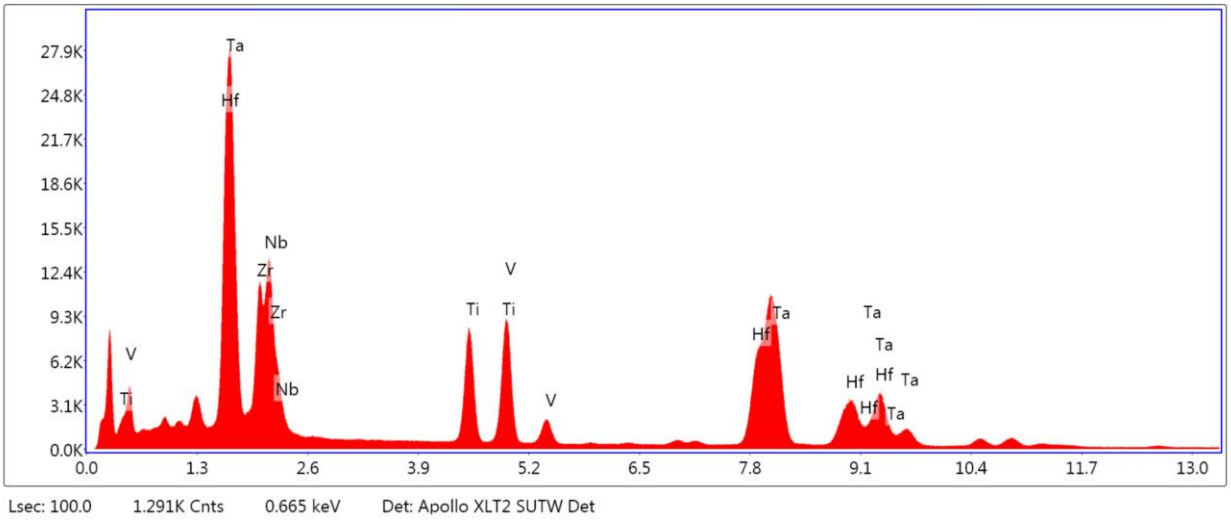

Figure F.2 EDS analysis of radiation-induced segregation for HfNbTaTiVZr alloy showed the chemical composition percentage of different elements corresponding to Figure 6.3 point b

eZAF Smart Quant Results

Element	Weight %	Atomic %	Net Int.	Error %	Kratio	Z	R	A	F
TiK	19.27	34.36	844.38	8.65	0.0510	1.0077	0.8339	0.2463	1.0658
V K	18.83	31.57	916.76	8.54	0.0520	0.9911	0.8409	0.2593	1.0754
HfL	21.72	10.39	1403.39	3.23	0.2023	0.9955	1.1766	0.8155	1.1474
TaL	29.88	14.11	1849.37	2.74	0.2671	0.9981	1.1830	0.8200	1.0922
ZrK	5.71	5.34	403.23	9.63	0.0242	0.9975	0.9612	0.3223	1.3180
NbK	4.60	4.23	318.21	10.28	0.0218	1.0067	0.9683	0.3512	1.3418

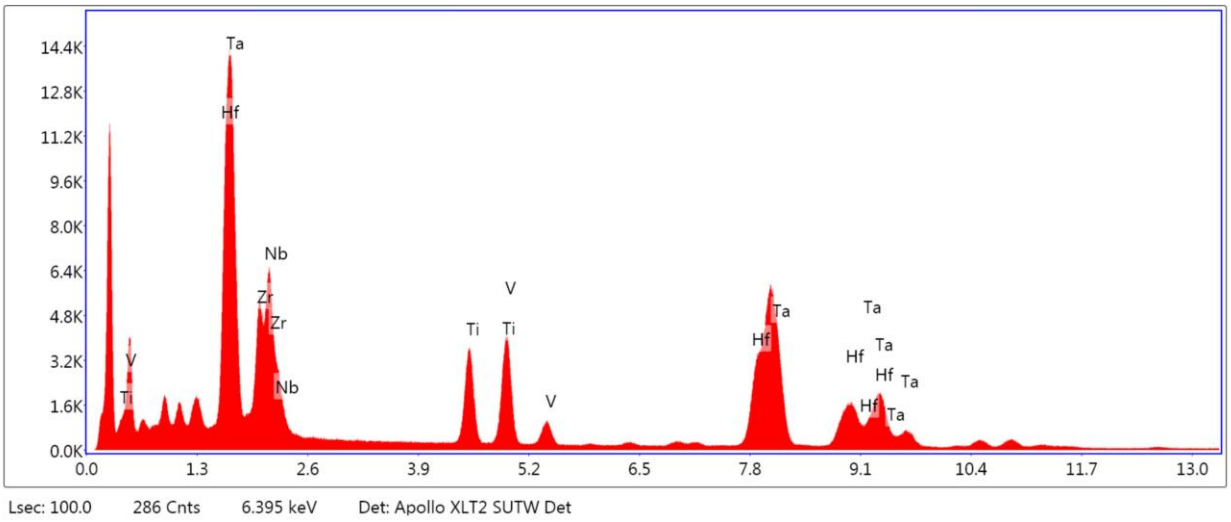

Figure F.3 EDS analysis of radiation-induced segregation for HfNbTaTiVZr alloy showed the chemical composition percentage of different elements corresponding to Figure 6.3 point c

eZAF Smart Quant Results

Element	Weight %	Atomic %	Net Int.	Error %	Kratio	Z	R	A	F
TiK	16.30	32.07	3548.96	8.49	0.0406	1.0082	0.8112	0.2303	1.0728
V K	14.93	27.63	3647.75	8.39	0.0392	0.9914	0.8179	0.2438	1.0870
HfL	23.78	12.56	8477.56	2.61	0.2316	0.9952	1.1441	0.8475	1.1548
TaL	36.43	18.98	12301.57	2.26	0.3368	0.9977	1.1502	0.8493	1.0908
ZrK	4.96	5.12	1691.83	9.31	0.0192	0.9970	0.9349	0.2962	1.3133
NbK	3.59	3.64	1211.91	9.56	0.0157	1.0062	0.9418	0.3243	1.3437

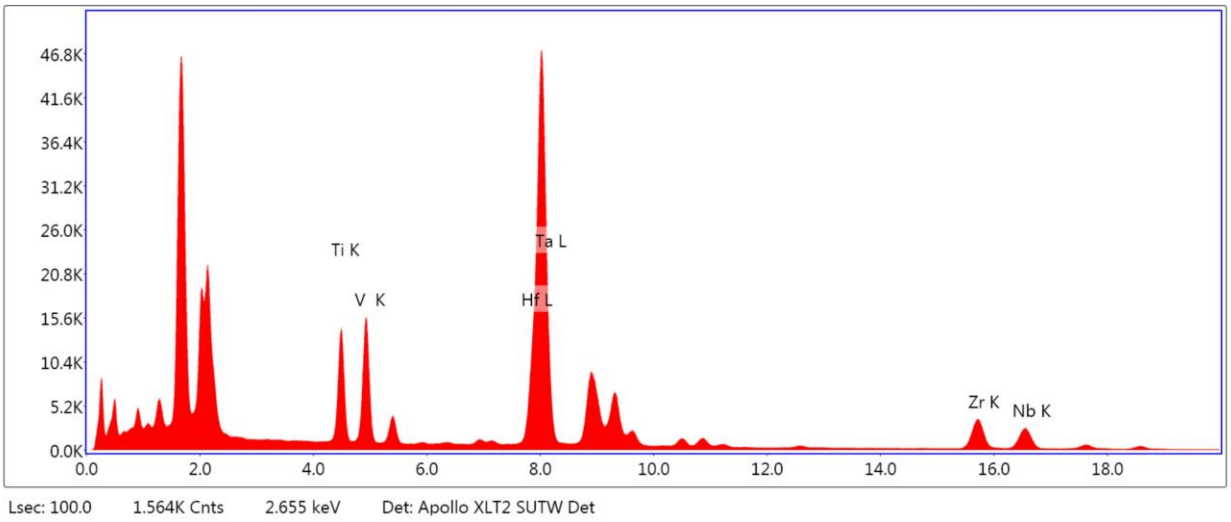

Figure F.4 EDS analysis of radiation-induced segregation for HfNbTaTiVZr alloy showed the chemical composition percentage of different elements corresponding to Figure 6.3 point d

eZAF Smart Quant Results

Element	Weight %	Atomic %	Net Int.	Error %	Kratio	Z	R	A	F
TiK	18.23	33.69	373.56	9.18	0.0471	1.0078	0.8256	0.2398	1.0682
V K	17.20	29.89	393.14	9.05	0.0466	0.9912	0.8325	0.2529	1.0796
HfL	22.89	11.35	720.52	3.39	0.2167	0.9954	1.1647	0.8280	1.1487
TaL	31.77	15.54	954.43	2.86	0.2877	0.9979	1.1710	0.8311	1.0917
ZrK	5.48	5.32	180.01	10.90	0.0225	0.9974	0.9516	0.3128	1.3164
NbK	4.42	4.21	142.55	11.19	0.0204	1.0065	0.9586	0.3414	1.3418

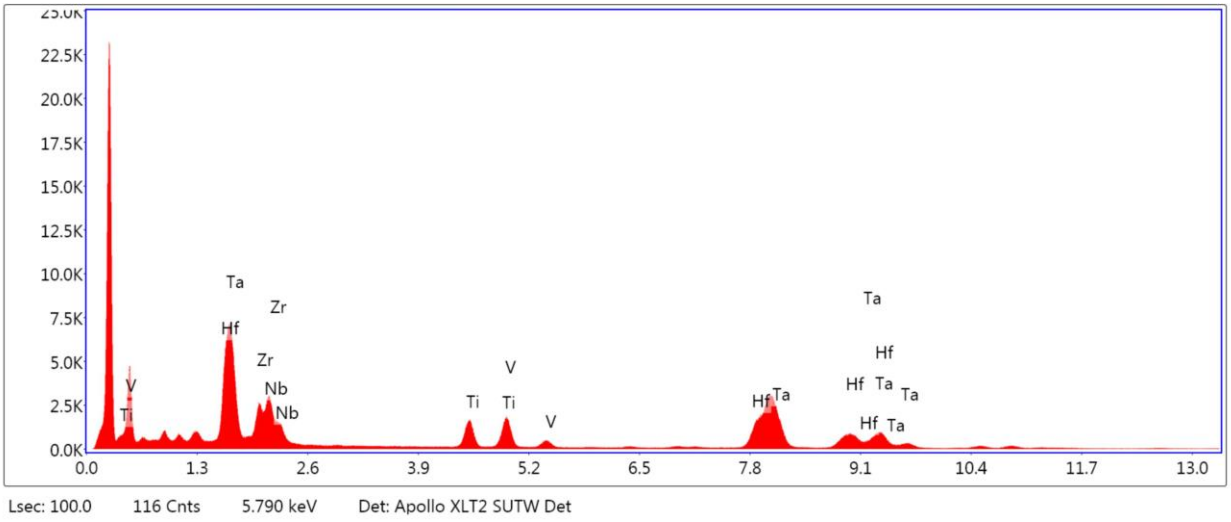

Figure F.5 EDS analysis of radiation-induced segregation for HfNbTaTiVZr alloy showed the chemical composition percentage of different elements corresponding to Figure 6.3 point e

eZAF Smart Quant Results

Element	Weight %	Atomic %	Net Int.	Error %	Kratio	Z	R	A	F
TiK	17.77	33.27	471.36	9.04	0.0454	1.0078	0.8227	0.2372	1.0690
V K	16.58	29.19	491.19	8.93	0.0445	0.9912	0.8295	0.2504	1.0810
HfL	23.35	11.73	967.63	3.21	0.2226	0.9953	1.1606	0.8335	1.1490
TaL	32.21	15.96	1272.86	2.72	0.2934	0.9978	1.1668	0.8360	1.0918
ZrK	5.55	5.46	236.43	10.69	0.0226	0.9973	0.9482	0.3104	1.3158
NbK	4.54	4.38	189.80	10.91	0.0208	1.0064	0.9552	0.3388	1.3408

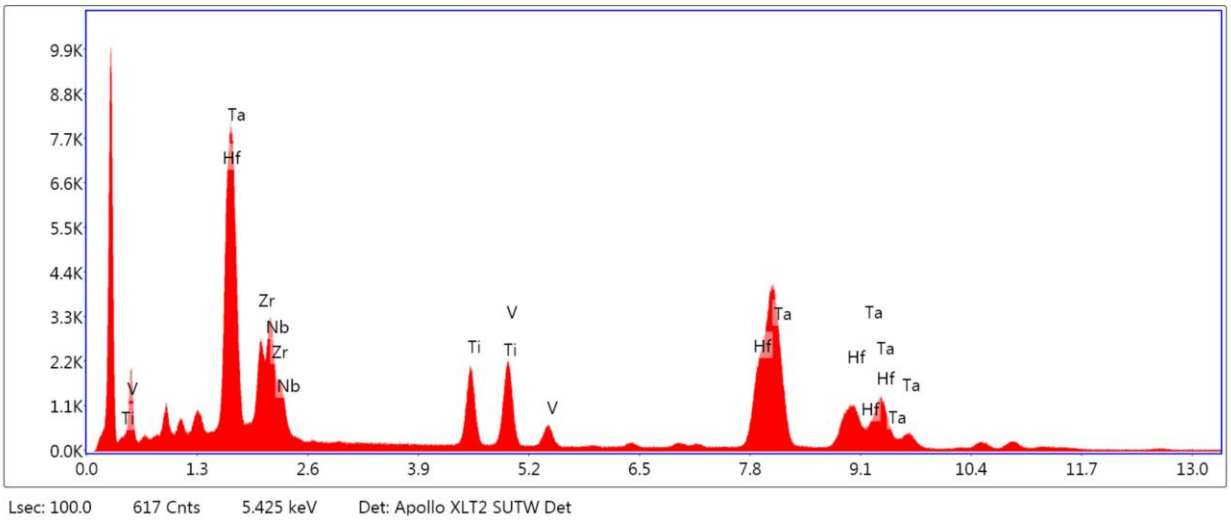

Figure F.6 EDS analysis of radiation-induced segregation for HfNbTaTiVZr alloy showed the chemical composition percentage of different elements corresponding to Figure 6.3 point f

eZAF Smart Quant Results

Element	Weight %	Atomic %	Net Int.	Error %	Kratio	Z	R	A	F
TiK	17.72	33.06	762.06	8.84	0.0454	1.0079	0.8235	0.2379	1.0689
V K	16.95	29.74	813.97	8.69	0.0456	0.9912	0.8303	0.2511	1.0805
HfL	22.70	11.37	1519.35	3.05	0.2162	0.9954	1.1617	0.8315	1.1507
TaL	32.63	16.12	2081.81	2.56	0.2968	0.9979	1.1679	0.8347	1.0917
ZrK	5.43	5.32	374.56	10.23	0.0222	0.9973	0.9491	0.3108	1.3163
NbK	4.57	4.39	309.13	10.48	0.0209	1.0065	0.9561	0.3394	1.3411

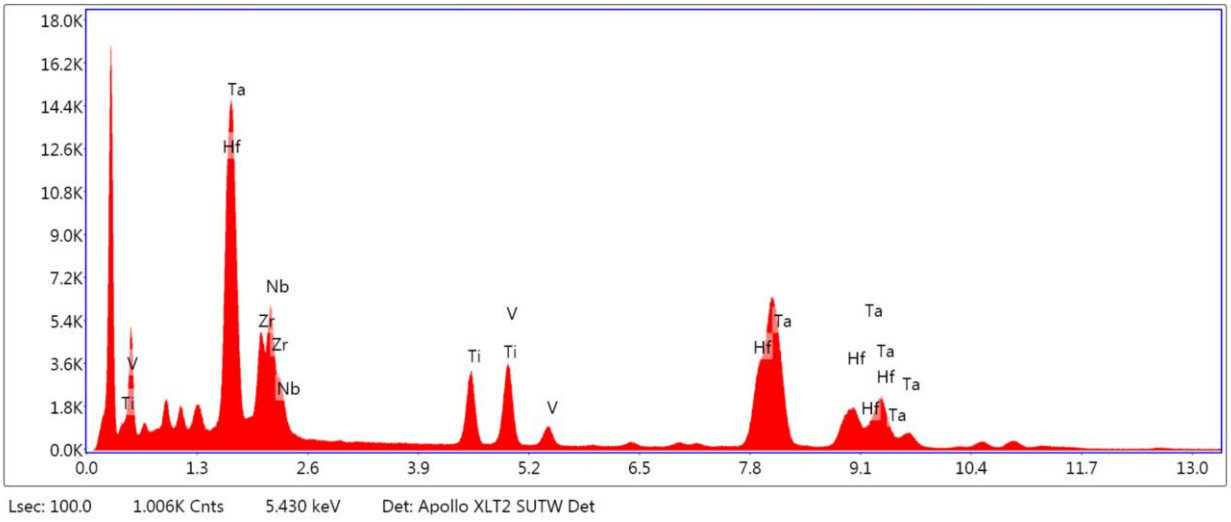

Figure F.7 EDS analysis of radiation-induced segregation for HfNbTaTiVZr alloy showed the chemical composition percentage of different elements corresponding to Figure 6.3 point g

VITA

Carl Jianren Zhou was born in December 1989 in Jiangxi Province, China. He received his bachelor's degree in the School of Material Science and Engineering, Chongqing University of Technology, China in June 2011 and a master's degree in the School of Mechanical and Automotive Engineering, South China University of Technology, China in June 2014. While working on his master's degree, he was a research assistant in the National Engineering Research Center of Near-Net-Shape Forming for Metallic Materials (NERC-NFMM) authorized by Ministry of Science and Technology of the People's Republic of China. In the meanwhile, he worked as a research & develop intern at Guangzhou Huajin Alloy & Advanced Material Industry Co., Ltd in Guangzhou City, China. In September 2014 he joined the Nuclear Energy Materials Group in the Department of Mechanical & Industrial Engineering at Louisiana State University in the United States of America to pursue his Doctor of Philosophy degree. Before joining Louisiana State University, he was accepted as a Ph.D. student in the Department of Mechanical Engineering at the University at Buffalo, the State University of New York.